

Kaluza Klein Dark Matter Analysis with the AMANDA Neutrino Telescope

Thesis submitted to The University of Canterbury
for the degree of Doctor of Philosophy

Department of Physics and Astronomy

Kahae Han

2010

Contents

1	Introduction	10
2	Physics of Extra Dimensions	14
2.1	Developments of Extra Dimensions	15
2.1.1	Historical Overview of Kaluza Klein Theory	15
2.1.2	String Theory calls on Kaluza-Klein	18
2.1.3	M-Branes and Braneworlds, and Cosmology	18
2.2	Models with Extra Dimensions	19
2.2.1	ADD scenario	19
2.2.2	Randall-Sundrum I and II	20
2.2.3	Universal Extra Dimensions UED	21
2.2.4	Split Universal Extra Dimensions	25
3	Dark Matter from Extra Dimensions	28
3.1	Astrophysical and Cosmological Origin	28
3.1.1	Stars, Galaxies and Clusters	28
3.1.2	MOND and TeVeS	28
3.1.3	Gravitational Lensing and Bullet Cluster	29
3.1.4	Cosmological Constraints	30
3.2	Particle Candidates	33
3.2.1	Relic Density of a WIMP	35
3.2.2	SUSY WIMPs from particle physics	39
3.3	Extra Dimensions Dark Matter	40
3.3.1	UED Dark Matter	41
3.3.2	sUED Dark Matter	46

3.3.3	Warped GUT Dark Matter	46
3.4	Dark Matter Detection Efforts	47
3.4.1	Direct Detection	48
3.4.2	Indirect Detection	49
4	Neutrino Detection and AMANDA/IceCube	55
4.1	Detector Overview	55
4.2	Neutrino Detection via Cherenkov Light Detection in Ice	56
4.2.1	Neutrino Nucleon Interaction in Ice	56
4.2.2	Muon Transportation in Ice and Energy Loss	59
4.2.3	Photon Transport in Ice	60
4.3	Detector Hardware, Trigger Class and Calibration	62
4.3.1	Geometry, OM characteristics	62
4.3.2	Muon Data Acquisition System	63
4.3.3	Pulse shape and time slewing	64
4.3.4	Trigger Class	65
4.3.5	Calibration	66
4.4	Physics Searches with AMANDA and IceCube	67
5	Analysis	69
5.1	Analysis Overview	69
5.2	Simulation	70
5.2.1	Simulation of Signal Monte Carlo	70
5.2.2	Simulation of Background	73
5.2.3	Simulation of Propagation and Detector Response	74
5.3	Data	76
5.3.1	Trigger Condition	77
5.3.2	Hit Cleaning and Calibration	78
5.4	Reconstruction	79
5.4.1	First Guess	79
5.4.2	Likelihood Minimization	80
5.5	Filtering	82

5.5.1	Lower Level Filtering	82
5.5.2	Higher Level Filtering	85
5.6	Cut Optimization and Sensitivity	93
6	Limits	101
6.1	Muon Flux Limit	101
6.2	Cross Section Limit	102
6.3	Uncertainties and Systematics	103
7	Conclusion and Outlook	109
A	APPENDIX	113
	Appendix A: Precut Variable Distribution for years 2002 and 2003	113
	Appendix B: COGz Variable Distribution	119
	Appendix C: NN Variable Distribution for years 2002 and 2003	120
	Appendix D: MVA trained separately for m500 and m1000	126
	Appendix E: IceCube Project Timeline	130

List of Figures

1.1	AMANDA-II Solar Neutralino Search Limits	12
1.2	Effective Volume and Sensitivity from IceCube22 and AMANDA-II 2001	13
2.1	Sketch of the large extra dimension ADD model worldview	19
2.2	Sketch of the warped extra dimension RS model	20
2.3	Split-UED model	26
3.1	Rotation Curve of the galaxy NGC 6503	29
3.2	The Cosmic Microwave Background Radiation Anisotropy	31
3.3	The WMAP CMB anisotropies	33
3.4	The Constitution of the Universe	34
3.5	Cosmological Constraints on Λ	34
3.6	WIMP's comoving number density vs temperature in the early universe	36
3.7	ATIC Nature KK dark matter	40
3.8	Relevant dark matter annihilation and scattering processes	41
3.9	Prediction for $\Omega_B h^2$	42
3.10	LZP annihilation channels	47
3.11	LZP mass	48
3.12	fraction of LZP annihilation to SM	49
3.13	Spin Independent Cross section limits from two different experiments	50
3.14	Spin Dependent Cross section limits from KIMS	50
3.15	CMSSM constrained by Fermi-LAT	52
3.16	Fermi LAT CR electron spectrum	53
4.1	The AMANDA detector	56
4.2	AMANDA-II and IceCube string configuration	57

4.3	Detection modes for high energy neutrinos	57
4.4	Charged Current νN Cross Section	58
4.5	Depth dependence of the effective scattering coefficient	61
4.6	Depth dependence of the absorptivity	62
4.7	A generic digital optical module	63
4.8	The AMANDA OMs	64
4.9	The AMANDA detector time slewing effect	65
4.10	The digitised pulse of a coax OM in AMANDA. X-axis is in bins of 25ns	66
5.1	UED WIMP annihilation Neutrino and Muon Energy Spectra	71
5.2	Neutrino and muon energy spectra from LZPs.	72
5.3	Cosmic Rays Shower Formation	73
5.4	South Pole in Darkness	77
5.5	Analysis chain	79
5.6	Cherenkov geometry	81
5.7	Arrival times	82
5.8	Neutrino and Muon Energy spectra at level 2	83
5.9	Multilayer Perceptrons	87
5.10	multivariate parameter comparison	89
5.11	Background Efficiency vs Signal Efficiency	90
5.12	Precut L3 Variables	91
5.13	Precut L3 Variables	92
5.14	Precut L3 Variables	93
5.15	Distribution of L3 Neural Net Variables	94
5.16	Distribution of L3 Variables	95
5.17	Distribution of L3 Variables	96
5.18	MVA Classifier output	97
5.19	Evolution of Neural Network Errors, 600 cycles	98
5.20	Relative Efficiency	99
5.21	Sensitivity Optimization at the final level for m750GeV	99
5.22	Final Effective Volume	100
6.1	Muon Flux Limits	103

6.2	Spin Independent Cross Section Limit	106
6.3	Spin Dependent Cross Section Limit	107
6.4	Spin Dependent Cross Section Limit with systematics	108
7.1	Sensitivity of IceCube with 86 Strings Solar Neutralino	110
7.2	Neutrino-nucleon cross sections in a variety of extra dimension models	111
A.1	Precut L3 Variables	113
A.2	Precut L3 Variables	114
A.3	Precut L3 Variables	115
A.4	Precut L3 Variables	116
A.5	Precut L3 Variables	117
A.6	Precut L3 Variables	118
A.7	COGz	119
A.8	Distribution of L3 Neural Net Variables	120
A.9	Distribution of L3 Neural Net Variables	121
A.10	Distribution of L3 Neural Net Variables	122
A.11	Distribution of L3 Neural Net Variables	123
A.12	Distribution of L3 Neural Net Variables	124
A.13	Distribution of L3 Neural Net Variables	125
A.14	MVA Classifier output	126
A.15	Distribution of L3 Variables, after the NN cut	127
A.16	Optimization of the MVA Cut values against search angle	129

List of Tables

3.1	The KK WIMPs relative annihilation fraction into various final states	43
5.1	Effective Volume at Trigger Level	76
5.2	Data Runs Selected	77
5.3	Flare Cuts	83
5.4	2001 efficiency	84
5.5	2002 efficiency	84
5.6	2003 efficiency	84
5.7	Effective Volume at Trigger level and Level 2	85
5.8	Variable Comparison for L3 Neural Net	89
5.9	Final Cut Value and Sensitivity	100
6.1	Muon Flux Limits	102
A.1	Final Cut Value and Sensitivity	128

Acknowledgements

I thank my supervisor Jenni Adams for her kind supervision throughout and also thank Suruj Seunarine for the group support.

Andreas Gross was a vital support for the last leg of my long and drawn out suffering, and deserves my gratitude for his expertise and knowledge in the subject and cheering me on till the finish line which did not seem to be in sight most of the times.

I am extremely happy that I met Dan Hooper that day in the Turf Tavern, Oxford, in the summer of 2004, which eventually led me to an interesting topic to work on as well as letting me stay for 7 great months at Oxford in 2005, and also Subir Sarkar who made me feel welcome during my stay there.

Amongst the AMANDA/IceCube WIMP analysis community, I could not have done it without Daan Hubert, who was so patient with my never ending questions. David Boersma, Carlos de los heros, Alfio Rizzo and Thomas Burgess also helped me find my way around the complicated jungle where AMANDA softwares reside. Tack to Per Olof Hulth, Christian Walck and Klas Hultqvist for the Stockholm stay.

I want to thank my umma and appa for supporting me all the way and Alex Nielsen for loving me and putting up with my tummy aches.

Abstract

In this work the search for the dark matter arising from a model of extra dimensions, otherwise known as Kaluza Klein WIMPs, on the data taken with the AMANDA neutrino telescope in the South Pole is presented. The limit on the dark matter from the Kaluza Klein Solar WIMPs analysis on the data taken from year 2001 to 2003 is derived.

Chapter 1

Introduction

The year 2002 saw the vindication for those who bet their time on studying the illusive particle, the neutrino. In his Nobel Prize winner's speech Ray Davies quoted from HR Crane's 1948 Review Article [1] on the search for neutrinos, as being the inspiration for him to study it further:

"Not everyone would be willing to say that he believes in the existence of the neutrino, but it is safe to say that there is hardly one of us who is not served by the neutrino hypothesis as an aid in thinking about the beta-decay hypothesis."

Just over half a century later, not only have we come to believe in its existence, the theory behind its mass and flavour mixing is being worked out, and in cosmology, via leptogenesis, it is featured in an argument for the existence of more matter over anti-matter in the universe.

Neutrino detection has also become centre-stage in the field of indirect measurements of astrophysics and particle physics phenomena. Whereas direct measurements are made in particle accelerators, the abundance of neutrinos coupled with their low interaction cross section make them it a unique candidate for investigating many astrophysical phenomena. The same features make the neutrino valuable for putting limits on some theoretical models in physics which predict processes in which neutrinos are produced.

One of the main outstanding questions in physics today is the existence and identity of dark matter and it is envisaged that neutrinos could play a big role in identifying the nature of dark matter. Neutrinos also double as a dark matter candidate. Another big question is the nature of dark energy. Neutrinos are linked to dark energy in the MaVaNs [2] theories which connect the varying mass of the neutrino to the dark energy.

In this thesis, an indirect search for Kaluza Klein Dark Matter Particles using the **Antarctic Muon**

And Neutrino Detector Array, AMANDA is described. Dark Matter particles captured by the Sun can annihilate producing neutrinos. These neutrinos can be searched for by looking for an excess over the background in the direction of the Sun.

In chapter 2, ideas behind the Kaluza-Klein theory and theories which involve extra dimensions will be introduced. It is interesting to note that the original motivation of introducing extra dimensions, both in its original conception and more recent revival, lie in unification of forces in particle physics. The Kaluza Klein dimensional reduction will be sketched out in detail, and then the more modern motivations for theories involving extra dimensions will be introduced without going into much detail, including three representative theories from this field. Of the representative models, three particular set-ups of extra dimensions model which give rise to dark matter candidates - the Universal Extra Dimension(UED), warped GUT and the split UED(sUED) will be noted with interest, but the discussion for the actual dark matter will be saved until Chapter 3.

Chapter 3 will consist of a brief summary of the historical aspects of the dark matter, as well as some up-to-date results from observations and some current cosmological models. After reviewing the motivation of dark matter, some possible candidates including the Weakly Interacting Massive Particles (WIMPs) will be listed. One section will introduce the particles that come from Minimally Supersymmetric extensions to the Standard Model (MSSM) called the neutralinos. These are the current favourite amongst the numerous [3] possible particle dark matter candidates which generally have the requirement of being stable, weakly interacting, and satisfying cosmological conditions. Next, the three specific dark matter models from extra dimensions mentioned in the previous chapter will be introduced. The relic density, and bounds from experiments which give the specific mass spectra of the WIMPs will be derived for the UED case.

At the moment, all possible channels of dark matter detection, i.e. collider searches, direct and indirect searches, are playing complementary roles in putting limits on various models in particle physics which fit the dark matter profile. Some models with WIMPs can produce particles such as positrons, gamma rays, anti-protons from annihilation of the WIMPs. The dark matter detection efforts will be listed in the remaining part of this chapter. The existence of Kaluza Klein WIMPs and the possibility of their detection through the methods mentioned has been explored in various works. For example collider searches are discussed in [4], direct detection in [5], and indirect detection [6]. As there already exists extensive literature [7] on aspects of neutralino dark matter and its detection with neutrinos, it will be interesting to make some comparisons between the neutralino WIMPs and the Kaluza Klein WIMPs in terms of its possible signature.

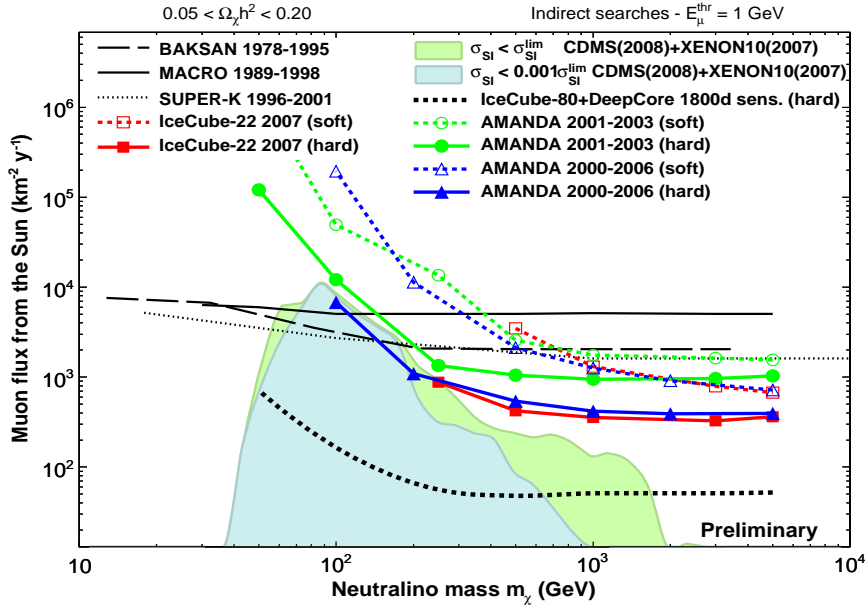


Figure 1.1: AMANDA-II Solar Neutralino Search Limits from analysis on AMANDA-II 2001-2003 data and point-source analysis on AMANDA-II 2001-2007 data. Figure taken from [13]

The AMANDA/IceCube neutrino detector in the South Pole is the first of its kind using polar ice as medium for the detection of Cherenkov light from muons. There are several other successful experiments in operation, including Baksan [8], Antares [9], Super-Kamiokande [10] which employ the Cherenkov technique for the detection of neutrinos. A brief overview of AMANDA/IceCube experiment will be given in chapter 4 in terms of its objectives and current status. The physics of neutrino detection via Cherenkov radiation and using ice as a detector medium will be summarized. Finally, some of the detector hardware and calibration-related settings will also be explained in this chapter.

There have already been many analyses performed both within the IceCube Collaboration, see for example [11] and outside the collaboration specifically looking for the neutralino. The most recent and relevant result from the AMANDA-II can be seen on Figure 1.1. Also a recent sensitivity on Kaluza Klein WIMPs was obtained with the combined AMANDA-II and IceCube [12], and this is shown on Figure 1.2

The analysis strategy of this work shares some common aspects with those of some other AMANDA-II WIMPs analyses. The commonly prepared data and the background is shared with these analyses from trigger level [14] to the lower filter levels [15].

The two main stages of the analysis will be presented in Chapter 5. After introducing some preliminary aspects of the analysis, the signal and background generation and the detector simulation detail will form the first section. WIMP signal arising from two of the three extra dimension model are generated and triggered by the detector. However, only the WIMPs from UED model are used in the full analysis. The

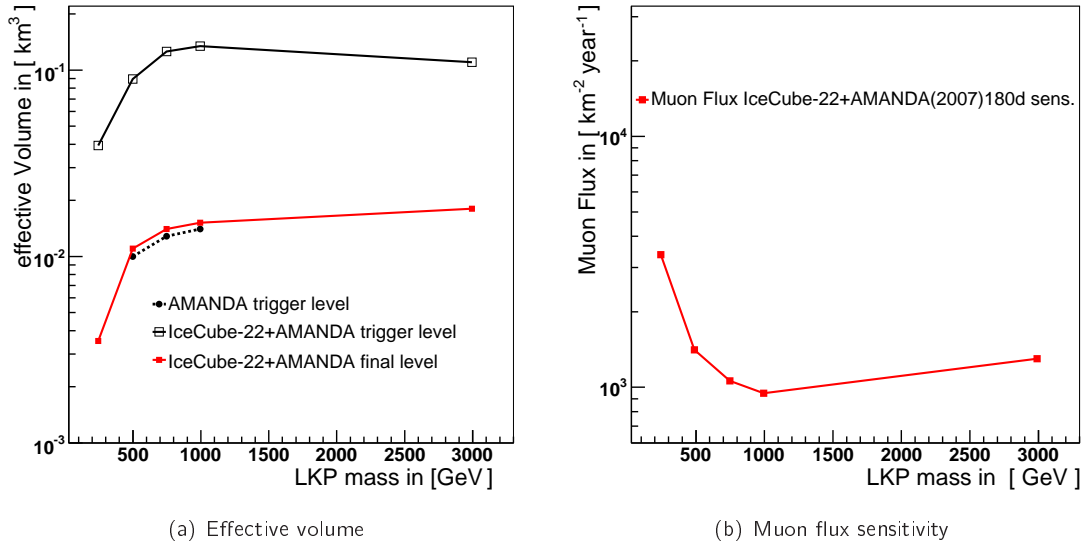


Figure 1.2: Effective Volume and Sensitivity from IceCube22 and AMANDA-II 2001. 1.2(a) shows the effective volume as a function of LKP mass at trigger level and final cut level for the IceCube-22+AMANDA analysis and at trigger level only for the AMANDA analysis. 1.2(b) demonstrates the projected sensitivity to 180 days of livetime on the muon flux from LKP annihilations in the Sun as a function of LKP mass for the IceCube-22+AMANDA detector configuration. Figure taken from [12]

method of reconstruction used in the analysis will be explained in this chapter. The main body of the work which includes the reconstruction and filtering process will make up the second section, to arrive at the sensitivity of the AMANDA detector for the UED WIMPs.

The new limit placed on the search for the Kaluza Klein dark matter from the data taken with AMANDA II neutrino telescope in the South Pole for the year 2001-2003 will be presented in chapter 6. A discussion on systematics will form the second part of the chapter.

Finally, this work will conclude with a discussion of the result and outlook in chapter 7.

Chapter 2

Physics of Extra Dimensions

The term Kaluza-Klein is used in a variety of ways in modern physics literature. Kaluza-Klein dark matter is usually used to mean any dark matter which arises from models with extra dimensions. There have been several developments since the originators developed an idea to unify gravity with electromagnetism by extending the number of spatial dimensions to four. The term refers both to the original models of Kaluza and Klein and more generally to extra-dimensional pictures where the extra-dimensions are compact and small, and the dimensional reduction technique applied in these theories à la Kaluza-Klein.

The idea of extra dimensions first gained attention when Gunnar Nordström(1881-1923) [16] introduced the notion of an extra dimension in 1914 to his theory of gravitation. Influenced by Minkowski's four dimensional spacetime, Nordström and Einstein, along with a few others were trying to create a relativistic theory of gravitation. Nordström attempted to unify his scalar gravitational theory with Maxwell's theory of electromagnetism¹ that he had developed a year earlier, by proposing a five-dimensional theory, with Lagrangian

$$\mathcal{L} = -\frac{1}{4}F_{ab}F^{ab} - J_a A^a, \quad (2.1)$$

where a,b indices run over 5 values. Here, $F_{ab} = \partial_a A_b - \partial_b A_a$ and the electromagnetic vector-potential has the components $A^a = (A^\mu, \frac{\phi}{\sqrt{4\pi G}})$, where the gravitational potential ϕ is incorporated. $J^a = (J^\mu, \rho\sqrt{4\pi G})$ is the current density 5 vector. Nordström was the first person to observe that imposing $\partial_5 A^a = 0$, which later came to be known as Klein's cylinder condition [17], would separate the 5 dimensional wave equation into Maxwell's wave equation and his own equation for the gravitational field.

However, the first serious attempts to consider extra dimensions in physics were carried out by Theodor Kaluza [18] and Oskar Klein [19] in the 1920's. Their efforts were motivated by the search for a geometric theory that would unify the forces of electromagnetism and gravity. They considered

¹Actually there were two relativistic scalar gravitational theories put forth by Nordström - first just elevating the field equation to a dalembertian, and second $\phi\Box\phi = -4\pi G T_m$ where the mass density ρ was assumed to be proportional to T_m

the possibility that an extra fifth dimension might be curled up with a very small radius and therefore be virtually unobservable. They were able to show that a model of pure gravity in five dimensions gives rise to a four dimensional universe with gravity, a $U(1)$ gauge field and a scalar field. This original mechanism is introduced in the first section of this chapter. As this was the earliest manifestations of the general ideas involved in extra dimensional theories, I place some emphasis on this in section 2.1.1.

In the second part of this chapter, I will introduce the theories in which extra dimensions are utilized. The bounds on the size of the extra dimension come from the effect of heavy Kaluza-Klein modes on electroweak observables, and this will be shown in section 2.2.3 for one of the models.

2.1 Developments of Extra Dimensions

2.1.1 Historical Overview of Kaluza Klein Theory

We have already seen in the preceding section that what is known as the cylinder condition, or imposing the metric to be independent of the extra dimension plays a part in the Kaluza-Klein theory. However, this cylinder condition alone does not entirely describe the term Kaluza-Klein Ansatz, as it is only Klein's contribution to the Kaluza-Klein Ansatz which completes the picture particularly relevant to the KK dark matter. Its historical conception will be sketched out in this section, where I will decompose the theory into the contributions by Kaluza and by Klein, drawing from [20], and [21].

As mentioned in the introduction of this chapter, Einstein was one of the people interested in the endeavour of expressing a relativistic gravitational theory. He succeeded in 1915, with his famous General Relativity. Theodore Kaluza sought to unite Einstein's General Relativity with electromagnetism. Kaluza's contribution was to make the following three assumptions:

- The universe in higher dimensions is empty.

This was inspired by Einstein, and meant that by varying the five-dimensional version of the usual Einstein action:

$$S = -\frac{1}{16\pi\hat{G}} \int \hat{R} \sqrt{-\hat{g}} d^4x dy, \quad (2.2)$$

where \hat{G} is a $5 - D$ gravitational constant,(five-dimensional quantities denoted by hats and all the capital Latin indices run over 0,1,2,3,4) and y is the new coordinate in the 5th dimension, one could recover

$$\hat{G}_{AB} = 0, \quad (2.3)$$

where $\hat{G}_{AB} \equiv \hat{R}_{AB} - \hat{R}\hat{g}_{AB}/2$ is the Einstein Tensor.

- Five Dimensional Ricci tensor and Christoffel symbols are defined exactly as in four dimensions.

This also allows us to parametrize the metric as follows:

$$(\hat{g}_{AB}) = \begin{pmatrix} g_{\alpha\beta} + \kappa^2 \phi^2 A_\alpha A_\beta & \kappa \phi^2 A_\alpha \\ \kappa \phi^2 A_\beta & \phi^2 \end{pmatrix} \quad (2.4)$$

- The cylinder condition, as mentioned before, where all the derivatives with respect to the fifth coordinate are assumed to be zero is imposed. Setting the scaling parameter $\kappa \equiv 4\sqrt{\pi G}$, this allows us to re-write equation 2.2 as:

$$S = - \int d^4x \sqrt{-g} \phi \left(\frac{R}{16\pi G} + \frac{1}{4} \phi^2 F_{\alpha\beta} F^{\alpha\beta} + \frac{2}{3\kappa^2} \frac{\partial^\alpha \phi \partial_\alpha \phi}{\phi^2} \right), \quad (2.5)$$

with $G \equiv \frac{\hat{G}}{\int dy}$. If $\phi = \text{constant}$, equation 2.5 is just the Einstein-Maxwell action for gravity and EM radiation scaled by ϕ with the third term an action for a massless Klein-Gordon scalar field.

Klein's contribution to the Kaluza Klein theory is thought to have been inspired by the onset of the other great theory at the time, quantum theory. Kaluza had, up till then, not attributed any physical attributes as such to the extra dimension he was considering, apart from saying that no physical quantities depended on it. Klein suggested that the extra dimension was actually lengthlike but too small to be seen². He went one step further to suggest that the geometry of the new dimension could have a circular topology of S^1 . This can introduce the periodicity of the fields through a Fourier expansion as the following:

$$g_{\alpha\beta}(x, y) = \sum_{n=-\infty}^{n=+\infty} g_{\alpha\beta}^{(n)}(x) e^{iny/r}, \quad (2.6)$$

$$A_\alpha(x, y) = \sum_{n=-\infty}^{n=+\infty} A_\alpha^{(n)}(x) e^{iny/r}, \quad (2.7)$$

$$\phi(x, y) = \sum_{n=-\infty}^{n=+\infty} \phi^{(n)}(x) e^{iny/r}, \quad (2.8)$$

where (n) refers to the n th Fourier mode, and r is the radius of the extra dimension.

The Kaluza-Klein Ansatz consists of discarding all massive $n \neq 0$ Fourier modes. For the five dimensional case, this is achieved by dropping the dependence on y of $g_{\alpha\beta}$, A_α and ϕ . However, in higher dimensional cases, the relationship between the full metric and the Kaluza-Klein Ansatz treated metric is less straightforward. It involves a third important metric called the ground state metric, which is the vacuum expectation value of the full metric which also determines the topology of the compact space.

The Fourier expansion also introduces us to *KK tower of modes*, a core idea behind the KK dark

²High-energy physics experiments constantly increase the constraints on the value of the size of the extra dimensions, but theorists like to make it equal to the Planck length of 10^{-33}cm .

matter. In the compact extra dimension the non-zero modes would possess quantized momenta and this could be manifested as tower of particles with extra mass $\frac{n^2}{r^2}$ added onto the zero mode mass m_0^2 .

Charge quantization is another relevant and interesting effect comes to light with the Fourier mode expansion. By starting with a massless five-dimensional scalar field, $\hat{\psi}(x, y)$ with an action :

$$S_{\hat{\psi}} = - \int d^4x dy \sqrt{-\hat{g}} \partial^A \hat{\psi} \partial_A \hat{\psi}. \quad (2.9)$$

and using Fourier expansion:

$$\hat{\psi}(x, y) = \sum_{n=-\infty}^{+\infty} \hat{\psi}^{(n)} e^{iny/r}, \quad (2.10)$$

one can obtain the following action:

$$S_{\hat{\psi}} = - \left(\int dy \right) \sum_n \int d^4x \sqrt{-g} \left[\left(\partial^\alpha + \frac{in\kappa A^\alpha}{r} \right) \hat{\psi}^{(n)} \left(\partial_\alpha + \frac{in\kappa A_\alpha}{r} \right) \hat{\psi}^{(n)} - \frac{n^2}{\phi r^2} \hat{\psi}^{(n)2} \right]. \quad (2.11)$$

This action allows us to express the charge and mass by direct comparison with the QED minimal coupling rule, $\partial_\alpha \rightarrow \partial_\alpha + ieA_\alpha$:

$$q_n = \frac{n\kappa}{r} \left(\phi \int dy \right)^{-1/2} = \frac{n\sqrt{16\pi G}}{r\sqrt{\phi}}, \quad (2.12)$$

and

$$m_n = \frac{|n|}{r\sqrt{\phi}}. \quad (2.13)$$

The mass discrepancy of the electron in $n = 1$ mode, assuming $r\sqrt{\phi} \sim l_{PL}$, would be heavier by some twenty-two orders of magnitude, but in modern compactified theories, this problem is usually discarded by identifying observed particles like the electron with $n = 0$ only.

Further motivation for extra dimensions has emerged in recent research including:

- Attempts to include internal groups as products of the geometry
- Attempts to explain the hierarchy problem without use of supersymmetry [22]
- Avoidance of conformal anomaly. Closure of Virasora algebra in string theory³
- Attempts to provide physical models for various cosmological ideas such as cosmic acceleration [23] and the big bang itself [24].
- In extended supersymmetry, where there exists $2^{\mathcal{N}}$ copies of supersymmetry e.g. $\mathcal{N} = 8$ maximal supersymmetry that does not have fields with spin greater than 2. If this is to come from an $\mathcal{N} = 1$ theory in higher dimensions then the theory will have 10 or 11 dimensions.

³In order to cancel conformal symmetry in string theory worldsheet, this requires the spacetime dimensionality to be 26 in the case of bosonic string theory or 10 in the case of superstring theory

In the next section I expand on some of the ideas mentioned above before introducing the extra dimensional theories which are relevant to the dark matter search.

2.1.2 String Theory calls on Kaluza-Klein

The Kaluza Klein dimensional reduction mechanism was originally inspired by one of the long-enduring quests of physics - to unify the known forces and interactions of particles. It is perhaps some deep seeded desire on the human mind to simplify down to some model that would unify the various phenomena one observed in the world to be explained by as few parameters as possible. Therefore, it is hardly surprising to learn that the original model of gravity plus electromagnetism was picked up and brought to the public attention again by the same need many years later, with the advent of string theory.

In 1983 at the Workshop on Grand Unification in University of Pennsylvania, Ed Witten introduced the relatively unknown string theory which had up to then been studied by Veneziano, Nambu, Nielsen, Susskind for particle scattering. Scherk and Schwarz looked at it as a plausible way to unify the four fundamental forces.

Unlike the three other fundamental forces with successful quantum models, a successful quantum theory of gravity, needed for gravity to make sense at the microscopic scale, has yet to be worked out .

Witten brought the case forward for string theory that it would be a good way of describing all the elementary particles observed in nature. With the mass, charge and spin of each particle depending on its certain quantised vibration of a one dimensional object called a string. It incorporated a theory of quantum gravity without the infinities which arise from assuming pointlike particles and gravitons.

However, up till then, physicists had been put off by the fact that the string theory would only give sensible answers with 9 dimensions. Witten invoked the original Kaluza Klein Theory to explain that the idea of extra spatial dimensions at a small scale was not something so unconceivable.

2.1.3 M-Branes and Braneworlds, and Cosmology

It was realized soon afterwards that for completeness, string theory had to incorporate not just 1-dimensional objects like strings but two or three dimensional objects. Thus the terminology of branes was born. In other words, 1-brane would be a string. 2-brane a sheet, 3-brane a volume and so on. In 1995, Witten took five of the string theories which, before incorporating branes into the model, had been thought unrelated and came up with a single underlying theory. Soon afterwards together with Hořava, Witten came up with M-theory, which used *ten* dimensions of space instead of nine. This opened up the possibility of incorporating string theory into cosmology, and one way of doing this was to find if the tension in the branes could account for the inflationary energy, which, failed however due to the fact that the time taken for the stored energy of the branes to be released is too short to account for the time it

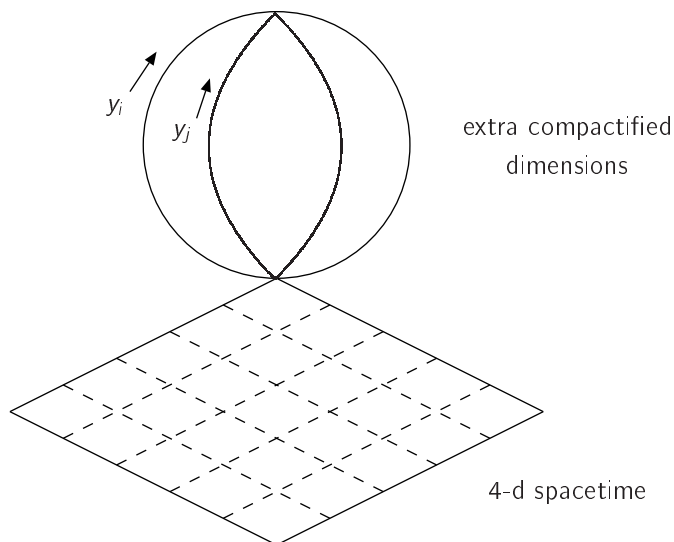


Figure 2.1: Sketch of the large extra dimension ADD model worldview. All the standard Model Fields are localized on the 3-brane, and only the gravity propagates in the bulk. Figure taken from [25]

would take for the universe could become smooth and flat as we see it today.

2.2 Models with Extra Dimensions

Once the stage was set for extra dimensions, several models were sketched out by theorists who came up with various possible scenarios, and this generated a lot of literature. As was the original idea behind Kaluza Klein theory, most models of extra dimensions have their aim in unification. Grand Unified Theory, or GUT is a theory that attempts to unite the strong force with the electroweak force, which has so far alluded physicists. Related to unification attempts is the hierarchy problem. This problem refers to unnatural situation of the weak force being so much stronger (by a factor of 10^{32}) than gravity, It can also be formulated as why the Higgs boson, if it existed, is so much lighter than GUT scale where the GUT scale is estimated by the renormalization group running of the three-gauge couplings to be greater than 10^{14}GeV . Supersymmetry is a theory which addressed this issue, and has given us a viable candidate for dark matter in terms of neutralino particles. However alternative theories attempt to address the hierarchy problem using extra dimensions and it is these which we are interested in in this thesis.

2.2.1 ADD scenario

More recent interest in extra dimensions was sparked by the work of Arkani-Hamed, Dimopoulos and Dvali (ADD) [26]. They showed that in models with D dimensions, the fundamental strength of gravity M_D could be of the order of the electroweak scale, allowing a possible resolution of the hierarchy problem. In general in dimensional compactification theories the four-dimensional Planck scale M_4 is related to

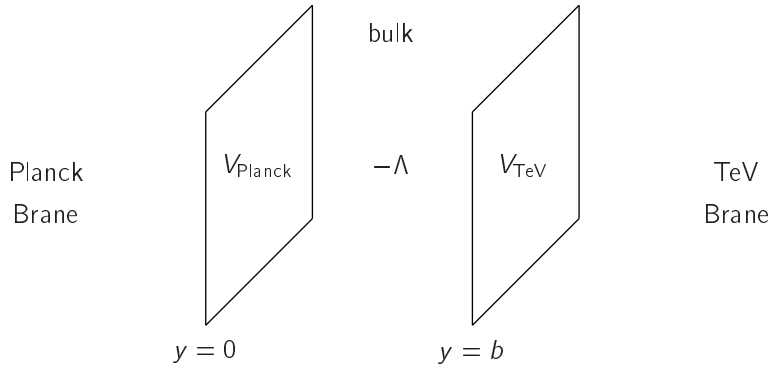


Figure 2.2: Sketch of the warped extra dimension RS model. In the original RS model, only gravity exists in the warped extra dimensions while the Standard Model particles are confined to the 3-brane. Figure taken from [25]

the D -dimensional Planck scale by

$$M_4^2 = M_D^{D-2}(2\pi r)^{D-4}. \quad (2.14)$$

Here it is considered that there are $D - 4$ extra dimensions compactified with radius r , (taken to be the same size for each dimensions) on a torus with volume $V_{D-4} = (2\pi r)^{D-4}$. All standard model fields are localized to a 3-brane, but only gravity can propagate on to the bulk. The terminology of branes and bulks form the central idea of brane cosmology where the four dimensional universe is usually restricted on the 'brane' inside a higher dimensional space called the 'bulk'. This model is also called large extra dimensions because when it was first proposed in 1998, the bound on r was still as large as 1 mm with two extra dimensions, setting $M_D = 1$ TeV. Consistency with experimental bounds from solar-system physics and brane-sum rules required them to consider at least two extra dimensions. Bounds can be placed on the extra dimensions by considering cooling via graviton emission in supernova explosions and Big Bang nucleosynthesis [27,28].

2.2.2 Randall-Sundrum I and II

Another mechanism in order to give a $1/R$ potential to the gravitational force is to turn on a negative cosmological constant in the extra dimensions described as an anti-de-Sitter space. This has effect of confining the gravitons to the vicinity of the brane and hence giving a $1/R$ potentials even if D is greater than 4 and extra dimensions are large. Randall and Sundrum (RS1) [22] built on these ideas and showed in their model that geometrical effects in the extra dimensions (known as warping) could lead to gravitons being approximately localised to the brane. This gave a much better phenomenological fit to experiments with only one extra dimension, but required the inclusion of a negative tension brane. A later model [29] (RS2) showed that a similar geometrical effect could lead to the extra-dimension being infinitely large and removing the negative tension brane.

Amongst all the models with extra dimensions one of the very few that gives rise to a viable dark matter particle is a variant model of the Randall Sundrum Warped geometry, [30, 31] where all standard model fields propagate in the bulk which is a 5 dimensional anti-de-Sitter space AdS_5 , except for the Higgs which is localized on the TeV Brane. This is embedded into a GUT, and its detection prospects were explored by Servant and Hooper in [32]. In this model, first, the electroweak gauge group is extended to $SU(2)_L \times SU(2)_R \times U(1)$ and then embedded in a GUT. Proton stability is imposed via a Z_3 symmetry, a combination of baryon number and $SU(3)$ color,

$$\Phi \longrightarrow e^{2\pi i(B - \frac{n_c - \bar{n}_c}{3})} \Phi, \quad (2.15)$$

where B is the baryon number of Φ and $n_c(\bar{n}_c)$ are the number of colour(anti-colour) indices. Standard Model fields do not carry a Z_3 charge. The $U(1)_B$ gauge symmetry has to be broken otherwise it would lead to the existence of a new massless gauge boson, therefore B is broken spontaneously on the Planck brane so that the $U(1)_B$ gauge boson acquires mass. However, if the B is broken by a scalar field with arbitrary baryonic charge, then the mechanism would lead to a fast proton decay. The detail and the reason behind the breaking of the symmetry is further discussed in detail in section 3.3 of [31]. In order to ensure that proton decay is Planck suppressed, it is broken with $\delta B \neq \frac{1}{3}, \frac{2}{3}$ and this can be achieved via the imposing of the Z_3 symmetry as shown above.

The KK states which carry non-zero Z_3 charge are stable and the lightest of these, called LZP (lightest Z_3 particle), is a viable WIMP candidate.

Both the ADD model and the original RS models required that all standard model particles be constrained to a four dimensional brane. While brane-like objects appear naturally in string theory the existence of this confinement process seemed to many to be rather ad-hoc. Furthermore, extra-dimensional theories, with higher-dimensional Planck scales of the order of electroweak symmetry-breaking ($\sim 1\text{TeV}$) generically have problems with observations of proton decay and lepton and baryon number conservation. This is because higher-dimensional terms in the Lagrangian are no longer as strongly suppressed as they are in a purely four dimensional theory.

The next model proposed can solve some of the problems which are not solved in ADD or RS models in their original forms, as well as providing us with a viable dark matter candidate.

2.2.3 Universal Extra Dimensions UED

The model which gives rise to the WIMP particle which was the focus of the analysis described in this thesis, Universal Extra Dimensions, or UED, is closely related to the original Kaluza-Klein proposal. Proposed by Cheng, Applequist and Dobrescu in [33] the extra dimensions are compact and all particles

are able to move in the extra dimensions. Thus all standard model particles have a Kaluza-Klein tower of modes.

Conservation of momentum in the extra-dimension leads to conservation of Kaluza-Klein number modulo two and no tree-level contributions to electroweak observables.

The action for the standard model in higher dimensions can be written as the following:

$$\begin{aligned}
S = \int d^4x \int d^n y & \left[\frac{1}{2g^2} F_{MN} F^{MN} \right. \\
& + i\bar{Q}\Gamma^M D_M Q + i\bar{u}\Gamma^M D_M u + i\bar{d}\Gamma^M D_M d \\
& + \bar{Q}\lambda_u u i\sigma_2 H^* + \bar{Q}\lambda_d d H \\
& \left. + \mathcal{L}_{\text{Higgs}} + \text{leptons} + \dots \right] \tag{2.16}
\end{aligned}$$

The M, N are higher dimensional indices running from 0 to $3 + D$ and Q, u, d are part of the $4 + D$ dimensional fermions, whose zero mode correspond to the standard model fermions. Γ^M are $4 + D$ anti-commuting $2^{K+2} \times 2^{k-2}$ matrices where $D = 2K$ for even D and $D = 2k + 1$ for odd D . As can be seen, there are no $\delta(y)$ functions present. The UED model, by definition, has no tree-level brane-localized fields or interactions, and all fields and interactions are bulk interactions. This leads to a discrete remnant of translation invariance which survives the compactification. This is known as KK number conservation. By promoting all the standard model particles to bulk, the spin 1/2 particles acquire more degrees of freedom, which means the fermions become generically non-chiral in the four dimensions. This problem is solved by orbifolding, i.e. compactifying on surfaces with endpoints. In models with one extra dimension, the extra dimension is half a circle, or S^1/Z_2 but in two extra dimensions and higher, there are a choice of dimensions to compactify on, including a torus with opposite sides identified, or T^2/Z_2 .

The orbifolding leads to fixed points on which interactions that break KK interactions can exist. The KK conservation is broken to a subgroup called KK parity, written as $P_{KK} = (-1)^k$ for the k th KK mode, implying:

- The lightest level-one KK mode is stable.
- Odd level KK modes can only be produced in pairs
- Direct couplings to even KK modes occur through brane-localized, loop-suppressed interactions.

Particularly for the case of six dimensions, the UED model provides us with some attractive features, such as the natural way in which the three generations of leptons and quarks can arise and the long lifetime of the proton.

Three Generations

Dobrescu and Poppitz in [34] sketches out the case for the UED where global anomaly cancellation requires more than one generation of quarks and leptons in two universal extra dimensions. Although the 4-dimensional anomalies cancel within a generation, they show that in a 6 dimensional theory, the anomalies do not cancel easily, which impose a constraint on the number of generations. The detail is not presented here, but in six dimensions of UED, there are global gauge anomalies. These are due to the change of sign of the Weyl fermion determinant under gauge transformations that are topologically disconnected from the identity; in six dimensions they arise whenever the gauge group G has nontrivial homotopy group of maps of the 6-sphere onto the gauge group, $\pi_6(G)$. Although the 6 dimensional $SU(3)_c$ global anomaly is cancelled within each generation, the $SU(2)_w$ global anomaly cancellation requires:

$$N(2_+) - N(2_-) = 0 \pmod{6} \quad (2.17)$$

where $N(2_{\pm})$ is the number of doublets of chirality \pm .

Then one must consider the case of number of generations, n_g , with identical chirality assignments. Doing this leads to a constraint that the number of generations must satisfy the following:

$$n_g = 0 \pmod{3} \quad (2.18)$$

This result is often used as one of the arguments for the UED with 6 dimensions - as it gives a natural way of obtaining the reason for three generations in quarks and leptons.

Proton Decay

It was already mentioned that proton stability is not explained in either of the original ADD or the RS models. In warped GUTs imposing proton stability results in a stable dark matter particle. [35] shows how this problem can be solved within UED with six dimensions. The six-dimensional Lorentz group, $SO(1,5)$ has a subgroup $SO(1,3) \times U(1)_{45}$ where $U(1)_{45}$ corresponds to rotations between the fourth and fifth extra dimensional operators. $U(1)_{45}$ symmetry gives conserved charge that prevents simple, baryon number violating terms. Similarly to the case of the anomaly cancellation, one comes up with the sum rule of the following:

$$3\Delta B \pm \Delta L = 0 \pmod{8} \quad (2.19)$$

which must be satisfied for all zero-mode fields. This not only forbids proton decay with less than 6 fermions, but also baryon-number violating interactions which lead to neutron-antineutron oscillations and lepton-number violating interactions which lead to Majorana neutrino masses.

Bounds from Experiments

In UED models, no new contributions exist at tree level which affect the Z-width through additional gauge bosons coupling to light fermions. This is because KK parity forbids tree-level couplings of $Z^{(k)}$ with the fermion zero modes. The lower bounds for the radius, $1/R$ of the UED model can be calculated, however, from one-loop interactions. Three parameters can be calculated from the measurements. The first parameter, T , measures the splitting in the W and Z masses due to physics beyond the standard model, is a good candidate for constraining $1/R$.

$$\alpha T = \Delta \left(\frac{M_W}{M_Z \cos \theta_W} \right). \quad (2.20)$$

Three terms contribute to the total T and they are all weak isospin violation terms: T_j^t from the top-bottom mass-splitting, T_j^h , VEV of the zero mode Higgs causing higher mode Higgs to violate isospin and finally T_j^V , the contribution from the electroweak gauge bosons. This is expressed in the following way:

$$T = \sum_j D_j (T_j^t + T_j^h + T_j^V) \quad (2.21)$$

where the sum is over all modes up to the cutoff scale and D_j is the density of states at each level j . With the measured experimental values of M_W, M_Z, m_t and α , one can derive a bound on the j th KK mass level, $M_j = j/R$.

In addition to the T parameter, there is also the S parameter:

$$S \equiv -\frac{8\pi}{M_Z^2} (\Pi_{3Y}(M_Z^2) - \Pi_{3Y}(0)) , \quad (2.22)$$

where $\Pi_{3Y}(q^2)$ is the vacuum polarization from physics beyond the standard model (gauge couplings are factored out from the hypercharge definition where $Y \equiv 2(Q - T_3)$). It is shown in [36] that once $1/R$ from T is satisfied, there is no additional constraint from S .

One-loop corrections of the KK modes to the $Z \rightarrow b\bar{b}$ branching ratios can also constrain the radius, R . The quantity examined is

$$\Delta R_b = 2R_b(1 - R_b) \frac{g_L^b \Delta g_L^b + g_R^b \Delta g_R^b}{(g_L^b)^2 + (g_R^b)^2} \quad (2.23)$$

where R_b is the ratio of the Z decay widths into $b\bar{b}$ and hadrons, and g_R^b and g_L^b are simply convenient expressions involving the Weinberg angle, given by:

$$g_R^b = \frac{1}{3} \sin^2 \theta_W \quad g_L^b = -\frac{1}{2} + \frac{1}{3} \sin^2 \theta_W. \quad (2.24)$$

Of the three parameters introduced, T parameter imposes the strongest bound on $1/R$. Using the

experimental values for M_W , M_Z , m_t , and α , the T parameter can be written in the form

$$T \approx 0.76 \sum_{j=1}^{n_{\max}} D_j \frac{m_t^2}{M_j^2} \left\{ 1 - 0.81 \frac{m_t^2}{M_j^2} + 0.65 \frac{m_t^4}{M_j^4} + \mathcal{O}(m_t^6/M_j^6) - 0.057 \frac{M_h^2}{m_t^2} [1 + \mathcal{O}(M_h^2/M_j^2)] \right\}, \quad (2.25)$$

where $m_t \approx 175$ GeV.

The sum over states are convergent for the case of $D = 5$ but log-divergent for $D = 6$ and power divergent for cases greater than six dimensions. With the experimentally measured values giving $T \lesssim 0.4$ this yields

$$\frac{1}{R} \gtrsim 300 \text{ GeV} \quad (2.26)$$

for the case of five dimensions. For two extra dimensions the bound increases to:

$$\frac{1}{R} \gtrsim 500 \text{ GeV}. \quad (2.27)$$

2.2.4 Split Universal Extra Dimensions

While Universal Extra Dimensions had its motivation in solving some of the particle physics theoretical problems posed by earlier models, the split Universal Extra Dimensions, on the other hand, has its basis in solving observational problems of UED itself. Proposed by Park, Chen and Nojiri in [37], it attempted to explain the discrepancy in the potential observation of UED dark matter by the current experiments such as ATIC [38], PPB-BETS [39] and PAMELA [40]. Astrophysical sources, in particular, from pulsars [41] have also been proposed as an explanation. However, in general, the attempt to attribute the signal to a UED dark matter annihilation scenario, has suffered from an inconsistency of non-observation of an excess in antiproton flux by the same experiment in the case of PAMELA, and also the non-observation of the sudden feature of cosmic ray electron spectrum by the Fermi Gamma Ray Space Telescope [42] in contradiction with the ATIC result. The sUED is a model which has been proposed to address these phenomenological issues.

This model uses a method of quasi-localizing the fermions on the boundaries while keeping the KK parity intact. Production of the hadron is suppressed by heavy Kaluza Klein quarks so that a better fit to the PAMELA anti proton data in [43].

The central idea behind the split-UED or the sUED model is that by introduction of a so-called 5D bulk mass the KK spectra of the quarks and leptons are doubled. One chirality of their zero modes are projected out by the orbifold condition while the other one is left as standard model fermions. This is achieved by a step function introduced as $\theta(y > 0) = 1$ and $\theta(y < 0) = -1$ for the kink mass

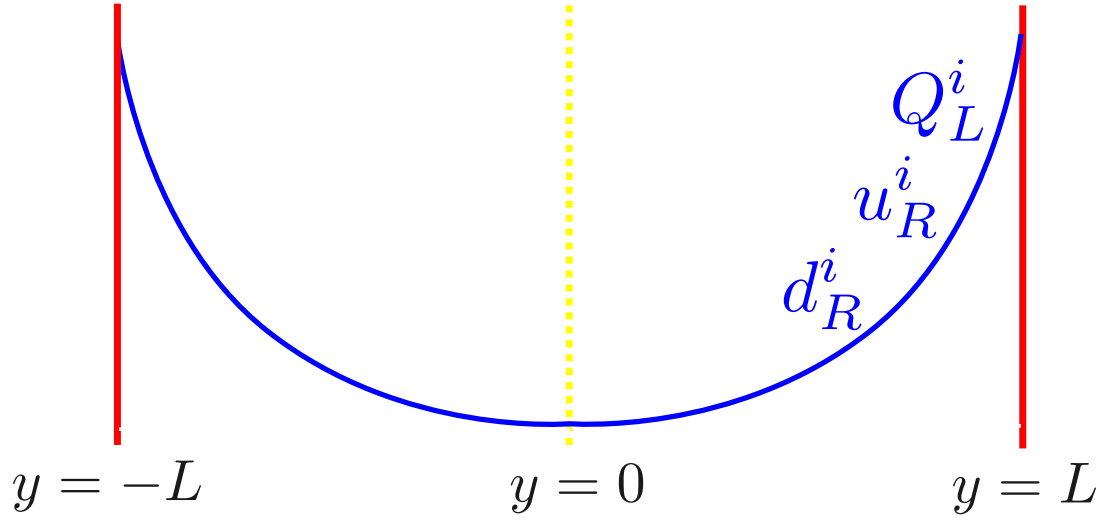


Figure 2.3: Split-UED model - the original setup from [37]. The Figure shows the profile of wave functions of the quasi-localized quarks in the extra dimension. It shows the inversion invariance about the midpoint at $y = 0$ and localized towards the end points at $y = L$ and $y = -L$.

$m_5^{ij}(y) = \mu_5^{ij}\theta(y)$ in the following:

$$S_{\text{split-UED}} = S_{\text{mUED}} - \int d^4x \int_{-L}^L \sqrt{g} m_5^{ij}(y) \bar{\Psi}_i \Psi_j \quad (2.28)$$

and Ψ_i are the bulk Dirac spinors containing quarks and leptons in their zero modes. One should notice that the zero mode wave functions, $\sim e^{\pm \int m_5(y) dy}$, are even functions under the inversion about the middle point of extra dimension, $y = 0$, so that Kaluza-Klein parity is respected. Here \pm signs are determined by chirality. In order to make the KK states of fermion acquire additional mass, this is done by the following:

$$m_n^2 = m_0^2 + k_n^2 + \mu_5^2 \quad (2.29)$$

where m_0^2 comes from the ordinary standard model Yukawa interaction, k_n^2 from the momentum of the extra dimension and the last term μ_5^2 from the 5D bulk mass. Once the 5D bulk mass is thus introduced, Kaluza-Klein modes can get additional mass contributions and become heavier while zero mode remain massless because of the orbifold condition. k_n is determined by considering the boundary conditions, $\mu_5 = \pm k_n \cot k_n L$ for KK modes - see Appendix of [43] for more.

The following bulk mass parameters choices are made to control the KK spectra:

- 5D bulk masses for quarks are chosen to be universal and larger than the typical KK scale
- 5D bulk masses for charged leptons are chosen separately for μ_{e_R} , μ_{μ_R} , and μ_{τ_R} .
- The left handed leptons 5D bulk mass is assumed to be small so that their couplings are almost

KK conserving.

The central idea is to have a tunable parameter to make the 5D quark bulk masses large in order to suppress the annihilation branching ratio to quark channels to be less than 1/10 of that of the lepton channels. In this chapter, an introduction to various models which involve extra dimension was presented, starting with a historical overview to the more recent models. For the most part the motivations from cosmology was not considered as this will be presented in the next chapter. In particular, dark matter arising from the following models : the UED model, a variant of the RS model and split UED will be introduced. For the analysis work, only the UED model dark matter is considered.

Chapter 3

Dark Matter from Extra Dimensions

3.1 Astrophysical and Cosmological Origin

3.1.1 Stars, Galaxies and Clusters

For more than half a century astronomers have known that there is not enough luminous material in galaxies to stabilize them via Newtonian gravity [44]. In 1933, Zwicky [45] applied the virial theorem to the Coma Cluster. In calculating the luminosity to mass conversion factor by applying the virial theorem to its measured average velocity along the line of sight from the observer in his 1937 paper, he found this conversion factor to be much higher to the one for the local stellar system. One of the possible explanations he suggested was that the cluster contained some material which did not emit light. This result was met with much skepticism as was the term, “dark matter” he coined for the missing matter. In 1970, Vera Rubin and Kent Ford measured the velocity of stars in a spiral galaxy showing the same characteristic of a flat appearance out to a large radius as was shown by Zwicky’s galaxy measurement. Two possible solutions to this problem present themselves; either Newtonian gravity is not the correct weak-field approximation to be used in this context [46] or there is a significant amount of non-luminous material present in the galaxies [44, 45].

3.1.2 MOND and TeVeS

In the case of the first of the two solutions proposed in the previous section, i.e. that the Newtonian gravity be modified to explain the observed discrepancies, Milgrom’s Modified Newtonian Dynamics, or MOND, [48] and its relativistic version by Beckenstein, Tensor Vector Scalar (TeVeS) [49], have succeeded to various degrees with their attempts. The idea in its simplest form is a relation between acceleration of each element of an extragalactic system, \mathbf{a} , and the local Newtonian field $-\nabla\phi_N$,

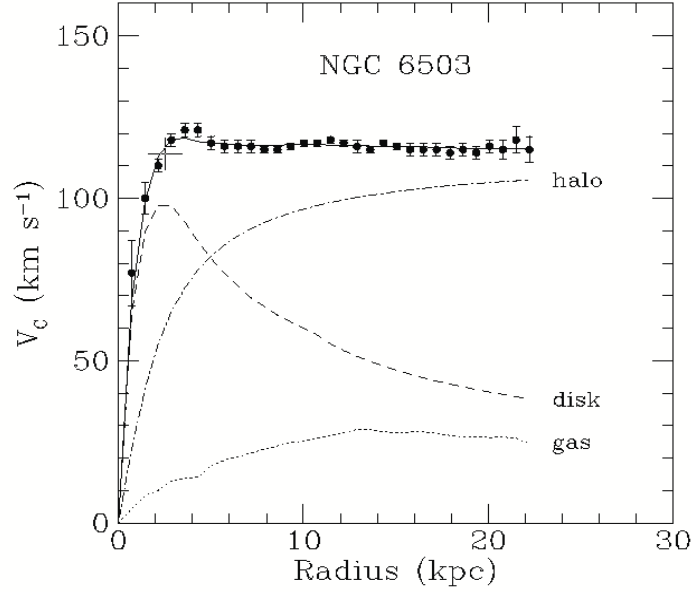


Figure 3.1: Rotation Curve of the galaxy NGC 6503

Shown velocity against distance from the center - Dotted:gas, dashed:disk, dash-dotted:dark matter - from [47]

modifying the Newtonian gravity:

$$\mu(|\mathbf{a}|/a_0)\mathbf{a} = -\nabla\phi_N, \quad (3.1)$$

where $a_0 \approx 10^{-10}ms^{-2}$ and $\mu(x) = x$ for $x \ll 1$ and $\mu(\infty) = 1$.

The bending of the light around a massive object, such as a cluster of galaxies can result in gravitational lensing. It is used to ascertain how much matter is contained, thus can be a useful tool in the field of dark matter study. Although MOND has been successful with predicting the rotational curves at galactic scale, due to its non-relativistic formulation, it fails at galaxy cluster lensing. TeVeS addressed the gravitational lensing problem with its successful formulation of MOND in relativistic form, [50] with disformal relationship between the physical metric and the Einstein metric. However, TeVeS itself has been criticized in failing to satisfy both lensing and galactic dynamics as well as having a possibility of existence of highly unstable stars. A possible resolution has been put forward with the proposal of a massive ($\sim 2eV$) neutrinos in [51].

3.1.3 Gravitational Lensing and Bullet Cluster

Perhaps the most direct and recent evidence for dark matter comes from the 'Bullet Cluster' [52] where a collision of galaxy clusters led to the separation of the luminous matter and the dominant source of gravitational lensing. Despite the X-ray observation which puts much of the baryonic matter to be

concentrated in the center of the system weak gravitational lensing observations place much of the mass outside of the central region of baryonic gas. This can be explained due to the fact that the dark matter does not interact by electromagnetic forces, and separated out from the slowed-down visible matter.

Gravitational lensing studies also put severe limits on the amount of the missing matter that can be attributed to compact objects, like the **Massive Compact Halo Objects** (MACHOs) such as planets and dwarf stars [53].

In the next section we look at the supporting evidence for dark matter and constraints from observations from cosmological scale.

3.1.4 Cosmological Constraints

In order to understand how cosmological observations can provide information on the existence and the nature of dark matter, a very short introduction to the cosmological framework is sketched out. The framework in which the modern cosmology is based on is that the universe is homogeneous and isotropic. Starting with the most general metric of GR and applying the condition of constant curvature required by homogeneity gives us the Friedmann-Robertson-Walker metric:

$$ds^2 = -dt^2 + a^2(t) \left[\frac{dr^2}{1 - kr^2} + r^2 d\Omega^2 \right]. \quad (3.2)$$

Here t is the proper time, $a(t)$ expansion factor and the three possible surfaces can be expressed by $k = -1, 0, 1$ (saddle, flat, sphere respectively). The stress-energy tensor, $T_{\nu}^{\mu} = \text{diag}(\rho, -p, -p, -p)$, of a homogeneous perfect fluid is used to describe the three states of the universe at various times by the dynamical variables : density, ρ and pressure p . The three states are:

- Matter ($p = 0$) non-relativistic material. As the universe expands, dilutes as $\sim a^3$.
- Radiation ($p = \rho/3$), photons and relativistic matter. Dilutes as $\sim a^4$.
- Vacuum Energy ($p = -\rho$). Does not dilute with expansion.

Computing the Einstein tensor for the FRW metric and inserting into the Einstein equations with $c = 1$, $G_{\mu\nu} = 8\pi T_{\mu\nu}$ leads to the Friedman equations:

$$\left(\frac{\dot{a}}{a} \right)^2 = \frac{8\pi}{3} \rho - \frac{k}{a^2} \quad (3.3)$$

$$\left(\frac{\ddot{a}}{a} \right) = -\frac{4\pi}{3} (\rho + 3p) \quad (3.4)$$

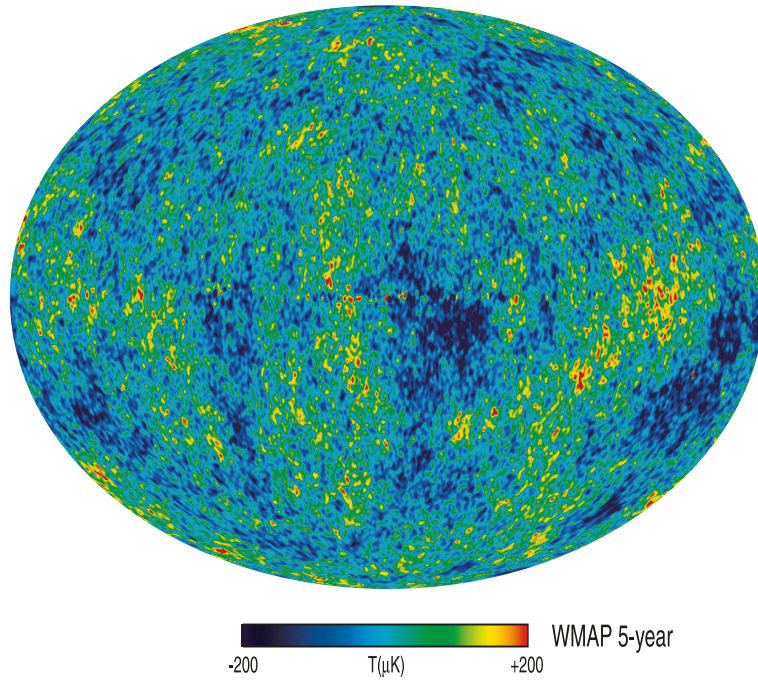


Figure 3.2: The Cosmic Microwave Background Radiation Anisotropy
 The foreground-reduced Internal Linear Combination (ILC) map based on the five year WMAP data taken from <http://lambda.gsfc.nasa.gov>

The notion of a critical density is defined as

$$\rho_c = \frac{3}{8\pi} \left(\frac{\dot{a}}{a} \right)^2 \quad (3.5)$$

that is, the energy density for a given $\frac{\dot{a}}{a}$ corresponding to $k = 0$. Using this notion we can finally express the relevant densities as the fractions of the critical densities $\Omega = \frac{\rho}{\rho_c}$ and these parameters are obtained from the cosmological observations.

CMB and the primordial element abundances as well as structure formation are used to put constraints on the amount of dark matter and its properties.

Cosmological Microwave Background

The Cosmic Microwave Background, CMB, is the background radiation of photons when they decoupled from the matter in the early universe. This has been measured by various experiments to be a near-blackbody radiation at a temperature 2.73K with 1 part in 10^5 fluctuations. The first space mission to measure the CMB anisotropy was COBE(Cosmic Background Explorer). In order to observe this fluctuation in detail showing the imprint of the density contrast in the early universe and the density ripples responsible for the structure formation as observed in the galaxy today, WMAP spacecraft,(Wilkinson Microwave Anisotropy Probe) was launched in 2001, and has been taking data since. PLANCK [54],

launched in May 2009, is the European (ESA) effort into mapping the CMB anisotropy. Other methods of experiments include balloon-borne experiments and ground-based experiments.

The CMB anisotropies information has been analysed via spherical harmonics $Y_{\ell m}(\theta, \phi)$ expansion:

$$\frac{\delta T}{T}(\theta, \phi) = \sum_{\ell=2}^{+\infty} \sum_{m=-\ell}^{+\ell} a_{\ell m} Y_{\ell m}(\theta, \phi) \quad (3.6)$$

The variance C_ℓ of $a_{\ell m}$ is given by

$$C_\ell \equiv \langle |a_{\ell m}|^2 \rangle \equiv \frac{1}{2\ell + 1} \sum_{m=-\ell}^{\ell} |a_{\ell m}|^2. \quad (3.7)$$

Assuming a Gaussianity in temperature fluctuation, all $a_{\ell m}$'s for a given l are the same, in other words $a_{\ell m}$'s do not depend on m . In Fig. 3.3 we see the plot of $\ell(\ell + 1)C_\ell/2\pi$ from the 5 year WMAP data.

In order to explain the large scale structure we see in the universe today, i.e. the galaxies and galaxy clusters, we need to have an inhomogeneity in the energy density. The most popular theories for the origin of the inhomogeneities rely on a period of inflation driven by a scalar field energy density. Quantum fluctuations in the scalar field result in inhomogeneity in the matter-energy density. The CMB provides us with a good snapshot of the level of baryon inhomogeneity at the time of photon decoupling. The non-baryonic cold dark matter which has had more time to grow compared to the baryon counterpart, provides the over-densities onto which the later-decoupled baryons can coalesce. The Sloan Digital Sky Survey(SDSS) which maps the sky for spectral information of galaxies provide us with information on the baryon acoustic oscillations(BAO). The photon-baryon fluid underwent acoustic oscillations which lasted until the time baryon decoupled from the photon field at the epoch of last scattering. This is seen in the power spectrum of the galaxy distributions taken by the SDSS. In addition, the acoustic peak provides a standard ruler for the ratio of distances at a range of redshift, and the shape of the large scale correlation function measured provides an independent verification of the matter density measured by the CMB anisotropy.

Along with data from the SDSS and Supernova 1a data, a number of cosmological constants which feature in the Lamda-CDM model in terms of some of the basic parameters are obtained and they include the following:

- $H_0 \approx 70.5 \text{ km s}^{-1} \text{ Mpc}^{-1}$, Hubble parameter
- $\Omega_b \approx 0.0456 \pm 0.0015$, Baryonic content
- $\Omega_m h^2 \approx 0.1358_{-0.0036}^{+0.0456}$ Matter content
- $\tau \approx 0.084 \pm 0.016$, Optical depth to re-ionization
- $n_s \approx 0.960 \pm 0.013$, Scalar spectral index

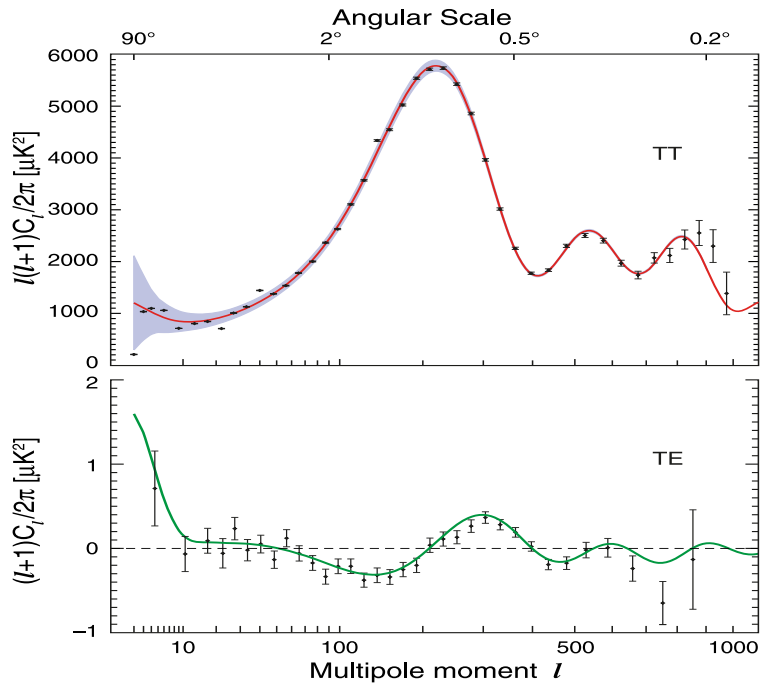


Figure 3.3: The WMAP CMB anisotropies

The temperature (TT) and temperature-polarization correlation (TE) power spectra based on the five year WMAP data. The addition of two years of data provides more sensitive measurements of the third peak in the TT and the high- l TE spectra, especially the second trough.

The shortfall between Ω_m and Ω_b is attributed to dark matter.

We can see in figure 3.5 how the different data sets can come together to constrain the parameters of the Lambda-CDM model. The fact that there is a region of overlap between all three measurements suggest a strong case in support of the lamda-CDM model of the universe.

Big Bang Nucleosynthesis

Calculations of the production of various low-mass elements based on Big Bang Nucleosynthesis [56] agree well with the observed abundances of these elements [57]. However, these calculations are dependent on the baryon mass fraction. The required mass fraction is found to be nearly identical to the one calculated from the observed luminous matter. This suggests that whatever the nature of the dark matter is, it should not interfere with the successful calculations of Big Bang Nucleosynthesis and thus it should not be baryonic.

3.2 Particle Candidates

Some baryonic candidates suggested for dark matter candidates include brown dwarfs, low mass stars and cold gas clouds. In [58], dark baryons which somehow avoided the process of luminous galaxy formation,

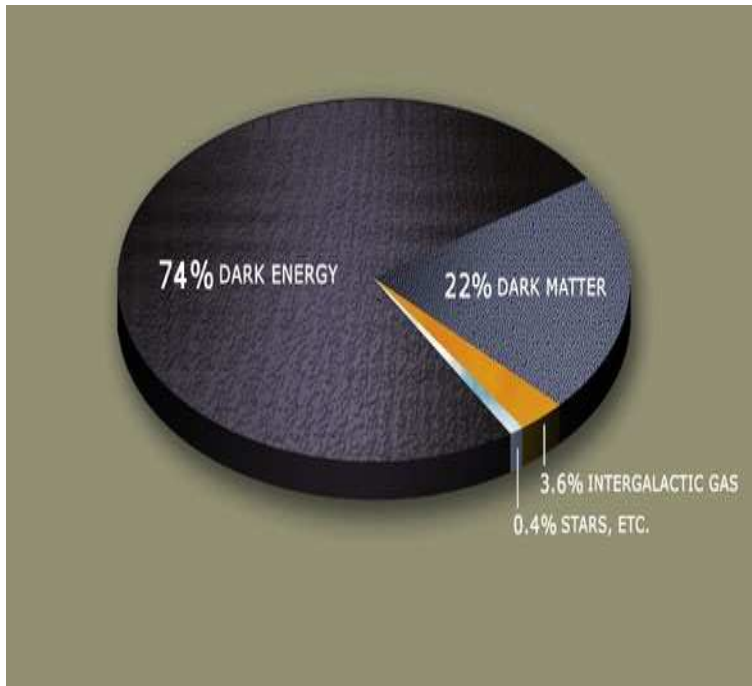


Figure 3.4: The Constitution of the Universe

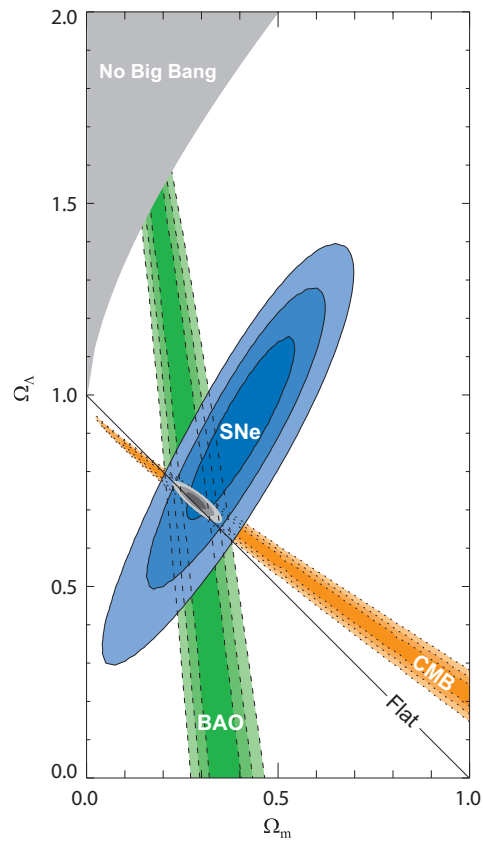


Figure 3.5: Cosmological Constraints on Λ
 68.3 %, 95.4 % and 99.7% confidence level contours on Ω_Λ and Ω_M obtained from CMB, BAO and the Union SN set, as well as their combination (assuming $w = -1$), figure taken from [55].

or being included in the Lyman alpha absorbing clouds are suggested. In the case of MACHOS which include the brown dwarf, neutron star or black hole, the amount present in halos still is not enough and would amount to no more than 20 percent of the halo mass between the solar circle and the Large Magellanic Cloud [59]. Overall, the baryonic dark matter could only account for between 10 and 25 percent of the dark matter.

A number of non-baryonic particle candidates are suggested in the review [3] fit the dark matter profile. They include:

- neutrinos and sterile neutrinos,
- axions,
- supersymmetric particles including neutralinos, sneutrinos, gravitinos, axinos,
- light scalar dark matter,
- kaluza-klein dark matter,
- little higgs dark matter.

Dark matter could be composed of more than one of the above. We already know that neutrinos from the standard model contribute to the overall dark matter albeit not enough to account for all. The fact that they are constrained to be so light means they are relativistic, therefore, they would be categorized as "hot dark matter". However, having hot dark matter impacts the fluctuations on smaller scales in the history of the universe. In other words, large scale structures such as superclusters could have been formed with relativistic neutrinos, but forming smaller structures like galaxies is not viable. Within some of the models there exist more than one particle candidate which fits the profile. The strength of the WIMP hypothesis lie in the fact that they arise independently from particle physics viewpoint, as was shown in the previous chapter. We now show how the required properties of the WIMP dark matter can coincide with the proposed conditions from particle physics.

3.2.1 Relic Density of a WIMP

To determine how a non-baryonic candidate fits the dark matter profile, one common scheme is to calculate its relic density.

Consider a particle χ existing in the early universe, which was stable, non-relativistic, and that only annihilation or inverse-annihilation could change its number in an expanding universe. If the equilibrium of these processes was broken by the expansion of the universe, then it could have resulted in a freeze-out

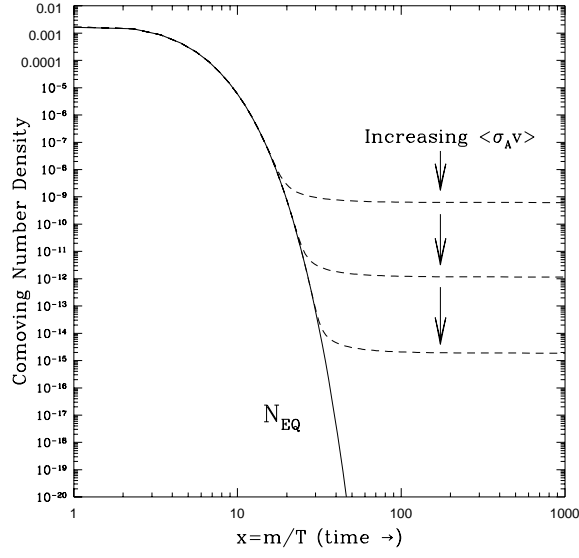


Figure 3.6: WIMP's comoving number density vs temperature in the early universe

The process of the thermal freeze-out of a stable, weakly interacting particle in the early universe. As the temperature drops below the particle's mass ($x \gtrsim 1$), the number density of such particles becomes Boltzmann suppressed. As the universe expands further, eventually these particles encounter no others of their species with which to self-annihilate, leading their density to “freeze-out”. taken from [60]

of that species [60].

If n_χ is the number density of χ , the rate of annihilation, $\Gamma_{\chi\chi}$ is written as :

$$\Gamma_{\chi\chi} = n_\chi \langle \sigma_{\chi\chi} v \rangle \quad (3.8)$$

where $\sigma_{\chi\chi}$ is the WIMP annihilation cross section and v is the relative velocity of the two χ 's. When freezeout occurs at $\Gamma_{\chi\chi} \lesssim H$, the equilibrium density, $n_\chi^{(eq)}$ is suppressed exponentially at low temperatures for a massive particle such as χ :

$$n_\chi^{(eq)}(T) \simeq \left(\frac{M_\chi kT}{2\pi \hbar^2} \right)^{3/2} e^{-\frac{M_\chi c^2}{kT}}. \quad (3.9)$$

This exponential suppression continues until the annihilation is overcome by the effects of the Hubble expansion as illustrated in Figure 3.6. One also sees that a particle with a larger annihilation cross section remains in equilibrium longer, resulting in a lower relic density.

We can express the evolution of the number density of χ in the form of a Boltzmann equation :

$$\frac{dn_\chi}{dt} + 3Hn_\chi = -\langle \sigma v \rangle [n_\chi^2 - (n_\chi^{eq})^2]. \quad (3.10)$$

This equation is usually solved by the means of expressing it in terms of entropy density, s :

$$\frac{dY}{dx} = \frac{-x\langle\sigma v\rangle s}{H(m)}(Y^2 - Y_{eq}^2), \quad (3.11)$$

where $Y \equiv \frac{n_\chi}{s} \equiv \frac{n_{\bar{\chi}}}{s}$ is the actual number of χ and $\bar{\chi}$ per comoving volume, and x is $\frac{m}{T}$, and x_F is x at the freeze-out temperature, T_F .

Using the following approximation for heavy states in the non-relativistic expansion:

$$\langle\sigma v\rangle = a + b\langle v^2\rangle + \mathcal{O}(\langle v^4\rangle) \approx a + 6b/x, \quad (3.12)$$

and the expression $\Delta = Y - Y^{eq}$, we can arrive at the

$$\Delta = -\frac{Y^{eq}}{2f(x)Y^{eq}} \text{ for } x \ll x_F \quad (3.13)$$

$$\Delta' = -f(x)\Delta^2 \text{ for } x \gg x_F. \quad (3.14)$$

for regions long before freezeout and long after freezeout.

We integrate the last equation between x_F and ∞ and using $\Delta_{x_F} \gg \Delta_\infty$, we derive the value of Δ_∞ and arrive at

$$Y_\infty^{-1} = \sqrt{\frac{\pi g_*}{45}} M_{Pl} m x_F^{-1} (a + 3b/x_F). \quad (3.15)$$

For a present day relic, χ the density of it is given by $\rho_\chi = m_\chi n_\chi = m_\chi s_0 Y_\infty$, where $s_0 = 2889.2 \text{ cm}^{-3}$ is the present entropy density. Therefore,

$$\Omega_\chi h^2 \approx \frac{1.07 \times 10^9 \text{ GeV}^{-1}}{M_{Pl}} \frac{x_F}{\sqrt{g_*}} \frac{1}{(a + 3b/x_F)}, \quad (3.16)$$

where a and b are expressed in GeV^{-2} and g_* is evaluated at the freeze-out temperature.

In order to get the relic density, one needs to calculate the annihilation fraction, and a and b , which depend on the **particle mass**.

Evaluation of the x_F leads to:

$$x_F = \ln \left[c(c+2) \sqrt{\frac{45}{8}} \frac{g}{2\pi^3} \frac{m M_{Pl} (a + 6b/x_F)}{g_*^{1/2} x_F^{1/2}} \right], \quad (3.17)$$

where c is a constant of order one determined numerically. The freeze-out temperature is obtained from iterative solution of the equation 3.17.

Eq. 3.16 can be approximated to an estimate according to [61]:

$$\Omega_\chi h^2 \approx \frac{3 \times 10^{-27} \text{cm}^3 \text{s}^{-1}}{\langle \sigma v \rangle} . \quad (3.18)$$

What is remarkable is that for the relic density in equation 3.18 to be comparable to what is observed for non-baryonic dark matter, χ should have an annihilation cross section close to a typical order of magnitude for the weak cross sections.

There are instances where the approximation in equation 3.12 fails. For instance, with the presence of a scalar field in early universe, or quintessence, the relic density has to be significantly modified as shown in [62]. Also, coannihilations or annihilations with other particles which are of comparable masses, have not been included in the calculation above. When there are particles at similar masses which share a quantum number the standard relic density calculations must be modified according to [63]. This is sketched out as follows.

Considering N particles X_i ($i = 1, \dots, N$) with masses m_i and internal degrees of freedom (statistical weights) g_i we assume that $m_1 \leq m_2 \leq \dots \leq m_{N-1} \leq m_N$, and that the lightest particle, X_1 , is protected against decay due to some symmetry. The equation 3.10 is then modified to

$$\frac{dn}{dt} = -3Hn - \sum_{i,j=1}^N \langle \sigma_{ij} v_{ij} \rangle (n_i n_j - n_i^{\text{eq}} n_j^{\text{eq}}) , \quad (3.19)$$

where n is the number density of the relic particle and $n = \sum_{i=1}^N n_i$, from the decay rate of particles, X_i , other than the lightest being much faster than the age of the Universe. Here,

$$\sigma_{ij} = \sum_X \sigma(X_i X_j \rightarrow X_{SM}) \quad (3.20)$$

is the total annihilation rate for $X_i X_j$ annihilations into a Standard Model particle. Finally,

$$v_{ij} = \frac{\sqrt{(p_i \cdot p_j)^2 - m_i^2 m_j^2}}{E_i E_j} \quad (3.21)$$

is the relative particle velocity, with p_i and E_i being the four-momentum and energy of particle i .

The thermal average $\langle \sigma_{ij} v_{ij} \rangle$, is defined with equilibrium distributions and given in terms of distribution functions in the Maxwell-Boltzmann distributions. In the case of supersymmetric particles, the thermal average has been reformulated into a more convenient expression by [64].

The details of including coannihilations in SUSY models are well established by [65]. The interplay between the annihilation rate and the particle interaction rate is subtle and its impact on the overall relic

density is non-trivial. In the case of this analysis, we are looking for WIMPs from a UED case where coannihilation is included and the implication from this particular case is explained in detail in section 3.3.1.

3.2.2 SUSY WIMPs from particle physics

Proposed in the 1970s, supersymmetry, as was briefly mentioned in the previous section, has provided us with a popular candidate for WIMP dark matter in the form of neutralinos. Supersymmetry is a model in which every SM field has a partner in which the integer spins and half-integer spins is swapped. The supersymmetric partners of the B-field (bino), W-boson (wino), and the two neutral Higgs bosons (higgsinos), all which happen to share the same quantum number, form a mass eigenstate, called the neutralino :

$$\tilde{\chi}_i^0 = N_{i1}\tilde{B} + N_{i2}\tilde{W}^3 + N_{i3}\tilde{H}_1^0 + N_{i4}\tilde{H}_2^0. \quad (3.22)$$

$\tilde{\chi}_i^0$ is referred to as the lightest SUSY particle, or LSP. More accurately, of the mixture of the four possible Majorana fermionic mass eigenstates, or neutralinos, the lightest eigenstate amongst them is taken as the LSP, although the other three also satisfy the requirement of being a dark matter candidate.

There are different versions of supersymmetric extensions to the Standard Model which are being studied today. These are minimal supersymmetric scenarios (MSSM, or non-extended supersymmetry), the constrained minimal supersymmetric scenarios (cMSSM) where accelerator results are applied to constrain the MSSM model, and extended and maximal supersymmetric scenarios where the additional indices, \mathcal{N} on the generators Q_i^α , provide a useful model for studying the quantum field theory and superstring theory.

The stability of an LSP rises from the imposing of conservation of R-Parity, to explain proton life-time. Imposing this condition giving rise to a stable dark matter candidate is also a feature of the warped GUT model where via the Z_3 symmetry, proton stability is achieved as we have seen in section 2.2.2 for the case of LZPs. Apart from the neutralino, other particles such as Sneutrino, the superpartner of a neutrino and gravitino the counterpart of a graviton, exist within the framework which can be considered as a dark matter candidate, but suffer from pitfalls.

Even with assuming the minimal supersymmetric extension to the Standard Model by constraining it to contain only the smallest possible field content which can give rise to all the fields of the Standard Model, there is still a huge number of free parameters. In considering the neutralino, the SUSY parameters determine the N_i mixing coefficient which in turn, determines the couplings and the mass of the χ . This is why it is often customary to take two extreme channels of annihilations which give rise to neutrinos as end products in a neutrino analysis of this WIMP candidate. They are commonly referred to as a soft $b\bar{b}$ and a hard channel W^+W^- because the neutrino spectra they produce are either soft with comparatively more neutrinos at lower energy, or vice versa for hard channel.

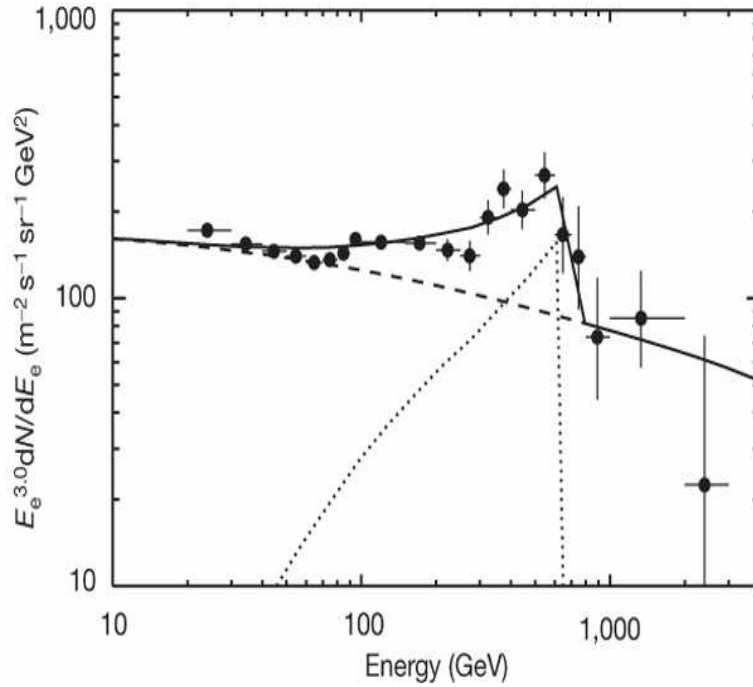


Figure 3.7: GALPROP general electron spectrum plus the KK WIMP at mass 620 GeV annihilating with the cross section $10^{-23} \text{ cm}^3 \text{ s}^{-1}$ and local dark matter density of 0.43 GeV cm^{-3} [38]

No information on how many of the neutralinos, or what proportion of them go to each annihilation channel is assumed. This is another difference that the large parameter dependent WIMPs have compared to the LKPs, the lightest Kaluza Particles, which we can utilize the branching ratio to each annihilation channel for a fixed scenario as discussed in Section 3.3.1.

3.3 Extra Dimensions Dark Matter

Amongst the WIMP class of dark matter particles, neutralino WIMPs from the SUSY models have been the most popular candidates to date. However with the new results from various indirect experiments in 2008/2009 (see 3.4.2), Kaluza Klein WIMPs gained much attention due to some results which favoured the UED dark matter - for example see Figure 3.7. Due to such results from experiments such as PAMELA [40] and PPB/BETs [39], more studies and predictions of its signature have been published. The particle spectrum the Kaluza Klein WIMPs produce has a unique characteristic and differs from the neutralino particle which is a Majorana spinor, because a KK WIMP candidate such as a B_1 has no helicity suppression preventing it from annihilation into two light fermions.

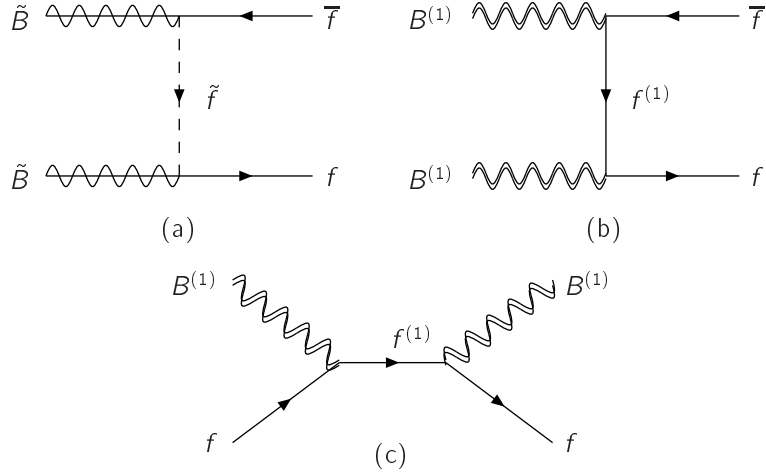


Figure 3.8: Relevant dark matter annihilation and scattering processes for (a) supersymmetry and (b),(c) UED. The supersymmetric annihilation diagram (a) is s -wave suppressed by a factor $m_{\tilde{f}}^2/m_{B^{(1)}}$, whereas the UED diagram (b) is unsuppressed. Observable annihilation in the Sun occurs through diagram (b) for example, to neutrinos with $f = \nu$ and to others as listed in Table 3.1. Annihilation in the galactic neighborhood to positrons occurs through diagram (b) with $f = \ell$. Scattering off nuclei occurs via diagram (c) with $f = q$, suitably “dressed” into a proton or neutron. [25]

3.3.1 UED Dark Matter

Of the tower of KK modes in the UED model with their masses given by:

$$m_{kk}^2 = \frac{1}{R^2} + m_{SM}^2 \quad (3.23)$$

at tree level there are two classes of radiative corrections, the first from loop terms, and the second from brane-localized kinetic terms which appear on the boundaries of the orbifold. After the radiative corrections which include the following assumptions - a.the matching contributions to the brane-localized kinetic terms are assumed to be zero at the cut off scale and b.no brane-localized quadratically divergent contributions to the Higgs mass- one notes that the KK spectrum of masses are very close in values to the degenerate SUSY spectrum. Despite the spin of the KK excitations being different from the SUSY superpartners, there will be no easy way to distinguish the spins of newly discovered particles at the colliders. This has led to a point noted by [66] that the KK spectrum could even be taken for a degenerate SUSY spectrum.

The KK parity, which is the conservation of momentum leading to the first excited mode of the photon being a stable particle is similar to the R-Parity in Supersymmetry which prevents the neutralino

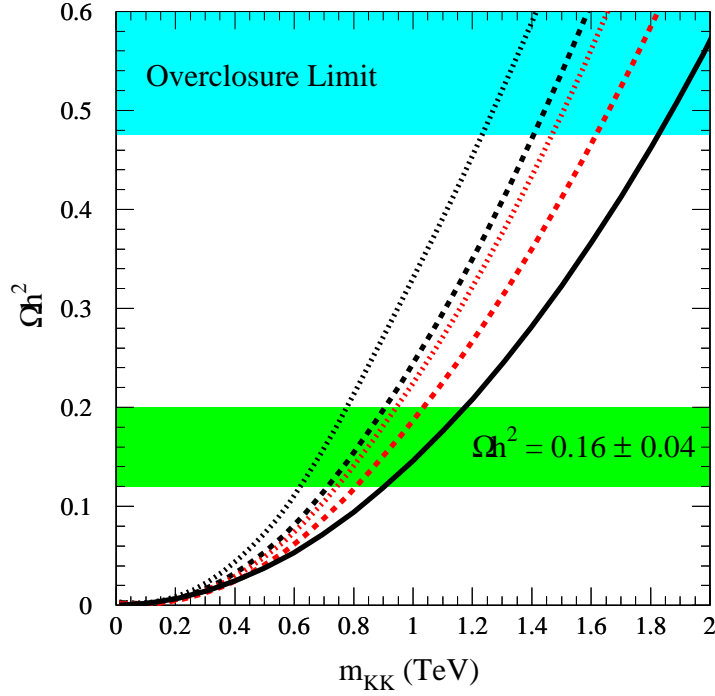


Figure 3.9: Prediction for $\Omega_{B^1} h^2$. The solid line is the case for B^1 alone, and the dashed and dotted lines correspond to the case in which there are one (three) flavours of nearly degenerate l_R^1 . For each case, the black curves (upper of each pair) denote the case $\Delta = 0.01$ and the red curves (lower of each pair) $\Delta = 0.05$. figure taken from [67]

from decaying. The KK photon has the following mass matrix in the $(B^{(n)}, W^{3(n)})$ basis

$$\begin{pmatrix} \frac{n^2}{R^2} + \delta m_{B^{(n)}}^2 + \frac{1}{4}g'^2 v^2 & \frac{1}{4}g'g v^2 \\ \frac{1}{4}g'g v^2 & \frac{n^2}{R^2} + \delta m_{W^{(n)}}^2 + \frac{1}{4}g^2 v^2 \end{pmatrix} \quad (3.24)$$

where g' and g are U(1) and SU(2) gauge couplings, while δm_B^2 and δm_W^2 are the radiative corrections to the B and W values, v is the Higgs vacuum expectation value, and R , the radius of the extra dimension. The mixing angle is much smaller than the Weinberg angle, which leads to

$$m_{B^1}^2 \simeq \frac{1}{R^2} \left[1 + \frac{g'^2}{16\pi^2} \left(-\frac{39\zeta(3)}{2\pi^2} - \frac{1}{3} \ln \Lambda R + (2\pi R v)^2 \right) \right] \quad (3.25)$$

neglecting $\sin^2 \theta^1 v^2$ corrections. Therefore, γ^1 is referred to as B^1 in most literature, or the lightest Kaluza Klein Particle, LKPs.

process	annihilation fraction	
	$\Delta_i = 0$	$\Delta_{g^{(1)}} = 0.14$
$B^{(1)} B^{(1)} \rightarrow \nu_e \bar{\nu}_e, \nu_\mu \bar{\nu}_\mu, \nu_\tau \bar{\nu}_\tau$	0.012	0.014
$\rightarrow e^+ e^-, \mu^+ \mu^-, \tau^+ \tau^-$	0.20	0.23
$\rightarrow u \bar{u}, c \bar{c}, t \bar{t}$	0.11	0.077
$\rightarrow d \bar{d}, s \bar{s}, b \bar{b}$	0.007	0.005
$\rightarrow \phi \phi^*$	0.023	0.027

Table 3.1: The KK WIMPs relative annihilation fraction into various final states

-The numbers shown are not summed over generations, and the Higgs mass was assumed to be lighter than $m_{B^{(1)}}/2$.

Relic Density Calculation

The viability of LKPs as a dark matter candidate has been explored in [67]. In [67] the authors look at cases of excitations of both KK photons and neutrinos, with and without coannihilations as possible LKPs. Only the 1st excitation of KK photons is explained here, and from here on LKP's from UED will refer only to this.

The relic density of a WIMP has been explained in section 3.2.1. The self-annihilation cross section of a B^1 is shown in the Appendix B.2 of [68]. Unlike in the case of a neutralino with its Majorana nature, there is no helicity suppression for B^1 into final fermion states, and annihilation fraction into fermions is substantial. It also allows us to calculate a definite relative annihilation fraction to all states and this is done for the case of a completely degenerate KK mass spectrum ($\Delta_i = 0$) and for the case of a relative mass splitting between the B^1 and KK quarks at ($\Delta_q = 0.14$) in table 3.1. Δ is the relative mass difference between the LKP and the second LKP, (NLKP) and is defined as $\Delta = (m_{NLKP} - m_{LKP})/m_{LKP}$. This table shows the branching ratio to the three neutrino species amount to just above one percent each, and over 20 percent to each electrons, muons and taus. The three neutrino channels and tau lepton channels make up the majority of the signal for this analysis. The rest annihilate to quarks and Higgs.

The effect of coannihilation is explored further in [67]. The right handed KK lepton l_R^1 is within one percent or so of the B^1 mass making it possible for coannihilation to occur. This constrains the mass to lie in the range around 600GeV to 800GeV according to [67]. The interesting fact to note here is that including the coannihilation actually increases the relic density of the B^1 due to the fact that the interactions with l_R^1 are smaller than self-annihilation, therefore decoupling happens at the same time and l_R^1 decays into a B^1 itself, adding to the relic density. This is opposite to the case of neutralino, where due to the efficient coannihilation between LSP neutralinos and NLSP sfermions, leading to a later decoupling time, leading to a lower relic density. The effect of the higher relic density from coannihilations is shown in the Figure 3.9, in the case of B^1 as the LKP, and e_R^1 , as the NLKP. Essentially, the result is from

the result of the calculation of the relic density without coannihilations $m_{LKP} = 900\text{GeV} \sim 1200\text{GeV}$ the effect of including coannihilations, depending on whether the NLSP include all three flavours or just one flavour of lepton, reduce the mass range to $m_{LKP} = 600\text{GeV} \sim 1050\text{GeV}$. The B^1 signal for the analysis in this work is produced at mass ranges of 500GeV, 750GeV and 1000 GeV in section 5.2.1

Capture and Annihilation in the Sun

The analysis described in the thesis looks for neutrinos from dark matter annihilation in the Sun. Dark matter particles are captured by the Sun if they interact and lose angular momentum. When a sufficient density of WIMPs is reached in the Sun annihilation's occur. Equilibrium is assumed to be reached between the capture and the annihilation rate. We outline the calculation of the relevant rates.

- Scattering Cross Section

In [69] Kurylov and Kamionkowski have shown that only scalar and axial-vector terms survive in a general case of WIMP-nucleon scattering in the extreme non-relativistic limit. The remaining terms such as pseudoscalar, vector, tensor and pseudotensor components are either suppressed by large factors or can be absorbed into these two. Spin-independent scattering can take place with all the nucleons in the nucleus, therefore the cross-section is proportional to the square of the nuclei mass. The detection using spin-independent scattering are more strongly constrained by the direct detection experiment as we shall see again in 3.4.1.

In order to calculate the B^1 WIMP capture rate in the Sun, C_{SD}^{\odot} , we use the capture rate for spin-dependent cross section from calculation in [61]:

$$C_{SD}^{\odot} \simeq 3.35 \times 10^{18} \text{ s}^{-1} \left(\frac{\rho_{\text{local}}}{0.3 \text{ GeV/cm}^3} \right) \left(\frac{270 \text{ km/s}}{\bar{v}_{\text{local}}} \right)^3 \left(\frac{\sigma_{H,SD}}{10^{-6} \text{ pb}} \right) \left(\frac{1000 \text{ GeV}}{m_{B^1}} \right)^2 \quad (3.26)$$

where ρ_{local} is the local dark matter density, $\sigma_{H,SD}$ is the spin-dependent, WIMP-on-proton (hydrogen) elastic scattering cross section, \bar{v}_{local} is the local rms velocity of halo dark matter particles.

There exists an analogous formula for the capture rate from spin-independent (scalar) scattering:

$$C_{SI}^{\odot} \simeq 1.24 \times 10^{18} \text{ s}^{-1} \left(\frac{\rho_{\text{local}}}{0.3 \text{ GeV/cm}^3} \right) \left(\frac{270 \text{ km/s}}{\bar{v}_{\text{local}}} \right)^3 \left(\frac{2.6 \sigma_{H,SI} + 0.175 \sigma_{He,SI}}{10^{-6} \text{ pb}} \right) \left(\frac{1000 \text{ GeV}}{m_{B^1}} \right)^2. \quad (3.27)$$

with $\sigma_{H,SI}$ the spin-independent, WIMP-on-proton elastic scattering cross section and $\sigma_{He,SI}$ is the spin-independent, WIMP-on-helium elastic scattering cross section. As will be mentioned again in the 6.2, much uncertainty exists in the approximation in this equation including the approximation

of the elemental abundances in the Sun.¹. However, the spin-dependent cross section is calculated from [66] given as:

$$\sigma_{\text{H,SD}} = \frac{g'^4 m_p^2}{648 \pi m_{B^1}^4 r_{q^1 R}^2} (4\Delta_u^p + \Delta_d^p + \Delta_s^p)^2 \quad (3.28)$$

where m_p is the mass of the proton and the Δ_q^p s denote the fraction of spin carried by a constituent quark q . The Spin dependent cross section in 3.28 is three to four orders of magnitude larger than the spin-independent cross section, so this allows us to ignore equation 3.27.

Using the spin fractions given by:

$$\Delta_u^p = 0.78 \pm 0.02 \quad , \quad \Delta_d^p = -0.48 \pm 0.02 \quad , \quad \Delta_s^p = -0.15 \pm 0.07 \quad , \quad (3.29)$$

we finally obtain the dominant elastic cross section for the capture in the Sun:

$$\sigma_{\text{H,SD}} = 0.9 \times 10^{-6} \text{ pb} \left(\frac{1000 \text{ GeV}}{m_{B^1}} \right)^4 \left(\frac{0.14}{r_{q^1 R}} \right)^2 . \quad (3.30)$$

where $r_{q^1 R} \equiv \frac{m_{q^1} - m_{B^1}}{m_{B^1}}$.

- Capture and Annihilation Rate in the Sun

The rate of change of the number N of B^1 particles in the Sun is given by

$$\dot{N} = C^\odot - A^\odot N^2 - C_E N , \quad (3.31)$$

where C^\odot is the capture rate obtained from above, $C_E N$ is an evaporation term which can be ignored with WIMP above the mass of a few GeV, and A^\odot is the annihilation cross section times the relative WIMP velocity per volume expressed as :

$$A^\odot = \frac{\langle \sigma v \rangle}{V_{\text{eff}}} \quad (3.32)$$

where V_{eff} is the effective volume of the Sun's core calculated by matching the core temperature and the gravitational potential energy of a WIMP particle at the core radius. The annihilation rate given by the following:

$$\Gamma = \frac{1}{2} A^\odot N^2 = \frac{1}{2} C^\odot \tanh^2 \left(\sqrt{C^\odot A^\odot} t_\odot \right) \quad (3.33)$$

with $t_\odot \sim 4.5$ billion years. Neutrino flux is maximized when both annihilation rates and capture rates reach equilibrium, which occurs when

$$\sqrt{C^\odot A^\odot} t_\odot \gg 1 . \quad (3.34)$$

¹The equation for the spin-independent cross section is not used for this work

The result is that we find the relic density dictated mass range of B^1 from section 3.3.1 leads to the equilibrium between the B^1 capture and annihilation rate generally being reached, in other words, the condition of 3.34 being satisfied.

3.3.2 sUED Dark Matter

As mentioned in the section 2.2.4, the sUED model was motivated by the need to incorporate the recent results of some indirect experiments by modifying an existing model. The main objective of this model is to suppress the excess hadron productions by UED model by invoking a 5D bulk Dirac mass term for quarks while keeping KK parity intact. As the production of hadrons is thus suppressed by heavy KK quarks, this provides not only a better fit to the PAMELA anti-proton data but also on electron and diffuse gamma-ray data from Fermi-LAT.

The difference from the UED of having 5D bulk masses for the leptons removes the degeneracies between the LKP from sUED and KK leptons, which could predict a LKP mass between 900 GeV and 1 TeV, from 5 years of WMAP data [70] and this value also fits the Fermi and Hess data.

No further investigation is carried out in this work on sUED dark matter. It is simply noted that the signal can be generated for sUED model dark matter producing a neutrino energy spectrum for future AMANDA/IceCube detector data analyses.

3.3.3 Warped GUT Dark Matter

The LZP, lightest particle from the model of Z_3 stabilized warped GUT is a right-handed neutrino. Actually, it is a four-component spinor and vector-like object, but it is referred to as a Dirac RH neutrino, because only the RH chirality has significant interactions and the other chirality decouples. If the neutrino had the same coupling to the Z as in the standard model, it is excluded by the direct detection experiments. In models with the electroweak gauge group extended to $SU(2)_L \times SU(2)_R \times U(1)$ the RH neutrino has gauge interactions with Z' but with ordinary matter, due to the large gauge boson mass ($\gtrsim 3TeV$) the interaction is weak.

Bounds from Experiments and Relic Density Calculation

Unlike the UED models, there is a large region of parameter space in the model. The two main parameters are: the *c-parameter*, which determines the localization of the wave function for the massless modes along the 5th direction and therefore the size of the Yukawa couplings, and the unified gauge group breaking boundary conditions. The *c-parameter* plotted against the mass of the lzp at four different KK boson

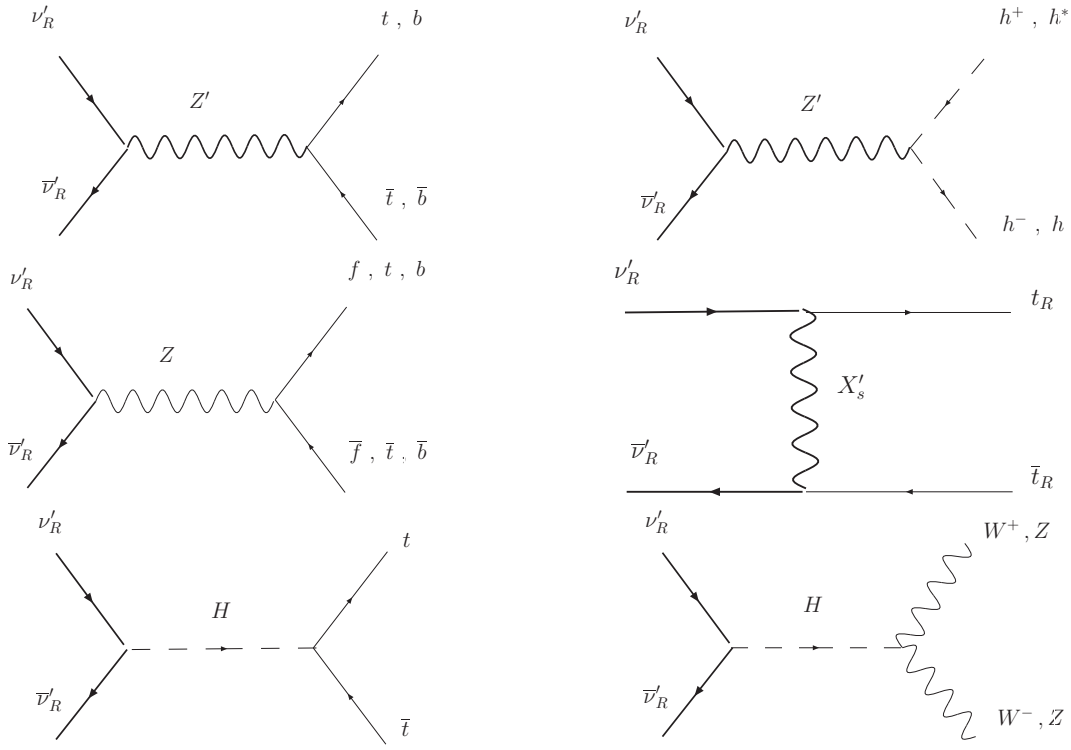


Figure 3.10: LZP annihilation channels
 f denotes all SM fermions other than top and bottom, taken from [32]

mass M_{KK} , is shown in figure 3.11(a). The value of the Z-LZP coupling, $g_z^{\nu'R}$, depends on the which part of the parameter space we choose. Therefore, only the region of the space where the annihilation cross section leads to a thermal density is chosen, and the value of $g_z^{\nu'R}$ is also chosen at a minimal value and at a median value as shown in 3.11(b).

For the generation of signal, three different gauge bosons were chosen at 4, 6 and 10 TeV and for each M_{KK} LZP were evaluated at minimal and median value of $g_z^{\nu'R}$. In considering the annihilation channels, as shown in figure 3.12, for the low mass ranges of LZP ($m_{LZP} \lesssim 100\text{GeV}$) LZPs annihilate primarily through s-channel Z exchange, which gives an annihilation mode very close to the decay modes of the Z. For heavier LZPs, annihilations to top quarks dominate. Top quarks decay into W^\pm and b which both can generate neutrinos. For the signal simulation in 5.2.1 the two different annihilation channels corresponding to the LZP mass ranges was used.

3.4 Dark Matter Detection Efforts

Dark matter detection can be divided roughly into two categories - the direct detection efforts and the indirect detection searches.

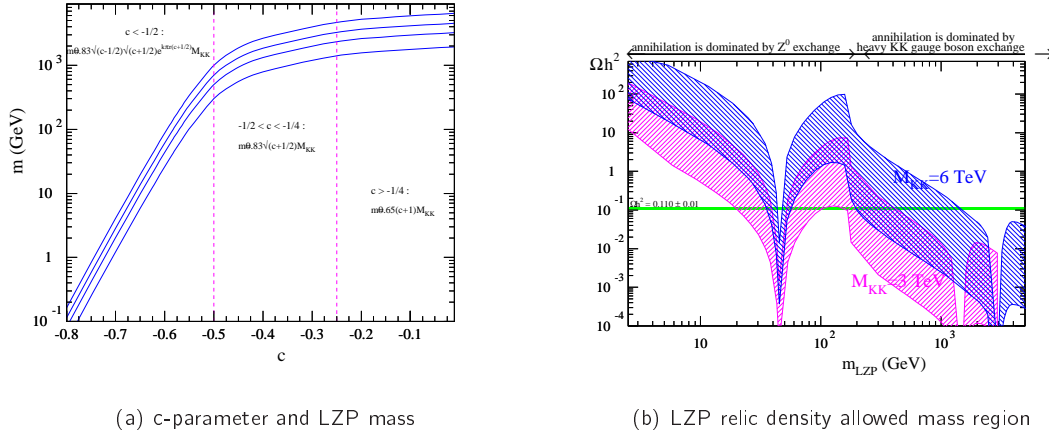


Figure 3.11: The figures show LZP mass restriction from Warped GUT [30]

3.4.1 Direct Detection

Direct detection experiments are specifically designed to look for dark matter collisions with a fixed target nucleus of a crystal, measuring the nuclear recoil in the case of an elastic scattering, and in the case of an inelastic scattering, a signature such as an emission of a photon following the ionization or excitation of the target. The density and the velocity distribution of the WIMPs and the WIMP-nucleon scattering cross section are all that is needed to predict a rate of event, therefore, direct detection experiments give results generally² independent of the theoretical model which WIMPs arise from, and limits on cross-section of the WIMP-on-nucleon are derived.

Axial vector dependent (V-A) interactions depend on the couplings to the spin content of a nucleon. The cross sections for the spin dependent scattering is proportional to $J(J + 1)$ therefore little is gained from using heavier nuclei. However, for a spin-independent(scalar) scattering, the cross section increases with using heavier nuclei. We have already seen in section 3.3.1 that in the Sun, the Kaluza Klein WIMP spin dependent cross section dominates over the spin independent cross section³. The Sun is composed of light elements only, hydrogen and helium, and although only hydrogen contributes to the spin-dependent cross section of the KK WIMP in the Sun, this is much larger in magnitude than the spin-independent cross section.

There are many direct searches for WIMP particles, too numerous to list all here. They include

²Generally, because various assumptions and approximations go into achieving the model-independent attribute - such as assuming that all WIMPs interact via spin-dependent or independent interaction. Also in the case of spin-dependent interaction, a number of assumptions must be made again with regards to the WIMP-proton or WIMP-neutron couplings, a_p or a_n , and their ratios, which depend on the WIMP model. See [71] for a full description

³actually, there is a third component to a WIMP-nucleon scattering, a vector interaction, WIMPs which are not Majorana particles can interact via this, e.g. sneutrinos, however neutralinos and KK DM do not have such component

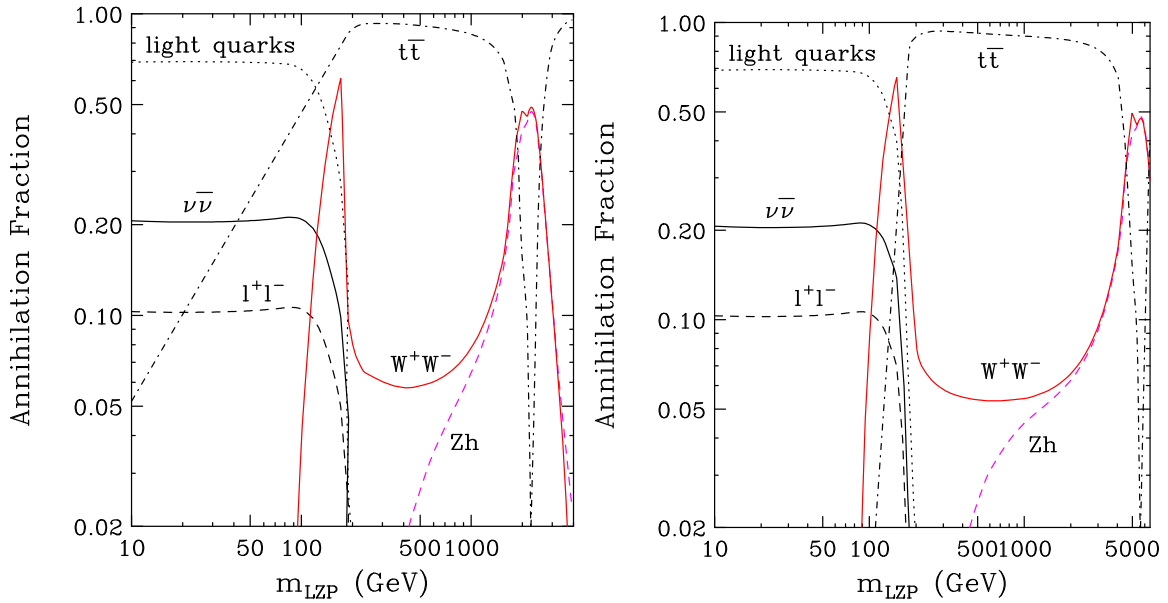


Figure 3.12: Results are shown for $m_{KK} = 4$ and 10 TeV in the left and right frames, respectively, [32]

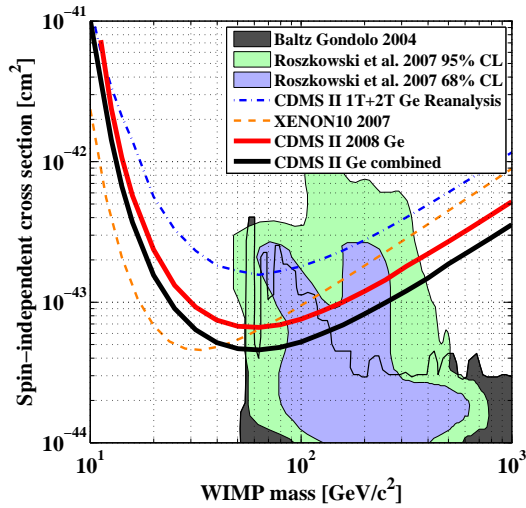
the Cryogenic Dark Matter Search (CDMS II) [72] in Soudan, the DAMA experiment in Grand Sasso, Italy, COUPP [73], CRESST [74], ZEPLIN [75], Edelweiss [76], KIMS [77]. The CDMS experiment uses germanium and silicon crystals in its detector. It has results -see figure 3.13(a) - which are in direct contradiction with the controversial positive result from the DAMA experiment [78] where the NaI Sodium Iodide crystal detector has been used to detect annual modulation in the signal rate induced by the Earth's revolution around the Sun. Many interpretations have been suggested to solve this discrepancy, including performing self-consistency checks on the DAMA results [79] by using the total (unmodulated) rate with energy recoils.

The Korea Invisible Mass Search, KIMS, [77], situated in Kangwon Province in South Korea, is an example which uses Cesium Iodide crystal to detect the WIMP scattering off the nucleus. For a spin dependent cross section limits, this direct detection experiment currently is IceCube/AMANDA's closest competitor.

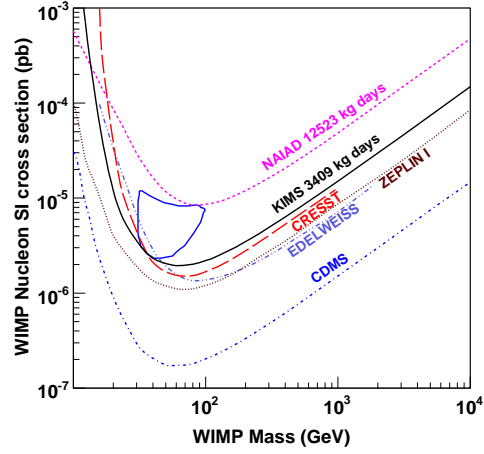
3.4.2 Indirect Detection

Depending on its annihilation products, the dark matter have several indirect detection channels that compliment the direct detection experiments. The philosophy behind this is that the flux of the such radiation is proportional to the annihilation rate, and the annihilation rate in turn is proportional to the square of the dark matter density. It is therefore natural to look for annihilation products in the vicinity of, or in the direction of where there is a high density of dark matter, i.e. massive bodies such as the Earth, Sun and galactic centres as well as the dense regions in the galactic halos.

Using the neutrino telescope constitutes one such effort. However WIMPs can also annihilate into several

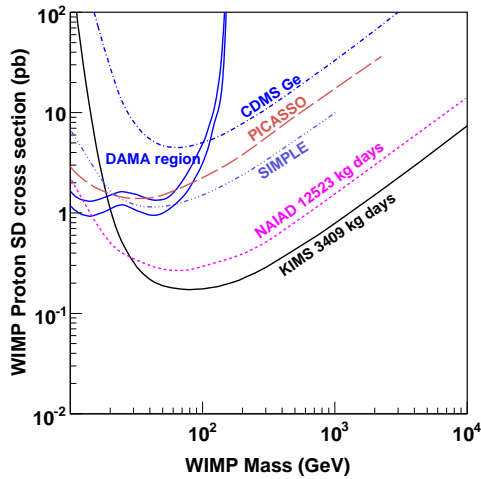


(a) taken from [72]

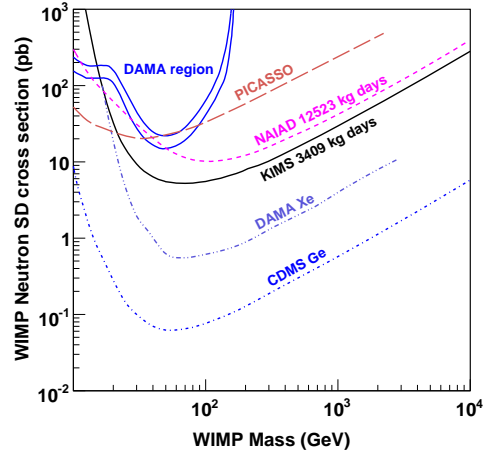


(b) taken from [77]

Figure 3.13: Spin Independent Cross section limits, from two different direct detection experiments (a) Spin-independent WIMP-nucleon cross-section upper limits (90% C.L.) versus WIMP mass. The upper curve (dash-dot) is the result of a re-analysis of a previous dataset - The upper solid line is the result from [72]. The combined CDMS limit (lower solid line) has the same minimum cross-section as XENON10(dashed) reports, but has more sensitivity at higher masses. Parameter ranges expected from supersymmetric models are shown (95% and 68% confidence levels in green and blue, respectively)



(a) Exclusion plot for the SD interaction in the case of pure proton coupling ($a_n = 0$) at the 90% confidence level



(b) Exclusion plot for for the SD interaction in the case of pure neutron coupling ($a_p = 0$) at the 90% confidence level

Figure 3.14: Spin Dependent Cross section limits from KIMS taken from [77]

other particles including positrons and electrons, gamma-rays and anti-protons.

- **Gamma-Ray experiments**

Gamma Ray emission from the galactic centre provide us with a good detection candidate for dark matter annihilations. However at the energies of interest to us, which is of GeV to TeV, the photons will interact with matter via pair production of e^+e^- with an interaction length of $38g\text{ cm}^{-2}$ which means ground based gamma ray telescopes like MAGIC [80], CANGAROO [81], and H.E.S.S [82] will not be able to observe it directly. However, by distinguishing the Cherenkov light from the cosmic-ray and gamma-ray induced air showers, they are able to perform ground-based gamma-ray detection.

The space-based telescope EGRET, [83] which has reported seeing an excess of gamma rays in the region of the galactic center, was the first example of a space-based gamma-ray telescopes. It was the predecessor of GLAST (Gamma-Ray Large Area Space Telescope) which was launched in 2008, renamed FERMI-LAT, which has been taking much valuable data for the whole field of particle physics and astronomy. Fermi sees gamma ray originating from the cosmic ray interaction with the interstellar medium(ISM) i.e. π_0 , inverse Compton scattering and the bremsstrahlung components. It is also hoping to look for dark matter contribution from direct production of gamma rays from annihilation or decays, or through interaction of its annihilation or decay products with the ISM.

For neutralinos, models such as the constrained MSSM has been further constrained with the data from nine months of FERMI LAT operation as shown in Figure 3.15 taken from [84]. The analysis was performed on the spectrally and spatially resolved photon counts from the FERMI data, to fit the cMSSM parameter space-varying dark matter annihilations profile from Segue 1, a dark matter dominated small satellite galaxy in the Milky Way.

- **positron and anti-protons**

There is a focus on searching for anti-particles in indirect searches. Dark matter particle annihilation provides as many anti-particles as particles, which makes them an easier target over the rare anti-particles produced in ordinary cosmic ray interactions. Additionally, dark matter induced anti-matter may have specific spectral properties. HEAT and BESS were both balloon-borne experiments. HEAT measured the cosmic-ray electron and positron spectrum while BESS has observed anti-proton spectrum. In the balloon flight in 1994-1995 HEAT reported seeing an excess of positron flux with a peak at 9GeV, which was subsequently confirmed in 2000 by another flight. BESS has taken data of the cosmic anti-proton spectrum in the range of 200MeV to 3 GeV.

PAMELA [40] is a satellite experiment which measures spectra of both positrons(50GeV to 270GeV)

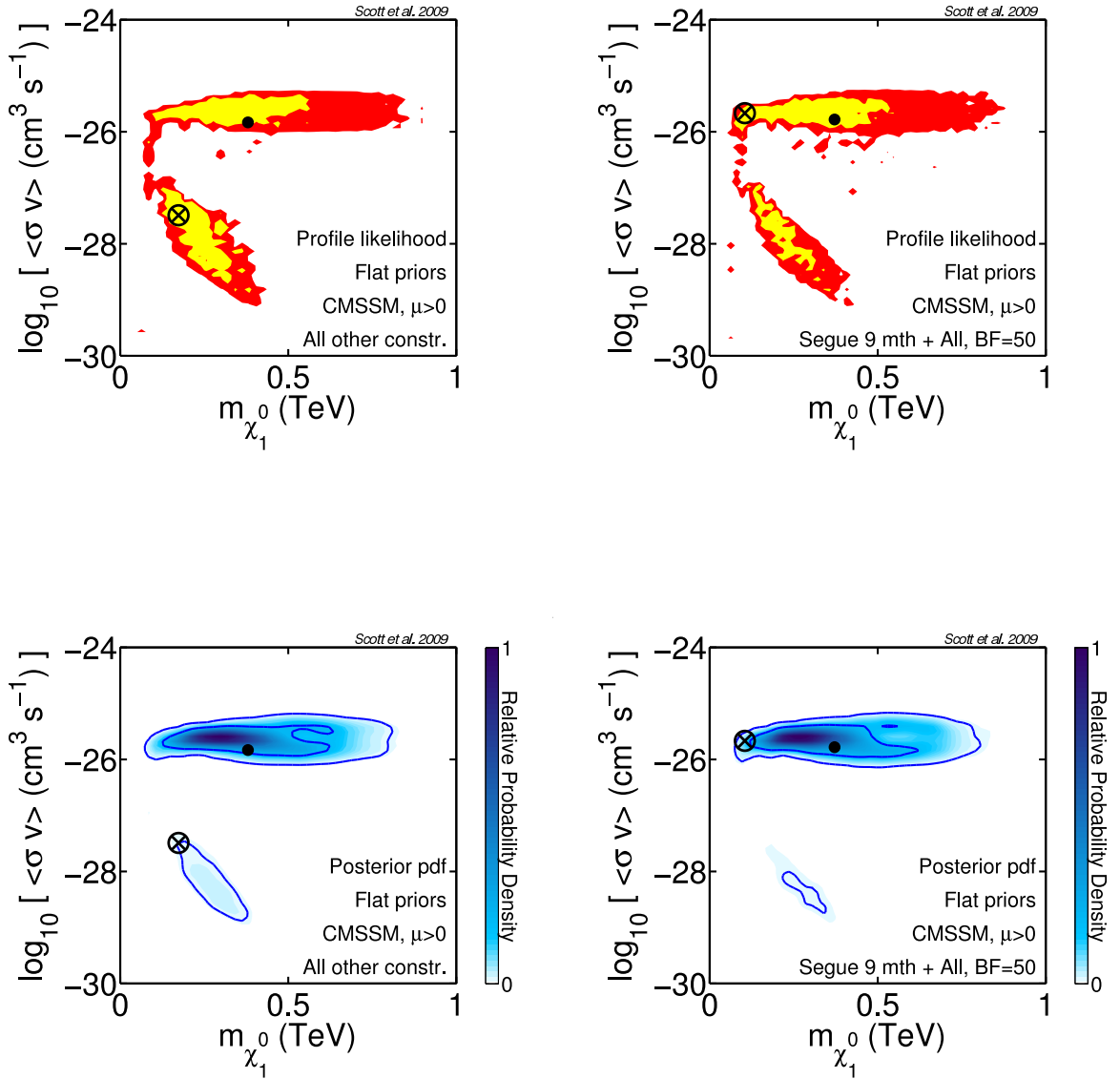


Figure 3.15: WMAP-compatible annihilation cross-sections in the CMSSM, assuming the neutralino to be the dominant component of dark matter. Favoured regions are as implied by existing experimental data only (*left*), and with the addition of 9 months of Segue 1 observations by FERMI (*right*). Upper plots show profile likelihoods (where yellow and red indicate 68% and 95% confidence regions respectively), while lower plots show marginalised posterior PDFs (where solid blue contours give 68% and 95% confidence regions). Solid dots indicate posterior means, whereas crosses indicate best-fit points. [84]

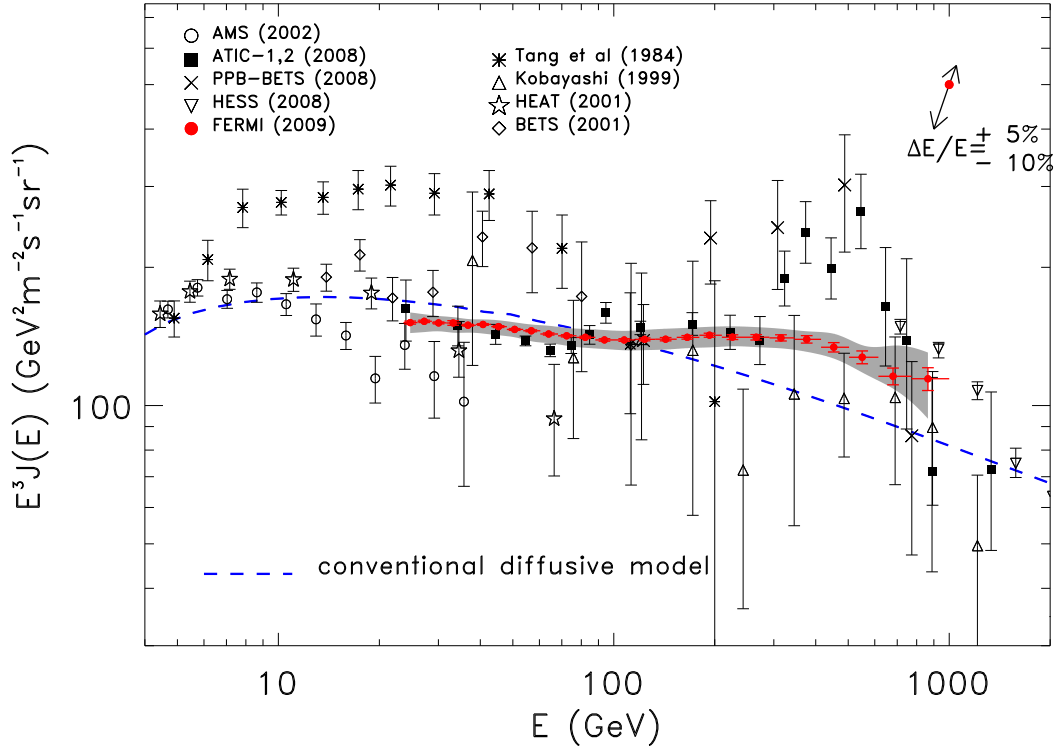


Figure 3.16: The Fermi LAT CR electron spectrum (red filled circles). Systematic errors are shown by the gray band. The two-headed arrow in the top-right corner of the figure gives size and direction of the rigid shift of the spectrum implied by a shift of $^{+5\%}_{-10\%}$ of the absolute energy, corresponding to the present estimate of the uncertainty of the LAT energy scale. Other high-energy measurements and a conventional diffusive model [85] are shown.

and anti-protons(80MeV to 190GeV). It has measured an increase in the positron energy spectrum above 10GeV. As the secondary positron spectrum coming from CR interactions with the interstellar gas drops with energy, it has a softer spectrum than the primary electron spectrum. In the absence of a primary source, the surprising upturn in the positron fraction has led many to suggest the existence of a primary source with energies in the range 10GeV to 100GeV, including astrophysical sources such as pulsars and dark matter.

ATIC [38] measured a broad excess in the range of 300 to 700 GeV of the total e^+ and e^- spectrum with a sharp cutoff at the high energy end of the excess which is shown in figure 3.7. PPB-BETS [39] also verified this data. However this was not seen by the recent Fermi LAT which has on board design that looks for the cosmic ray electrons. The Fermi result over a similar range of energy where despite seeing a hardening at around 80GeV. Between 100 and 500 GeV it is well within the power law with a harder index, with a break at a high energy as shown in their latest result in figure 3.16 from [42]

- **Neutrinos**

Neutrinos do not interact easily, therefore, as a dark matter probe, it has the advantage over the others of travelling directly from a possible source of a dark matter density well in a near-straight line. This allows us to use even a point-source analysis to derive a limit for the dark matter annihilation. The details of using neutrinos for WIMPs search will not be explained here as it forms the rest of the work.

Neutrino telescopes are operating which use the neutrino induced Cherenkov photons to search for astrophysical neutrinos. Both water and ice are used as the detecting medium. Each has their own advantages and disadvantages. While the absorption length of light in ice is larger than that in water the scattering length is shorter. Also ocean based telescopes suffer from the presence of bio-luminescence from deep-sea organisms which produce light, either when they emit photons spontaneously or when they interact with the detector. Water detectors include ANTARES [9], NEMO [86] and NESTOR [87]. The three experiments have merged under one entity, the KM3NET consortium, and this is in its preparatory stage at the moment to build a large neutrino telescope [88] under the Mediterranean sea at a scale comparable to IceCube. It hopes to detect neutrinos from the southern sky - and look for the supernova remnants, micro-quasars, and unassociated gamma-ray sources reported by the H.E.S.S. which is beyond the reach of IceCube.

Ice is used as a detecting medium by AMANDA/IceCube and further details are given in subsequent chapters.

Chapter 4

Neutrino Detection and AMANDA/IceCube

4.1 Detector Overview

IceCube is a large neutrino detector at the South Pole, nearing its construction completion in the Antarctic summer season of 2010-2011. The name derives from the km^3 scale volume of the detector. The **Antarctic Muon And Neutrino Detector Array** (AMANDA) was¹ a precursor to the IceCube detector. Like IceCube, AMANDA also started its life with a small number of strings, starting with 4 strings only in AMANDA-B4 in 1995 and went through a series spanning AMANDA-A and AMANDA-B with increasing number of strings. AMANDA-II was the last and the full capacity version with 19 strings and it was completed in 2000. AMANDA took data for over a decade before the final switch off in 2009. It served as a successful prototype so that the IceCube could be built on a much larger scale.

The AMANDA-II detector (see figure 4.1) at its completion, had 677 optical modules (OM) attached to 19 strings. Most of the OMs are located between 1500 m and 2000 m below the surface. Each OM is a glass pressure vessel, which contains an 8-inch hemispherical photomultiplier, or PMT.

IceCube was built on AMANDA with various technical improvements. However although IceCube has a larger instrumented volume than AMANDA, the spacing between strings is greater (see figure 4.2). Due to its denser volume, AMANDA-II had a lower energy threshold for detecting neutrinos giving it an advantage over IceCube for detecting WIMPs with masses in the sub-TeV regime. Subsequently the Deep Core Project has been incorporated into IceCube in 2009/10, improving its low energy capabilities by a denser string spacing in the detector centre.

¹the AMANDA-II ceased operation in May 2009

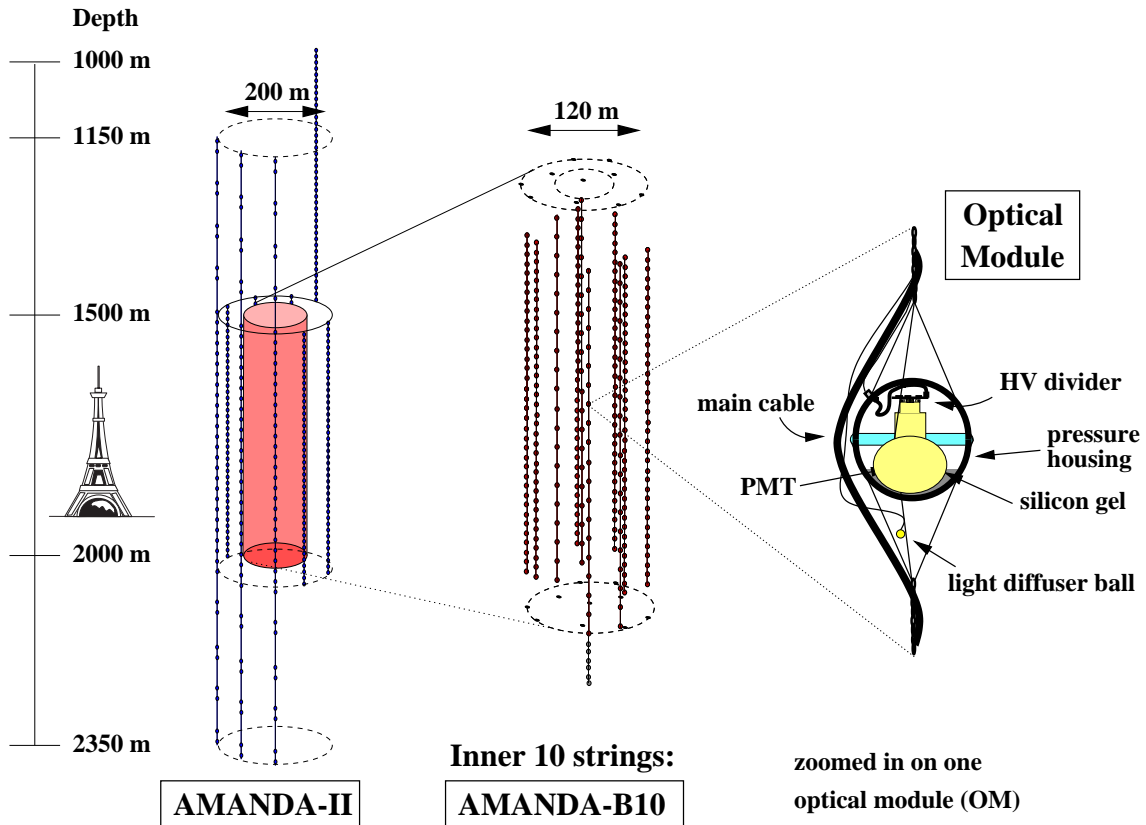


Figure 4.1: The AMANDA-II detector. c.f. Eiffel Tower for scale

4.2 Neutrino Detection via Cherenkov Light Detection in Ice

4.2.1 Neutrino Nucleon Interaction in Ice

A charged current interaction in ice between a high energy neutrino and the nucleon, N can create a lepton and a hadronic cascade:

$$\nu_\ell + N \rightarrow \ell + X, \quad (4.1)$$

In all cases the charged particles produced emit Cherenkov photons, which are detected by the AMANDA PMTs - see figure 4.1.

Each lepton flavor - electron, muon or tau - generates a different signal in the detector, The AMANDA-II is primarily a muon neutrino detector, in the sense that most analyses utilizes the muon channel only. However, AMANDA-II also looks for electromagnetic cascades created from electron neutrinos which have a spherical light distribution as the cascade does not travel a large distance and the light is scattered. Taus also decay and produce hadronic cascades but tau events at high energy such as a few PeVs can produce very specific signature such as a *double bang event* where two extremely bright cascades unique for high-energy ν_τ occur one after another. Usually the other two channels suffer from having a worse angular resolution than the long muon tracks, and also a larger instrument volume is

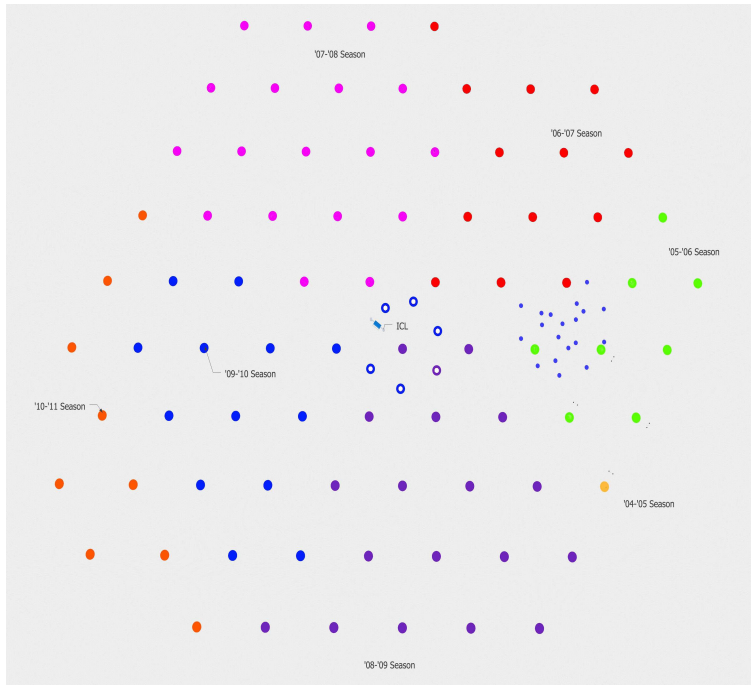


Figure 4.2: AMANDA-II and IceCube string configuration
IceCube strings deployed by season and AMANDA-II strings are shown in small solid blue dots in the diagram

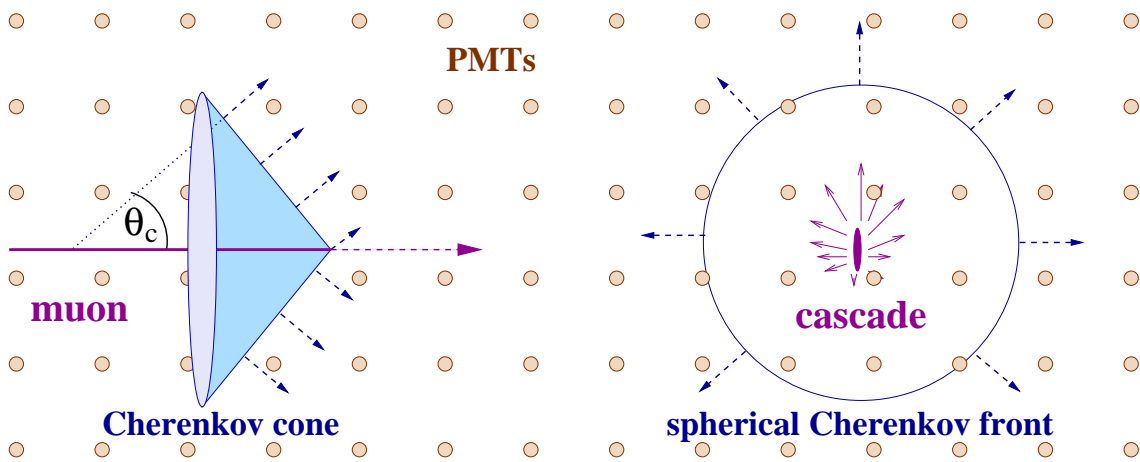


Figure 4.3: Detection modes of the AMANDA detector: Left: muon tracks induced by muon-neutrinos; Right: Cascades from electron- or tau-neutrinos.

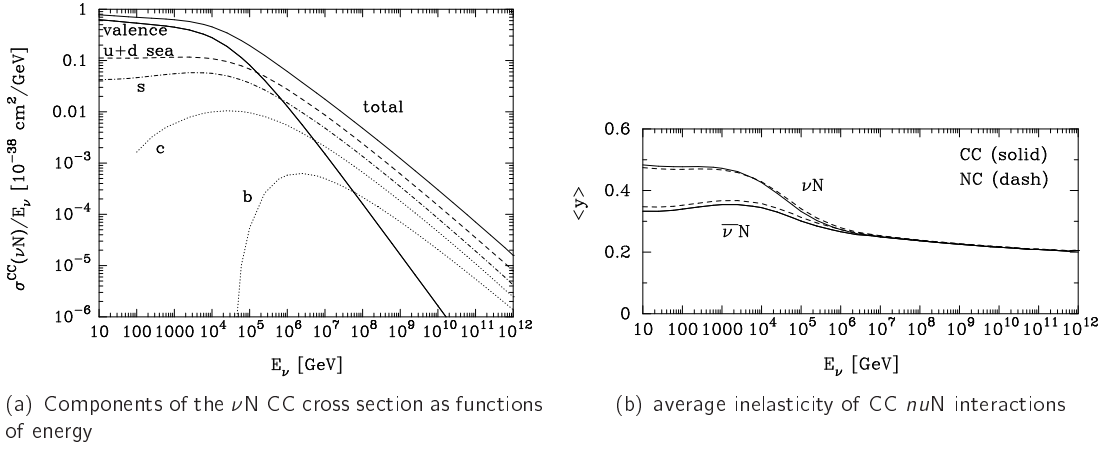


Figure 4.4: Charged Current νN Cross Section
both figures taken from [89]

needed for detection due to the interactions having to be close to the detector to be identified. In a diffuse analysis, due to the backgrounds from atmospheric neutrinos being smaller, the ν_e and the ν_τ channel have some advantages as the energy resolution is significantly better since the full energy is deposited in or near the detector.

In WIMP analyses only the muon channel is used as at the low energy regime of WIMP detection the cascades are too difficult to isolate from background.

The neutrino nucleon interaction cross section has been studied by Gandhi, Quigg Reno in [89, 90]. The differential cross section for a charged current interaction can be written in terms of the Bjorken scaling variables x and y as:

$$\frac{d^2\sigma}{dx dy} = \frac{2G_F^2 M E_\nu}{\pi} \left(\frac{M_W^2}{Q^2 + M_W^2} \right)^2 [xq(x, Q^2) + x\bar{q}(x, Q^2)(1-y)^2], \quad (4.2)$$

Here, $x = Q^2/2M\nu$ and $y = \nu/E_\nu$, $-Q^2$ is the invariant momentum transfer between the neutrino and the muon, $\nu = E_\nu - E_\mu$ is the energy loss in the lab frame, M and M_W are the nucleon and intermediate-boson masses, and $G_F = 1.16632 \times 10^{-5} \text{ GeV}^{-2}$ is the Fermi constant. This relation can be assumed linear in the mass range between 1 GeV and 10 TeV .

The parton distribution functions $q(x, Q^2)$ and $\bar{q}(x, Q^2)$ are given by

$$\begin{aligned} q(x, Q^2) &= \frac{u_v(x, Q^2) + d_v(x, Q^2)}{2} + \frac{u_s(x, Q^2) + d_s(x, Q^2)}{2} \\ &\quad + s_s(x, Q^2) + b_s(x, Q^2) \\ \bar{q}(x, Q^2) &= \frac{u_s(x, Q^2) + d_s(x, Q^2)}{2} + c_s(x, Q^2) + t_s(x, Q^2), \end{aligned} \quad (4.3)$$

where the subscripts v and s label valence and sea contributions, and u, d, c, s, t, b denote the distributions for various quark flavours in a *proton*.

Interestingly, this also highlights the difference in cross section between the neutrino-nucleon interaction and antineutrino-nucleon interaction.

4.2.2 Muon Transportation in Ice and Energy Loss

A muon in ice loses energy via various processes including:

- ionization
- bremsstrahlung
- photo-nuclear interaction
- electron pair production
- LPM suppression of bremsstrahlung and pair production
- decay

However, most of these can be characterized via a simple formula:

$$\frac{dE}{dx} = a(E) + b(E) \cdot E. \quad (4.4)$$

In ice, the value for a and b are found to be $a \approx 0.2\text{GeVm}^{-1}$ and $b \approx 3 \cdot 10^{-4}\text{m}^{-1}$ from [91].

The average final distance (range) for each energy, x_f , to the solution of the above is expressed as :

$$x_f = \log(1 + E_i \cdot b/a)/b \quad (4.5)$$

At high energies the stochastic processes are important, so this is simulated via an AMANDA specific package which performs the numerical simulation. A high-energy ν_μ charged current interaction creates a muon, not deviating much from the initial neutrino direction (having a mean deviation angle of $\psi = 0.7^\circ \times (E_\nu/\text{TeV})^{-0.7}$ from [92]). This requires the muon reconstruction resolution to be $\lesssim 1^\circ$ at energies above 600GeV.

While the muon is travelling at a speed faster than that of the light, it continuously emits Cherenkov photons. A relativistic muon thus created emits a cone of Cherenkov light at the fixed angle of $\theta_c \approx 41^\circ$, from $\cos \theta_c = (n \cdot \beta)^{-1}$, where $n \simeq 1.32$ is the index of refraction in the ice and $\beta \simeq 1$.

4.2.3 Photon Transport in Ice

A very important aspect of the detector comes with the simulation of the photon propagation in ice. The absorption and scattering of photons are the two main depth and wavelength dependent effects. Absorbed photons contribute to a reduction in photon count, and scattering contributes to delays in the measured arrival times. With pure ice, there will be no diffraction, and indeed at the depth of AMANDA it was hoped that this would be the case. The contribution of air bubbles to scattering decreases with depth, and at greater depths than 1.4km scattering by dust dominates.

There have been several careful studies performed within the AMANDA/IceCube collaboration. [93–95]. In [94], the result from using four different kinds of **pulsed** light sources (including a YAG laser, two nitrogen lasers and LED flashers at two different wavelengths) and two different **steady** light sources were employed to measure the effective scattering length, and the absorption length at various depth of the ice. First, we start with introducing λ_s , the average path length between two scatter centres defined as:

$$\lambda_s = \frac{1}{n_{centre} \langle \pi r_{centre}^2 \rangle} \quad (4.6)$$

with n_{centre} the number density of the medium. Mie scattering theory is applied to a strongly forward peaked anisotropic scatters, where the scattering is not isotropic to achieve a total effective length of light transport:

$$\lambda_e = \lambda_s \sigma_{i=0}^n \langle \cos \theta \rangle^i, \quad (4.7)$$

which for large n approximates to

$$\lambda_e = \frac{\lambda_s}{1 - \langle \cos \theta \rangle}. \quad (4.8)$$

The scattering and absorption of light in ice are characterised by the effective scattering and absorption coefficients. These are defined as follows:

The effective scattering coefficient is defined as

$$b_e = \frac{1}{\lambda_e}. \quad (4.9)$$

The absorption coefficient, on the other hand, is defined by

$$a = \frac{1}{\lambda_a}. \quad (4.10)$$

Price and Bergström have introduced an empirical model which describes the wavelength dependence of the absorptivity of ice from UV to IR wavelength in [96]. There are three components which parametrize

the absorption coefficient:

$$a(\lambda) = A_U e^{-B_U \lambda} + C_{dust} \lambda^{-\kappa} + A_{IR} e^{-\lambda_0/\lambda}. \quad (4.11)$$

The first term describes an *Urbach tail* which is a steep exponential decrease in absorption coefficient which occurs at slightly longer wavelengths than that of an electronic band-gap energy. The second term is due to insoluble dust particles in the ice, with C_{dust} proportional to dust concentration, and the last term, an approximation of the exponential rise in the red and infrared due to molecular absorption by pure ice.

The measurement of both coefficients are illustrated in Figures 4.5 and 4.6. The effect of dust layers

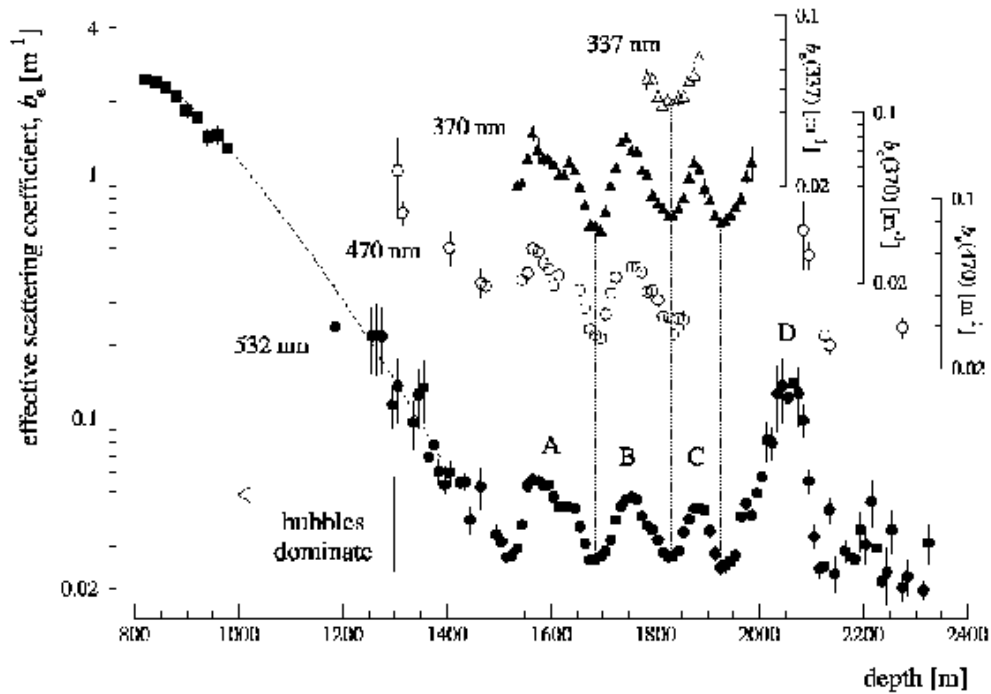


Figure 4.5: Depth dependence of the effective scattering coefficient

Four peaks labeled A to D correspond to stadials in the last glacial period. A broad dust peak due to the Last Glacial Maximum, expected at 1300m is masked by bubble scattering. The points between 800 and 1000m, where scattering is dominated by bubbles and does not depend on wavelength, are weighted means of a previous study at 410nm to 610nm. Figure from [94]

resulting from different geological time period are very clearly seen. Of these, the depths between 800 and 1000m correspond to the onset of a period called the *Holocene*, which continues to the present day from 11,700 years ago, with relatively low dust concentration and a mild global climate. The *Last Glacial Maximum* or LGM, a time where the maximum extent of glaciation occurred in the Last Glacial Period, or what is commonly known as the Ice Age. LGM occurred at around 23,000 years ago, corresponding

to a depth of 1300m in South Pole ice with increased dust concentration. Finally, the specific dust layer peaks shown in the figures refer to *stadials* which are times of colder periods during an interglacial period.

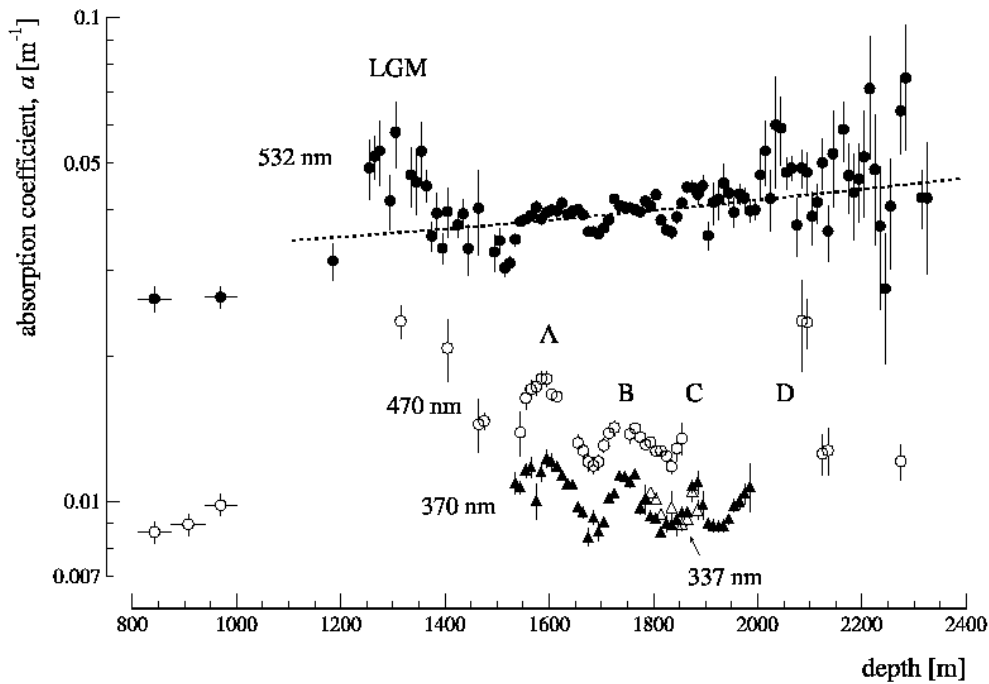


Figure 4.6: Depth dependence of the absorptivity

Measured with pulsed sources at four wavelengths. At 532nm the ice component dominates and is superimposed on smaller variations due to dust, and the dashed line outlines a 1 percent per Kelvin increase in absorptivity with temperature. The broad peak at 1300m is due to the Last Glacial Maximum. At shorter wavelengths the dust peaks at A,B,C are clearly seen. figure taken from [94]

4.3 Detector Hardware, Trigger Class and Calibration

Due to the history of the AMANDA-II detector, the hardware setting information of the detector was non-uniform. This includes the detector geometry, the electronic behaviour for the different channels (OMs), and trigger conditions which need to be simulated accordingly (see 5.2). Therefore, the detector settings were saved separately in individual files for the corresponding time period.

4.3.1 Geometry, OM characteristics

The geometry of the AMANDA-II was briefly mentioned in Section 4.1. The 677 OMs attached to the 19 strings were located at a depth between 1500m and 2000m in a volume in the shape of a cylinder with radius 100m and a height of 500m. The spacings between the OMs range from from 10 to 20m.

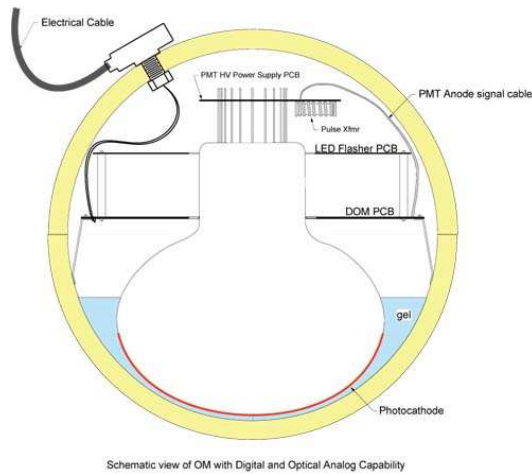


Figure 4.7: A generic digital optical module

The Figure shows pressure sphere, optical coupling gel, PMT, signal processing electronics board, LED flasher board, PMT base and electrical penetrator from [97]

The OMs vary in their response and their individual characteristics are incorporated into the detector simulation. The variations have their origin in a range of effects. For instance the OMs are made from two types of glass, Billings (OMs 1-86) and Benthos (OMs 87-680). Billings' sensitivity was estimated to be around 85 percent of the sensitivity of the Benthos and the relative sensitivity for each individual PMT is available from the Hamamatsu (the manufacturer of the PMTs). The OMs also have different noise rate, and different afterpulse probability. The typical noise rate of an AMANDA OM is around 1 kHz, mainly due to the radioactivity in the spheres and some spheres are more radioactive quiet than others.

4.3.2 Muon Data Acquisition System

The AMANDA-II detector employs a multiplicity trigger, in which events are triggered, that is, recorded when there are a certain number of hit optical modules within a certain time window. The trigger logic is called the DMADD (Discriminator and Multiplicity Adder Device) where each OM hit amplified by a SWedish AMPlifier or (SWAMP) or an Optical Receiver Board (ORB)² gives an electrical signal to a discriminator if the threshold of the discriminator is reached. At certain intervals the DMADD checks how many of the generated pulses overlap, and the number of overlapped pulses give the multiplicity. The generated pulse is then passed onto the Time to Digital Converter which measures the leading and the trailing edge of the pulse. A delayed output is received later by the peak sensing Analog to Digital Converter (pADC) which records the maximum pulse amplitude within the pulses in a 6 μ s window around the trigger time. The four strings deployed in 1995/1996 had the OMs connected to the surface via coaxial cable that transmitted both the HV and the analog anode signal (see left most figure of 4.8), while the time offset calibration t_0 was measured separately from the surface to a diffuser ball close to the OM

²The coaxial and twisted pair cables are connected to SWAMP, whereas the optical cable goes to the ORB

through an optical fiber. However in 1996/1997 the coaxial cable was replaced by twisted-pair cables for the 216 OMs deployed on six strings (strings 5 to 10), which resulted in the attenuation and the dispersion being reduced significantly. In 1997/1998 three test strings (strings 11-13) used optical fibers on all OMs both for calibration and for the analog transmission of the PMT pulses. The obvious advantages of optical analog transmission compared to the electrical analog technique consisted of the high bandwidth, double pulse resolution improvement, a higher dynamic range, no correction for the amplitude-dependent time slewing needed and no pick-up of EM noise nor cross-talk. The dAOMs(digitally controlled analog optical module) and the DOMs (Digital Optical Module) where the digitization of the signal is performed under ice both are shown in the right two pictures of the 4.8. The DOMs make the use of the same HV generator as the dAOMs but do not need an optical fiber cable because the signal is already digitized. In the final deployment season of 1999/2000 when six strings were deployed, out of the 251 OMs, 189 used the improved passive analog optical transmission system with the electrical backup. 23 OMs were of the dAOM type(10 with LED and 13 with Laser diode transmitters), and 41 were of the DOM type with LEDs.

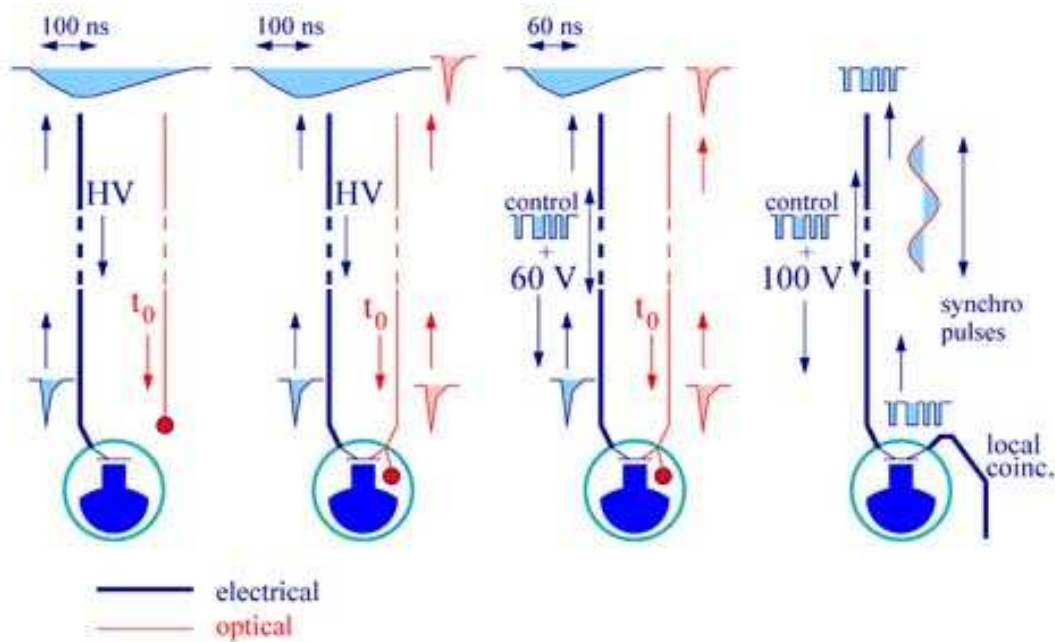


Figure 4.8: The AMANDA OMs

From left to right, electrical signal transmission, passive optical signal transmission, active optical signal transmission(dAOMS) and digital signal transmission from [97]

4.3.3 Pulse shape and time slewing

Depending on which type of cable the OMs were connected to the surface by, the pulse shape produced by the DMADD (see 4.3.2) varied considerably. For example, an OM connected by a coaxial cable produced a pulse with a width of around 600ns whereas the OM connected by an optical cable produced a much

narrower width of 5ns. Related to this property, the most important pulseheight dependent feature of the electrical channels is called time slewing. A pulse with a higher amplitude gives the discriminator a signal earlier than one with a smaller amplitude even if they start at the same time, as shown in Figure 4.9. The quantity α (see Section 4.3.5), is obtained by plotting the time delay due to the pulse shape against $\frac{1}{\sqrt{\text{amplitude}}}$ from equation 4.12. The effect of time slewing is taken into account during calibration, in order to make sure that true time is derived from measured time.

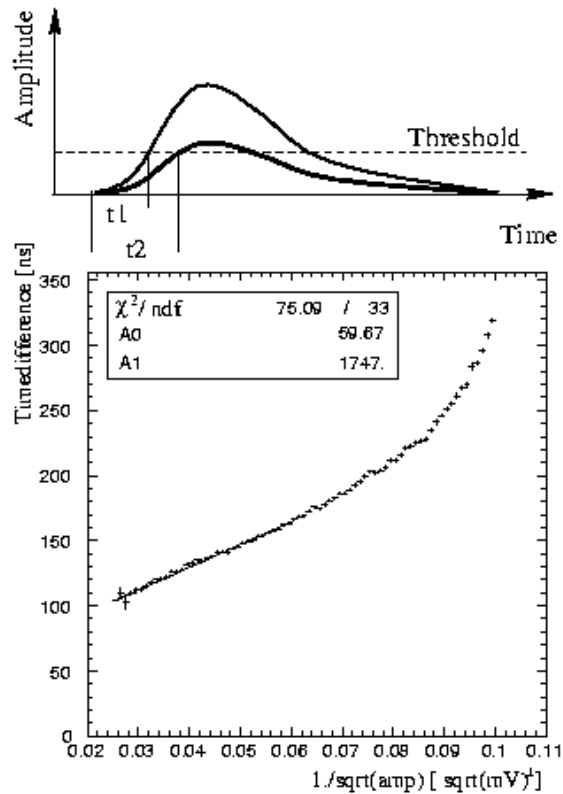


Figure 4.9: The AMANDA detector time slewing effect

The top figure shows the time slewing effect and the bottom plot shows the plot of the time delay due to the pulse shape vs the $(\text{amplitude})^{-1/2}$

4.3.4 Trigger Class

The main trigger condition used for AMANDA-II was the M24 trigger. This was a simple multiplicity trigger which required at least 24 modules hit within a time window of $2.5 \mu\text{s}$. A number of external triggers based on coincident events with other detectors (e.g. SPASE) exists, but these were not utilized for the analysis. Once the trigger condition was satisfied, the time and channels were read out by the DAQ mentioned in section 4.3.2.

The requirement of 24 hit modules in a $2.5 \mu\text{s}$ window used by the multiplicity trigger was chosen to reflect the compromise in the high and low energy events. Less than 24 hits might allow too many

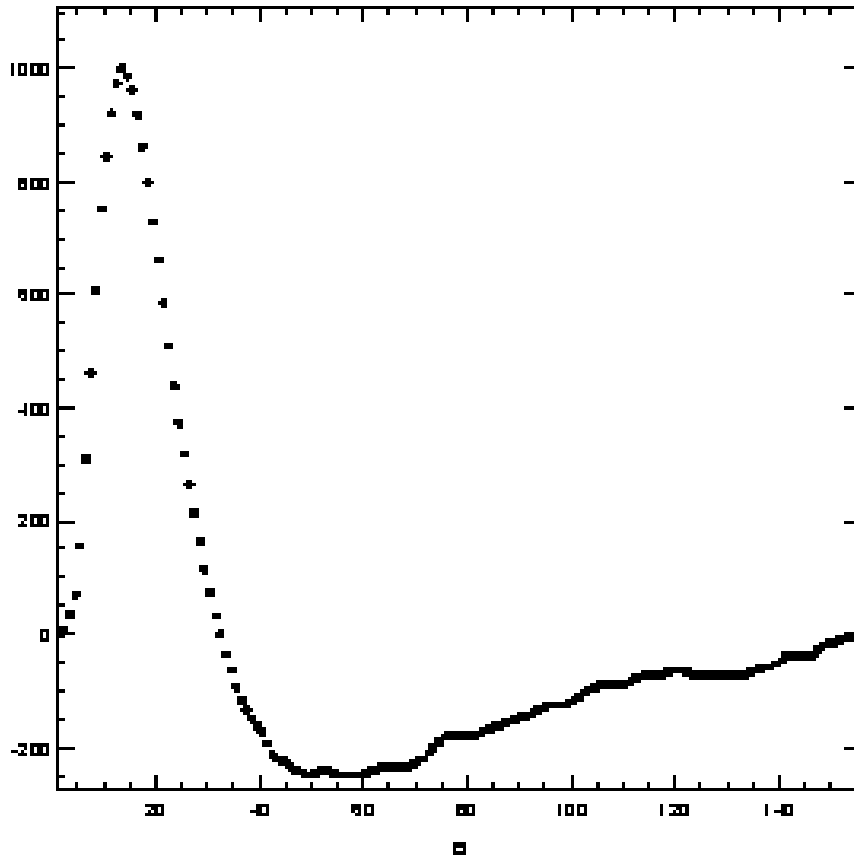


Figure 4.10: The digitised pulse of a coax OM in AMANDA. X-axis is in bins of 25ns

atmospheric muons which are of low energy, and increasing it would reduce the trigger efficiency for the low energy neutrinos. The string trigger condition addressed this by requiring a certain number of hits in a certain number of consecutive modules on a string. The numbers of the modules depend on the relative position of the string - whether the string is one of the inner four strings or the outer strings (with smaller vertical spacing between the OMs). This allowed for those events which had not triggered the M24 trigger to be recorded and saved many low energy events which are vital for the WIMPs analysis. The multiplicity trigger condition was kept uniform throughout but the string trigger changed its condition several times during the analysis period and this is taken into account in the analysis. More detail on the non-uniformity of the string trigger is explained in section 5.3.1.

4.3.5 Calibration

The calibration of the detector was performed on the following information, using the laser diode and the diffuser ball:

- **Time**

For all OMs in the array, pulses were sent from laser diode to the diffuser balls below the OM. Since the distance to the diffuser-ball is measured accurately with an Optical Time Domain Reflectometer, the photons from the diffuser ball immediately hits the PMT photo-cathode and enough calibration data collected this way can provide us with α and t_0 from fitting to the following equation:

$$t_{true} = t_{measured} - t_0 - \frac{\alpha}{\sqrt{amplitude}} \quad (4.12)$$

After calibration, the arrival time of a photon at PMT is known within 5ns precision. When DAQ components or settings are changed the calibration constants are revised by sending the pulses from the laser diodes.

- **Geometry**

In order to deduce the exact relative positions of the OMs unscattered photons from the laser pulsed diffuser ball of one OM to another OM was used. Knowing the time when the pulse is injected, and the time calibration constant already derived, relative position of the OMs were measured to a 0.5 to 1m precision.

- **Amplitude**

Several pulses from different photons can merge into one long hit. The amplitude is increased accordingly. For each OM we could find the mean amplitude of a single photo-electron, $pADC_{spe}$ from fitting the atmospheric muon induced photons to a Gaussian peak. The number of photons was found by converting the measured pADC value by dividing it by the $pADC_{spe}$. The linearity of the amplitude holds up to less than 5 number of photo-electrons. The calibration is performed based on individual OMs.

4.4 Physics Searches with AMANDA and IceCube

Various other searches for astrophysical phenomena are possible with the AMANDA/IceCube detector.

Relatively well-established astrophysical phenomena which could provide neutrinos for detection via certain model-dependent mechanism include the proton blaza model for AGNs and relativistic fireball model for GRBs provide a source of neutrinos at energies that can be detected via the AMANDA/IceCube detector. Other sources specifically related to stars include the supernova, which, if used with a early warning system, the elevated level of low noise of a large Cherenkov detector during the period could point to the low-energy neutrinos from a supernova. Some models also suggest that supernova could provide a higher energy neutrino source via proton acceleration which could interact inside the supernova remnants(SNRs) or inside the shell. Moon Shadows of muons were observed successfully by IceCube with 40-string configuration and this is an important result [98] to show that the detector is working as

it should.

Apart from WIMPs, there are searches for non-standard physics performed on magnetic monopoles, quantum gravity, i.e. the cross section discrepancy from models with extra dimensions, [99], neutrino oscillations etc.

Chapter 5

Analysis

5.1 Analysis Overview

In order to search for the Kaluza Klein WIMPs using AMANDA-II, we employ the Sun as a gravitational trap for the WIMPs to accumulate over the years. This chapter contains a description of the analysis. Our goal is to detect neutrinos from dark matter annihilation in the centre of the Sun. The challenge lies in isolating the neutrino events from the huge background of cosmic ray muons which also trigger AMANDA. This is achieved through a sequence of filtering steps. Even when the cosmic ray muon background has been removed there will always be an irreducible background of atmospheric neutrinos present which are neutrinos produced by cosmic ray interaction. On an event by event basis they can not be distinguished from the neutrinos which are produced as a result of DM annihilation. So our strategy for detection of DM induced neutrino is to look for an excess over the atmospheric neutrino background.¹.

The analysis itself consists of two broad stages - simulation and filtering. The simulation of the signal Monte Carlo, background and their subsequent propagation and detector response is described in section 5.2. Simulated data and experimental data are reconstructed and filtered in parallel in the early filtering stages. Through several stages the atmospheric muon background data is reduced until the irreducible background, or atmospheric neutrino background dominates. This is described in the section 5.4. At this level we are able to rely on statistical methods to deduce a result on the actual annihilation rate of WIMPs in the Sun. An important point to note is that we do not assume a priori the number of annihilation of WIMPs during the period of detector response. It is sufficient to generate enough events to give a distribution of the neutrino energy spectrum. This result can then be utilized in giving useful information such as the muon flux at the detector that would be expected if the WIMPs annihilation rate was the one obtained by the analysis or the cross section of the WIMP on proton scattering, which can

¹Solar neutrinos at MeV range fall below the energy of detection. There also exists cosmic ray interactions with the solar atmosphere which also produces neutrinos but the rate which is expected to be very low according to [100]

be useful for comparisons with other experiments searching for WIMPs.

5.2 Simulation

To see if there is a statistically significant excess of neutrinos that have come from the Sun that can be attributed to the annihilation of dark matter particles, one must first simulate both the signal we are expected to see and the background. Various simulation methods which include some AMANDA-specific programs as well as modified packages were used for the simulation of signal and background and their subsequent propagation to the detector and the detector response.

5.2.1 Simulation of Signal Monte Carlo

Much of the physics behind the Kaluza Klein WIMP model has been covered already in the previous chapters. The constraints on the mass of the WIMPs come from the relic density argument and the particle physics (see section 3.3).

One of the most important concepts in the WIMPs analysis lies in the fact that only the shape of the energy spectrum of the neutrino signal is used in the analysis and no information is assumed about the absolute number of the WIMPs annihilation. In fact, a limit on rate of annihilation is derived as a result of the analysis. A simulation package developed by Joakim Edsjö called WIMPSIM² [101] was used to generate the neutrino signal resulting from the Kaluza Klein WIMPs. The first part of the package is called WimpAnn and it simulates the production of Standard Model particles through DM annihilation in the Sun using pythia [102] and nusigma [103]. The resulting neutrinos from the standard model particles are propagated through the Sun taking into account oscillations between all three flavour neutrinos and their interactions along the way. The second part of the code, WimpEvent, propagates the neutrinos to the Earth again, taking oscillations into account and places the neutrino-ice interaction at the detector.

The following oscillation parameters of the neutrinos were used for the generation of the signal MC:

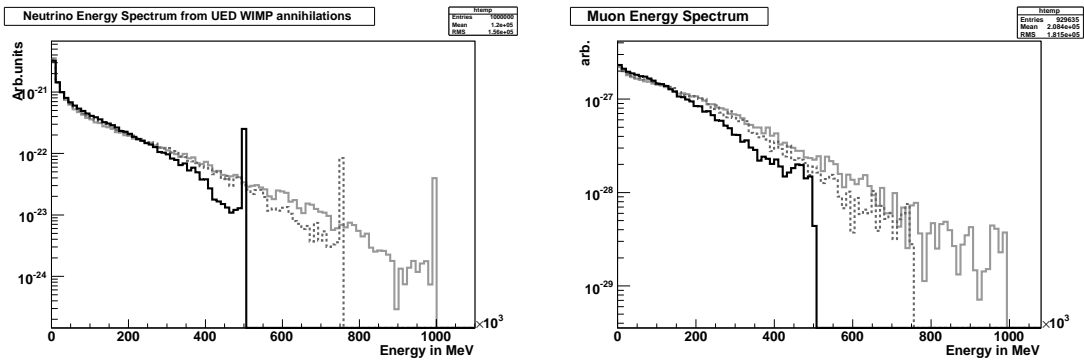
$$\theta_{12} = 33.2^\circ, \quad \theta_{13} = 0.0^\circ, \quad \theta_{23} = 45^\circ \quad (5.1)$$

as well as,

$$\Delta m_{21}^2 = 8.1 \times 10^{-5} \text{eV}^2, \quad \Delta m_{31}^2 = 2.2 \times 10^{-3} \text{eV}^2 \quad (5.2)$$

which was the default setting taken from [104]. The signal was generated during the time when the Sun was below the horizon only. As mentioned previously, an arbitrary number of the annihilation was chosen with the main emphasis placed on having enough signal number of events remaining at the end of the final level cut. For the UED B_1 WIMPs, 10 million annihilations were simulated for each year for

²WIMPSIM version 2.11.1 was used



(a) Neutrino Energy spectra from UED WIMPs annihilation (b) Muon Energy spectra from UED WIMPs annihilation

Figure 5.1: Neutrino and Muon energy spectra from the annihilation of UED WIMPs for three different WIMP masses at the detector: 500 GeV, 750 GeV and 1000 GeV.

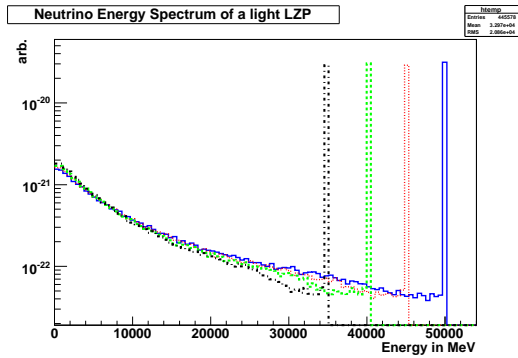
each mass at 500, 750 and 1000 GeV, according to the mass range set by the relic density consideration in section 3.3.1. The muon neutrino and resulting muon energy spectrum at the detector at the three different masses is shown in the figure 5.1.

For the analysis presented here, the Kaluza Klein channel in the WIMPSIM program was used, which gave one spectrum of neutrinos weighted with all the relevant branching ratios taken from the Table 3.1. The first column of branching ratios corresponding to $\Delta_i = 0$ was used as this was the default setting of WIMPSIM for the Kaluza Klein channel at the time. However, varying the branching ratio is quite a simple task in this framework and this was behind the motivation for the signal generation of the LZPs.

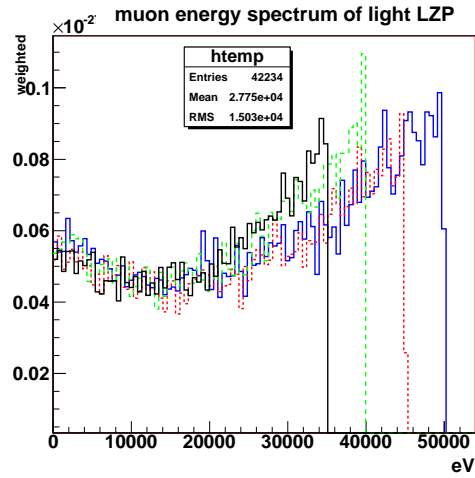
For the LZPs from the warped GUT model, we have seen that this class of WIMPs are more parameter-dependent. The signal was generated depending on the mass of the gauge boson, M_{KK} from the model (see section 3.3.3) and the annihilation channels were divided into two ranges which depends on the WIMP mass range. The two different ranges and the corresponding neutrino and muon spectra are shown in figure 5.2. The analysis on the LZPs was not taken any further in this work due to time constraints.

A routine called WimpeventF2K [105], was used for converting the events into the data format³ used for some of the AMANDA analysis chain. It executes an important step of converting the directional information of the Sun nadir angle of the initial neutrino track and the angle formed by the lepton and the hadronic shower that emerges from the interaction into the required AMANDA data format. The option to specify a threshold energy of 1GeV for the muon is chosen, as well as the muon-box volume option where the events are placed within the maximum volume(direction-dependent) that would encompass the "sensitive volume" around the detector, much increasing the simulation efficiency. The bias is corrected by attaching a volume-dependent weight to each event.

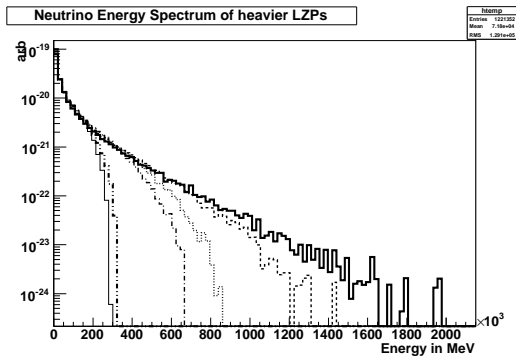
³This format is called F2k



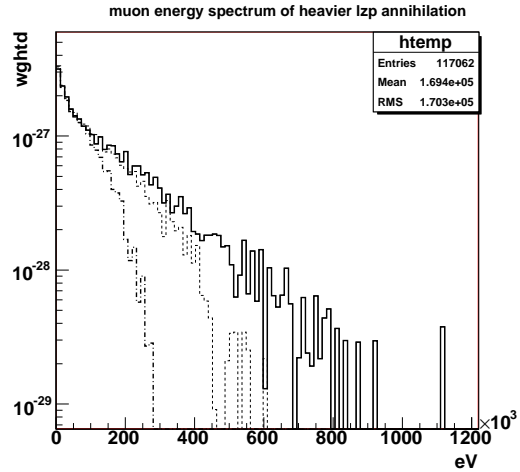
(a) The energy spectra of neutrinos from LZPs annihilation at 50 GeV (blue solid), 45 GeV (red dot), 40 GeV (green dash) and 35 GeV (black solid)



(b) The energy spectra of muons from LZPs annihilation at 50 GeV (blue solid), 45 GeV (red dot), 40 GeV (green dash) and 35 GeV (black solid)



(c) The energy spectra of neutrinos from LZP at 1500 GeV, 900 GeV, 310 GeV, 150 GeV, 90 GeV, 70 GeV, 35 GeV and 31 GeV



(d) The energy spectra of muons from 1500 GeV, 900 GeV, and 350 GeV neutrinos

Figure 5.2: Neutrino and muon energy spectra from LZPs.

The LZP signal was generated using the WimpSim [101] with a modified channel 100 (for UED KK) with the relevant branching ratios for the lighter LZPs, and for the heavier LZPs, channel 6 (annihilation to top particles) was chosen. The figures shown here are at the generation level at the detector (pre-trigger).

5.2.2 Simulation of Background

It is interesting to note that both the cosmic ray muon background and the atmospheric neutrino background for the WIMP analysis share the same origin. Although the physics of cosmic rays has been studied extensively, at the high energy end of the spectrum, the mechanism of accelerating the cosmic ray particles has yet to be identified conclusively. Almost 90 percent of cosmic rays are protons, and when they interact with the Earth's atmosphere they produce mesons such as pions and kaons. The development of a cosmic ray air shower is depicted in Figure 5.3. Neutral Pions decay into gamma photons but the charged pions would decay into a muon and a muon neutrino. The muons are called atmospheric muons because they are formed in the atmosphere and they form the dominant background in the analysis. This background can be reduced through a number of filtering steps.

The fact that the Earth is opaque to atmospheric muons, should mean that we only need to look for the up-going tracks in our analysis to remove this background. However the sheer magnitude of the atmospheric muons hitting the Earth - by a factor of 10^5 times in magnitude more than atmospheric neutrinos- means that a significant number of down-going muon tracks get misreconstructed as upgoing and these events dominate our background.

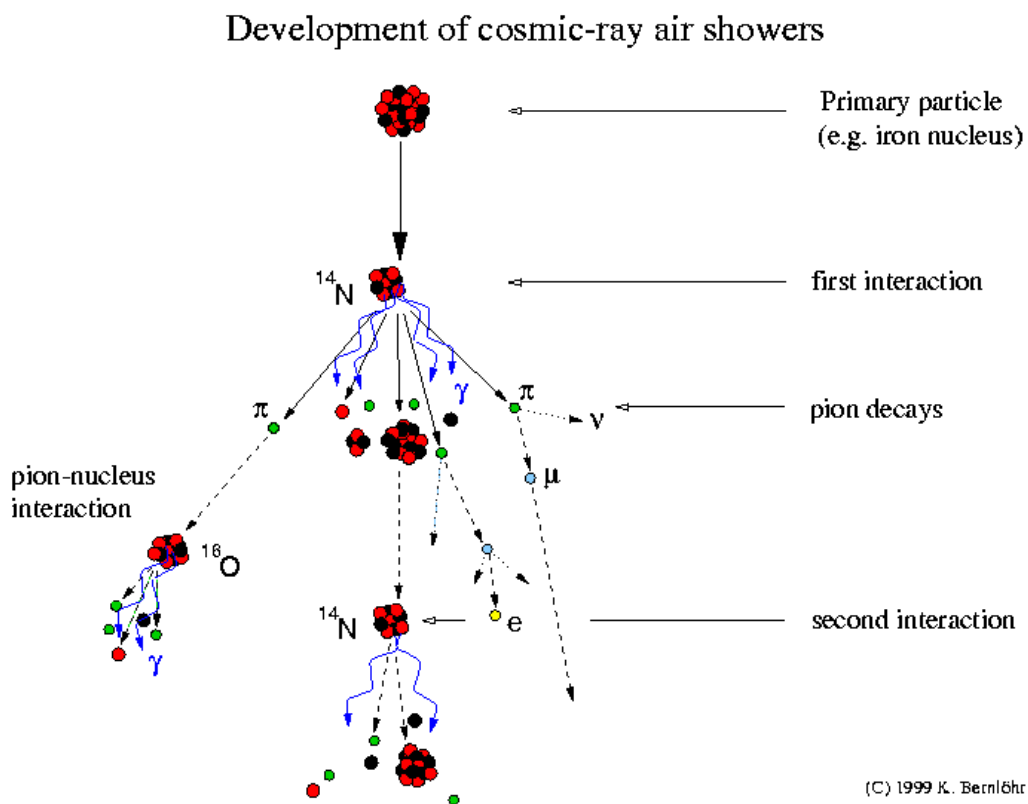


Figure 5.3: The Production of Cosmic Rays

For the generation of the reducible background of atmospheric muons, a cosmic ray air shower package called *CORSIKA*⁴ modified for use in AMANDA-II, [107], [108] was used. This consists of taking the the Wiebel-Sooth parametrization [109] composition of the cosmic rays with QGSJET model [110, 111] for the hadronic interactions. For each year, one million isotropic showers were generated, spanning the energy range of 800 GeV to 10^{11} GeV with an energy spectrum of $E^{-2.7}$. Each shower was over-sampled by 10. In total, 6000 dcorsika QGSJET files were produced corresponding to 4.6 days of lifetime.

In order to simulate the irreducible background of atmospheric neutrinos, Lipari's [112] parametrization was applied via weights in the ANIS program [113] that produces a vanilla power-law spectrum of E^{-1} . The energy range of the neutrinos generated ranged from 10 GeV to 3.25×10^5 GeV. The zenith angle was fixed from 80 to 180 degrees, as only the time when the Sun was below the horizon was relevant. Neutrino oscillations are not included. The interaction vertices are placed in an optimal volume of a cylinder with a radius 375m and length of 15 km before and 375 m after the detector centre.

5.2.3 Simulation of Propagation and Detector Response

Muons generated from both the background and signal were propagated using AMANDA software called MMC⁵. MMC propagates muons through four different media (air, firn, ice and rock). The detector response was simulated with *AMASIM*⁶. *AMASIM* calls on photon tables produced by *PTD* for propagation of the Cherenkov produced photons. *PTD* is a software package [116] that tracks photons through ice and records for the detection probability and time of the photon by an AMANDA optical module of arbitrary orientation. The results are tables of probability distributions for detecting a photons generated by a starting, stopping or infinitesimal muon track (1cm) or by a shower. Of the available ice models, MAM or the Muon Absorption Model [117] was used for this analysis. *PTD* has ice layers but each OM sees only one ice layer, meaning that multiple layers are not considered as each photon is tracked all the way to the OM.

The batch jobs submission was simplified and submitted using a perl-script based package called SIMUPERL which encompassed the simulation chain from the production of the events down to the detector response. As mentioned in section 4.1 *AMASIM* requires the year-dependent individual detector configuration, this was provided by the two separate files - geo files and elec files. The first provides the geometrical information about the OMs including the following:

- position in x,y,z in cm
- orientation up or down (1 or -1)

⁴*CORSIKA* v.6.0201 was used, [106]

⁵MMC version 1.2 was used [114]

⁶*AMASIM* version Grapefruit-Fix3 [115] was used

- projected area of the optical module in m²
- time taken for the signal to travel up the cable in ns, t_0

The elec file contains the following information:

- threshold of the channel in mV
- prompt signal from OM for 1 pe in mV which is used to determine the leading edge and the TOT
- delayed signal from OM for 1pe in mV
- noise rate of the OM in Hz
- relative sensitivity of the OM
- afterpulse probability and time
- pulse shape
- time window and number of pe
- trigger window
- SWAMP behaviour and saturation

Here pulse shape refers to the distribution of the actual voltage before the discriminator versus time. Depending on the OMs different pulse shapes can be simulated by *AMASIM*. While the typical pulse of the coax OM has a width of 600 ns, the optical OMs only have 5 ns. Time window and number of pe refer to the $\langle n \rangle$ photons arriving within $\langle t \rangle$ ns time window being joined to one hit to simulate the PMT saturation. Finally, the prompt signal and the delayed signal refer to the simulation of the two different outputs of the SWedish Amplifier(SWAMP). The first goes directly from the SWAMP to the discriminators and the second output is which is fed into peak sensing ADCs. In 2002 and 2003 the string trigger was downscaled by AMANDA-II as will be explained further in section 5.3.1. The simulation of the string trigger, however, could not be downscaled in the particular version of *AMASIM*. In order to account for the downscaling of the hardware trigger which occurred in the year 2002 and 2003, the simulated events are scaled by half when they satisfy the string trigger condition.

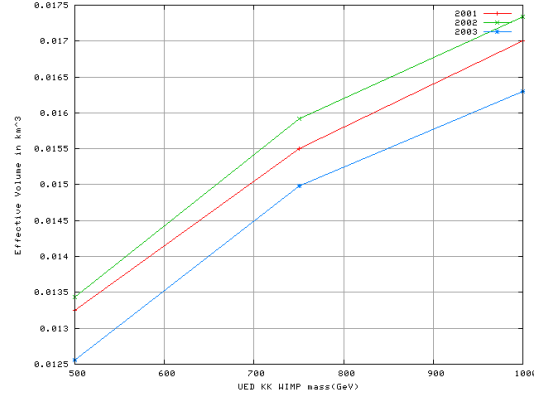
Effective Volume

In this section the concept of effective volume which is a quantity calculated at each level of analysis is introduced. It is calculated through the relationship:

$$V_{eff} = V_{gen} \cdot \frac{N_{obs}}{N_{gen}} \quad (5.3)$$

Table 5.1: Effective Volume at Trigger Level

Year	2001	2002	2003
Effective Volume m500 in km^3	$1.33e-2$	$1.34e-2$	$1.26e-2$
Effective Volume m750 in km^3	$1.55e-2$	$1.59e-2$	$1.50e-2$
Effective Volume m1000 in km^3	$1.70e-2$	$1.73e-2$	$1.63e-2$



where V_{gen} is the generation volume for the neutrino interactions, N_{gen} is the number of generated interactions and N_{obs} is the number of events detected.

The effective volume is more than just a parameter. The effective volume is used to obtain the final muon flux limit on the WIMP detection at the conclusion of the analysis. During the filtering steps of an analysis, the calculated value of effective volume can be used to check how much signal is being kept as the filtering stages are applied. It also fulfills the purpose of comparing between the detectability of the different signals. Finally the effective volume serves as a measurement of the detector performance comparison between detectors.

Effective Volume at Trigger Level

The effective volume at trigger level for each model is shown in table 5.1. These were produced with 10 million WIMP annihilations. For increased statistics, Wimpevent2F2K's oversample option was used to place the events around the detector and this increased the number of events by a factor of five.

5.3 Data

The data used for this analysis was taken with AMANDA-II during the days between 19th March 2001 and 22nd October 2003. At the South Pole, the Sun is below the horizon for six months of the year between the spring equinox and the autumnal equinox. This is illustrated in figure 5.4.

Of the data taken during this period, the time when the Sun was below the horizon, i.e. zenith angle greater than 90 degrees, was used as analysis data, and a small fraction of the portion of the data when the Sun was above the horizon (zenith angle greater than 80 degrees) was used for training purpose

Table 5.2: Data Runs Selected

Year	2001	2002	2003
Runs between	3159 – 3369	5634 – 5884	6985 – 7309
Days between	19Mar – 23Sept	15Apr – 23Sept	20Mar – 22Sept
Duration(days)	181	124.5	156.8
Livetime(days)	142.5	107.8	133.3

during the multivariate level (see section 5.5.2).

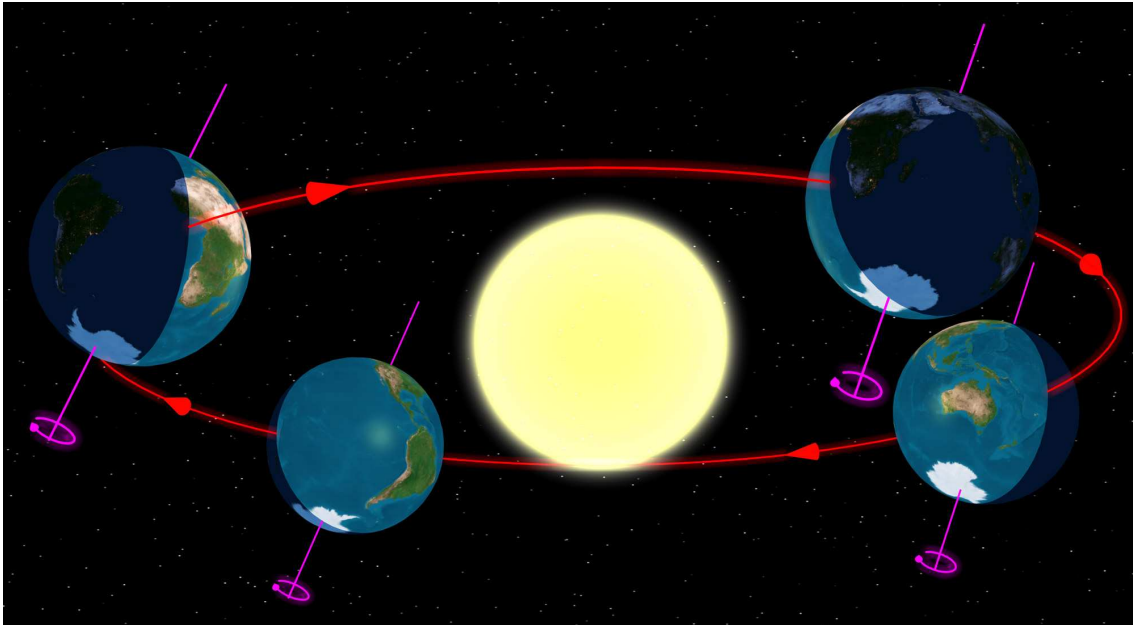


Figure 5.4: South Pole in Darkness - Between the spring and autumnal equinox is the South Pole Winter, the solar WIMP hunting season

5.3.1 Trigger Condition

As mentioned in section 4.3.4 AMANDA took data under the multiplicity trigger and string trigger conditions. Although the multiplicity trigger condition was kept uniform over the years at 24 hit optical modules during a $2.5 \mu\text{s}$ window, the string trigger condition changed over the years, sometimes within a year.

- Within the year 2001, runs up to 3270 implemented the string trigger condition where 6 out of 9 consecutive OMs on the inner 4 strings, and 7 out of 11 consecutive OMs on the outer strings had to be satisfied. From run 3270 this condition was changed to 6 out of 9 everywhere up to run number 5633 in 2002.
- In 2002, the string trigger was downscaled by a factor of two, which meant only half the events which satisfied the string trigger condition were actually recorded. However, from run 5633 in 2002, the outer strings condition changed back to 7 out of 11 OMs again. The string trigger

non-uniform configuration contributed to early 2002 data being discarded, and only data from April 2002 onwards are used where the string trigger was downscaled by a factor of two and operated in a stable mode.

- This condition carried through and was kept uniform in the year 2003. This implied that after the string trigger was simulated, for the MC signal and the simulated background, the downscaling had to be applied to the events at each level.

5.3.2 Hit Cleaning and Calibration

Before the hits can be used for reconstruction, calibration was performed on both simulated and experiment measured data according to information in section 4.3.5 and 5.2.3. However, not all detector instabilities or behaviour can be simulated. This necessitates a procedure called the hit cleaning, in which bad hits are flagged, and removed from usage in further processing steps. These include:

- **Bad OMs**
OM misbehaviour information is used to construct a bad OM list. All hits from OMs on the bad OM list are discarded. They can be defunct, or noisy or too variable in terms of the dark noise rate. The OM list is compiled each year as some OMs can operate normally if the error is fixable, for example in the case of a discovery of a badly connected module. The number of OMs used for the analysis was 513, 534 and 540 out of 677 in the three years from 2001 to 2003.
- **Crosstalk**
Crosstalk occurs as a result of the cables inducing signals in the neighbouring cables. Interference in the surface electronics boards also contribute to crosstalk. The information on the time between the leading edge and the trailing edge of a signal called the TOT, or Time-over-Threshold, is used to filter out cross talk hits which are likely to have a very short TOT. To exclude further crosstalk pulses which pass through the TOT cut, a map constructed from the time calibration identifying the OM pairs strongly susceptible to crosstalk is used.
- **Noise and afterpulses**
The radioactive decay in glass spheres of the OM can lead to noises. The dark noise rate difference in the different types of glass used for the OMs demonstrates this - the higher radioactive isotope content of the Benthos glass leads to a higher darknoise rate. These noise hits are removed by requiring the calibrated leading edge times of the individual OMs to be within a $7\mu\text{s}$ time window.
- **Amplitude**
The calibrated amplitude is required to be in between 0.1 to 1000 photo electrons.

5.4 Reconstruction

This section contains a description of the process of reconstructing the events and the filtering procedure. Several reconstruction methods were available for use with the AMANDA data. However, the description listed here will be restricted to the reconstruction algorithms used by this analysis.

The parameters of the AMANDA reconstructed events are rather simple. A muon event is simply defined by the position of the muon and its direction, at some time. The very first step in converting the individual hits to tracks is done by the First Guess methods.

The reconstruction is usually performed in a sequence of steps, as shown in 5.5.

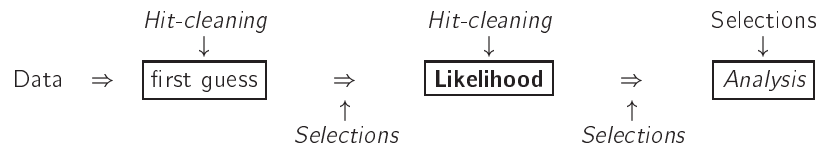


Figure 5.5: Schematic principle of the reconstruction chain

5.4.1 First Guess

Information on the timing of the hits is used by the First Guess methods in order to construct tracks. Fast analytic algorithms based on pattern recognition are used.

Direct Walk

Direct Walk is a First Guess algorithm that utilizes the hits most likely to have been caused by direct photons by selecting track elements, i.e. the line between any two hit OM's with, only with the following time difference:

$$|\Delta t| < \frac{d}{c_{vac}} + 30 \text{ ns with } d > 50\text{m}. \quad (5.4)$$

The track elements which satisfy several criteria showing compatibility with a muon track are promoted to *track candidates*. In the event when more than one track candidate is found, a cluster search is performed, where only the cluster with the largest number of track candidates is selected based on a quality criterion. Finally the average direction of all the track candidate inside the cluster defines the initial track direction, and the track vertex and the time information are taken from the central track candidate in the cluster.

Direct WIMP

A modified version of Direct Walk was proposed in [118] in order to optimize it for maximum acceptance for vertical events, while keeping the atmospheric neutrino background and rejection of the atmospheric muon background comparable. This was done by having a different condition for the cases where both hits defining the segment are in the same string - for those hits the lowering the d value from equation 5.4 and N_{hit} values, the minimum required number of hits along the track. The common data streaming with the Earth WIMP analysis meant that this was one of the shared reconstruction options.

JAMS

The first guess method that was utilized the most for this analysis was **JAMS**. JAMS stands for Just Another Muon Search, and was designed by Peter Steffen [119]. Instead of relying on looking for track elements connected by direct hits (see equation 5.4) a search for clusters is performed along different directions on an isotropic grid in the “time residual-distance to track” space. If the cluster density is high, a fit is performed to give the solution on some physical variables such as time, position and direction. Next, variables on track quality (such as the number of early/late hits, the distance of hits to the track and the spread of hits along the track) are constructed and fed to a neural net to derive a quality parameter. The cluster which has the maximum quality parameter is chosen as the solution of the JAMS.

5.4.2 Likelihood Minimization

Once the first guess methods provide the estimate of initial values, the muon track is reconstructed by following a maximum likelihood procedure. Given a set of experimentally measured values x , the unknown parameters of an event to be reconstructed, a are determined by maximizing the likelihood $\mathcal{L}(x|a)$. For the muon track, we assume that the Cherenkov radiation is generated by a single infinitely long muon track ($\beta = 1$) at $v \sim c$ that forms a cone. This is described by the following:

$$\mathbf{a} = (\mathbf{r}_0, t_0, \hat{\mathbf{p}}, E_0) \quad (5.5)$$

where \mathbf{r}_0 is an arbitrary point on the track, and at time t_0 , the muon passes \mathbf{r}_0 with an energy E_0 along a direction $\hat{\mathbf{p}}$, illustrated by 5.6.

With the likelihood defined as :

$$\mathcal{L}(x|a) = \prod_i p(x_i|a), \quad (5.6)$$

where $p(x_i|a)$ is the probability density function of observing the measured value x_i for the parameters a . For AMANDA detector, the values x consist of t_i and duration, i.e. $TO T_i$ (Time Over Threshold) of each signal and the peak amplitude A_i of the largest pulse in each PMT. However, the hit times t_i are

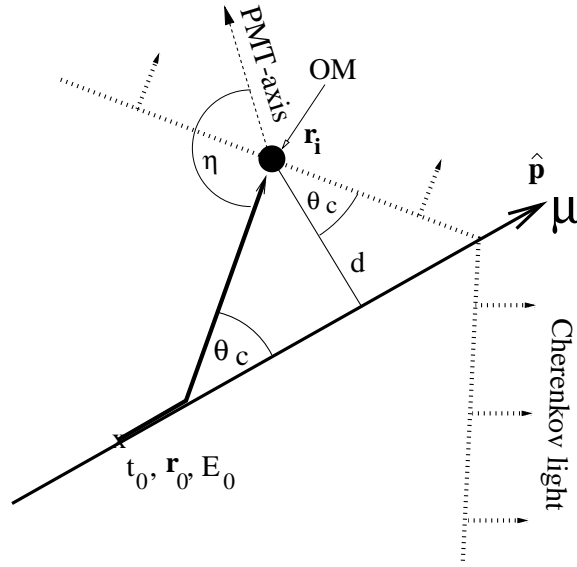


Figure 5.6: Cherenkov light front: definition of variables. A muon track defined by \mathbf{r}_0 , t_0 , and E_0

the most relevant measured information. Therefore, unless stated otherwise, the likelihood would refer to the time likelihood.

From the geometry shown in Figure 5.6,

$$t_{geo} = t_0 + \frac{\hat{\mathbf{p}} \cdot (\mathbf{r}_i - \mathbf{r}_0) + d \tan \theta_c}{c_{vac}} \quad (5.7)$$

photons are expected to arrive at OM i (at \mathbf{r}_i) at time t_{geo} .

Defining the relative arrival time, t_{res} to be

$$t_{res} \equiv t_{hit} - t_{geo}, \quad (5.8)$$

we take the difference between the observed hit time and the hit time expected for a photon that travels undelayed directly from the muon to an OM without scattering. In an ideal world, t_{res} would either be 0 or 1, and $p(t_{res}|\mathbf{a})$ would be a delta function. However due to several factors shown in 5.7, this is not the case. Effects such as PMT jitter, dark noise of the PMT as well as the photon scattering in ice and the orientation of the PMTs due to their non-uniform angular response, are all contributing factors.

The maximum of a likelihood is found via minimizing $-\log(\mathcal{L})$. This is done via minimization algorithms such as Simplex, Powell, or Minuit.

In order to prevent false likelihood maximum, or local likelihood minima that can arise due to effects such as scattering, or symmetries in the detector, an iterative reconstruction method is used.

In iterative reconstruction methods, a global minimum is reached by saving the result of the first minimization, and then randomizing the direction angles, then transforming the track point and shifting

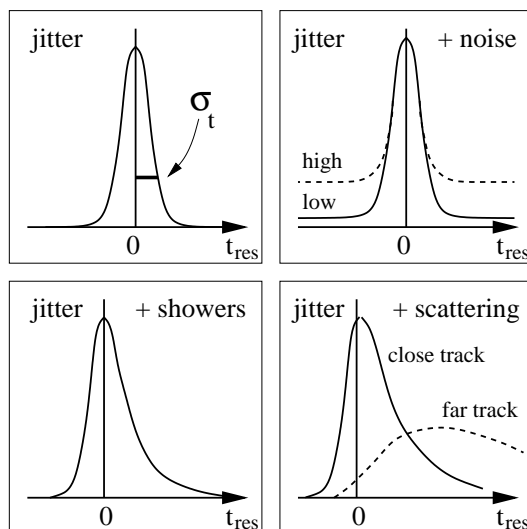


Figure 5.7: Schematic distributions of arrival times t_{res} for different cases: The effect of several factors on t_{res} are shown, the distribution is broadened and distorted. Top left: PMT jitter limits the timing resolution σ_t . Top right: the effect of jitter and random noise, can generate additional hits which are random in time. Bottom left: The effect of jitter and secondary cascades along the muon track. Bottom right: The effect of jitter and scattering, on average shifts t_{res} to later times and modifies the probability of a hit.

the time of the new point to match the expectation value, then calculating the minimization. If the new minimum is less than the previous, then it is saved instead. The fast, Simplex algorithm is used for this. In this work, a combination of both non-iterated and iterated likelihood reconstructed variables are used.

5.5 Filtering

In AMANDA reconstruction and filtering is done by the same software called Sieglinde. Calibration and hit-cleaning, and retriggering steps explained in section 5.3.2 are also performed by the same package.

5.5.1 Lower Level Filtering

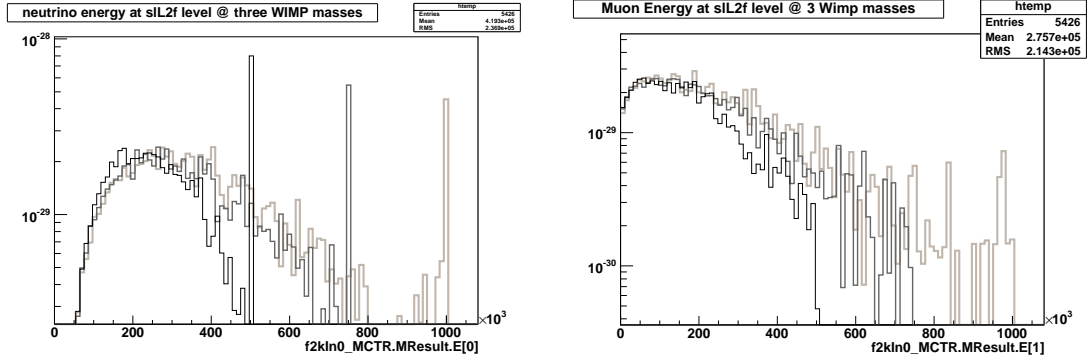
Angular cuts were performed at the lower level stages of the filtering process. The common filtering scheme for the lower levels was shared in part with Earth WIMPs analysis and Solar neutralino analysis. The lower level filtering consists of two stages.

Level 1 used two fits, DirectWalk and DirectWIMP, performed as part of a common processing by the WIMP analysis. Events passing the M24 trigger condition with a DirectWalk reconstructed zenith angle larger than 70° as well as all events with a DirectWIMP reconstructed zenith angle larger than 70° are kept. For level 1, the 'classic' version of Sieglinde was used, reading and writing the classic AMANDA f2k data format.

Level 2 performed a retriggering step, removing all events not passing the M24 or string trigger con-

Table 5.3: Flare Cuts

Flare Indicator	2001	2002	2003
long_noise_1 <	3	5	5
long_missing_2 <	3.5	3	7
only_adc_3 <	18	20	3
nch_dead_4 <	4	9	4
short_H_5 <	4	4	6.5
short_M_6 <	3	5	3.5
missing_ch_7 <	6	3	3
induc_B10_8 <	5	4	5
induc_1119_9 <	3	3	9



(a) Neutrino Energy spectrum from UED WIMPs annihilation

(b) Muon Energy spectrum from UED WIMPs annihilation

Figure 5.8: Neutrino and Muon Energy spectra at 500GeV, 750GeV, 1000GeV Wimp mass

dition. Level 1 removes hits based on bad OMs and TOT values. and the retriggering has the effect of removing slightly more data compared to the simulated background as transient OM behaviour and cross-talk phenomenon are not simulated. Several fits were performed at level 2: JAMS, 32 iterative Log Likelihood(LLH) fit and a 32 iteration Bayesian fit biased towards downward tracks. The cuts made at level 2 consisted of keeping only the events with JAMS reconstructed zenith angle larger than 70° , and events with zenith angle larger than 80° from the 32 iterated LLH on JAMS seeded events. In level 2, the 'SLART' version was used, providing the ROOT tree output used later in this analysis. Finally an additional hit-cleaning cut was performed based on removing events termed as flare [120]. Some events are designated non-photon in origin meaning that they are induced by some unknown disturbance source outside the detector. For each event, nine indicators are calculated which count the number of non-photon hits. The year-dependent flare indicator cut value is shown in table 5.3. For the meaning of the individual variables, the reader is referred to [120].

The energy spectra of the neutrino and the muon at the end of level 2 is shown in figure 5.8. The year-wise passing rate is shown in Table 5.4, Table 5.5, and Table 5.6 respectively.

Table 5.4: 2001 efficiency

source	2001		
	L0	L1(L1:L0)	L2(L2:L1)
500GeV	9.03e-27	8.05e-27(0.89)	6.67e-27(0.83)
750GeV	1.13e-26	1.01e-26(0.89)	8.40e-27(0.83)
1000GeV	1.25e-26	1.12e-26(0.90)	9.39e-27(0.83)
atm muons(scaled to livetime)	1.002e9	3.998e7 (0.0399)	2.356e6(0.05)
atm neutrinos(scaled to livetime)	4.7365e3	4.118e3 (0.869)	3.324e3(0.807)
data	1.456e9	7.6007e7(0.052)	4.278e6(0.056)

Table 5.5: 2002 efficiency

source	2002		
	L0	L1(L1:L0)	L2(L2:L1)
500GeV	9.15e-27	8.504e-27(0.93)	7.05e-27(0.82)
750GeV	1.16e-26	1.08e-26(0.93)	9.02e-27(0.83)
1000GeV	1.27e-26	1.18e-26(0.92)	9.95e-27(0.84)
atm muons(scaled to livetime)	7.066e8	2.673e7(0.0378)	1.362e6(0.05)
atm neutrinos(scaled to livetime)	3.213e3	2.921e3(0.909)	2.385e3(0.8165)
data	9.21e8	5.734e7(0.062)	2.418e6(0.042)

Table 5.6: 2003 efficiency

source	2003		
	L0	L1(L1:L0)	L2(L2:L1)
500GeV	8.55e-27	7.93e-27(0.93)	6.90e-27(0.87)
750GeV	1.09e-26	1.013e-26(0.92)	8.84e-27(0.87)
1000GeV	1.19e-26	1.11e-26(0.93)	9.71e-27(0.87)
atm muons(scaled to livetime)	8.488e8	3.135e7(0.0369)	1.639e6(0.05)
atm neutrinos(scaled to livetime)	3.5133e3	3.106e3(0.884)	2.618e3(0.843)
data	1.146e9	5.8714e7(0.0051)	3.021e6(0.05)

Table 5.7: Effective Volume at Trigger level and Level 2

Mass	Trigger Level	Level 2
m500GeV(2001)	0.0133	0.00979
m750GeV(2001)	0.0155	0.0112
m1000GeV(2001)	0.0170	0.0128
m500GeV(2002)	0.0134	0.0103
m750GeV(2002)	0.0159	0.0124
m1000GeV(2002)	0.0173	0.0136
m500GeV(2003)	0.0126	0.0101
m750GeV(2003)	0.0150	0.0122
m1000GeV(2003)	0.0163	0.0132

Effective Volume at Lower Level

At the end of lower level filtering (L2final), table 5.7 shows the effective volume in km³.

5.5.2 Higher Level Filtering

At Level 2 final level, both signal MC and background as well as data, were ready for multivariate filtering. A multivariate method is favoured over straightforward linear cuts when there is a chance of a higher correlation between the variables involved. The number of available reconstructed variables was large, but a lot of the variables, for example, those that depend on energy or the quality can share the same origin. This means that, making one cut after another might not result in optimal cuts.

Quality Parameters and Topological Fits

If the first two levels have made use of straightforward directional information, the multivariate stage placed an emphasis on utilizing the topological hit parameters with respect to a selected track. In the sieglinde package, a lot of the quality variables are described by the topology of the tracks, under the module **topf**, which takes the hits around a track within a specified radius of ρ , and provides the topological hit parameters such as the number of hits, OMs, or the number of hit strings. A more sophisticated concept like the centre of gravity(COG) of the hits can be calculated where COG refers to the centre of the detected light distribution and is the average x , y , z coordinates of the hit OMs. In the averaging the coordinates of each OM are weighted by the amount of light recorded by the OM. The **topf** module also calculates the smoothness parameter, S , which measures the consistency of the observed hit pattern with the hypothesis of constant light emission by a muon. High quality tracks with S close to zero have hits equally spaced along the track.

Other ways of deriving the quality of the tracks include taking the difference of one variables reconstructed via two different methods(or comparing the improvement by iteration) or taking the *likelihood*

parameter, or reduced log likelihood, L , or LLH, defined as:

$$L \equiv -\frac{\log(\mathcal{L})}{N_{free}}, \quad (5.9)$$

where N_{free} is defined as the degrees of freedom, and is equivalent to the reduced chi-square for a Gaussian probability. Smaller L values correspond to higher quality track reconstructions. Bayesian, or Zenith Weighted likelihood, is included as an option for iterative log likelihood. By comparing L for the best up-going versus the best down-going reconstruction, and rejecting when the up-going reconstruction is not much better than down-going this is a very efficient way of iterative reconstruction. One can use the Bayesian likelihood of

$$P(\mathbf{a}|x) = \frac{P(\mathbf{a}|x)P(\mathbf{a})}{P(x)} \quad (5.10)$$

where, as before, \mathbf{a} are the track parameters to be determined and x are the observations. Ignoring $P(x)$ which is independent of \mathbf{a} , the dependence on zenith angle of the atmospheric muons, modeled by a Monte Carlo calculations are used as a weight to the muon hypothesis \mathbf{a} , and the reconstruction performs well by maximizing the product of the p.d.f. and the $P(\mathbf{a})$, a priori.

Finally, there is a method called the Paraboloid Log Likelihood which quantifies the sharpness of the minimum found by the minimizers by fitting a paraboloid to it, and estimates the error ellipse of the log likelihood reconstructed theta/phi values.

TMVA and Neural Network

Toolkit for Multivariate Analysis, TMVA v3.9.6 [121] was used along with ROOT to perform the multivariate analysis. TMVA provides an environment for the processing and parallel evaluation of multivariate classification and regression techniques including nine different multivariate techniques and one rectangular cut.

After exploring the options of the few multivariate methods provided, the neural network was chosen taking a number of factors into consideration including its proven robustness from previous analyses, and an overall good performance. Three different Artificial Neural Network, ANN implementations are provided in TMVA. The TMlpANN, implemented in ROOT, the Clermont-Ferrand ANN (CFMlpANN), and a new ANN (MLP), which is very similar to the ROOT ANN, but can be trained significantly faster. All ANNs belong to the class of Multilayer Perceptrons (MLP), which are feed-forward networks according to the following propagation schema 5.9 Feed-Forward is a common network topology, where the connections between the units do not form cycles, as opposed to a feedback or a recurrent NN.

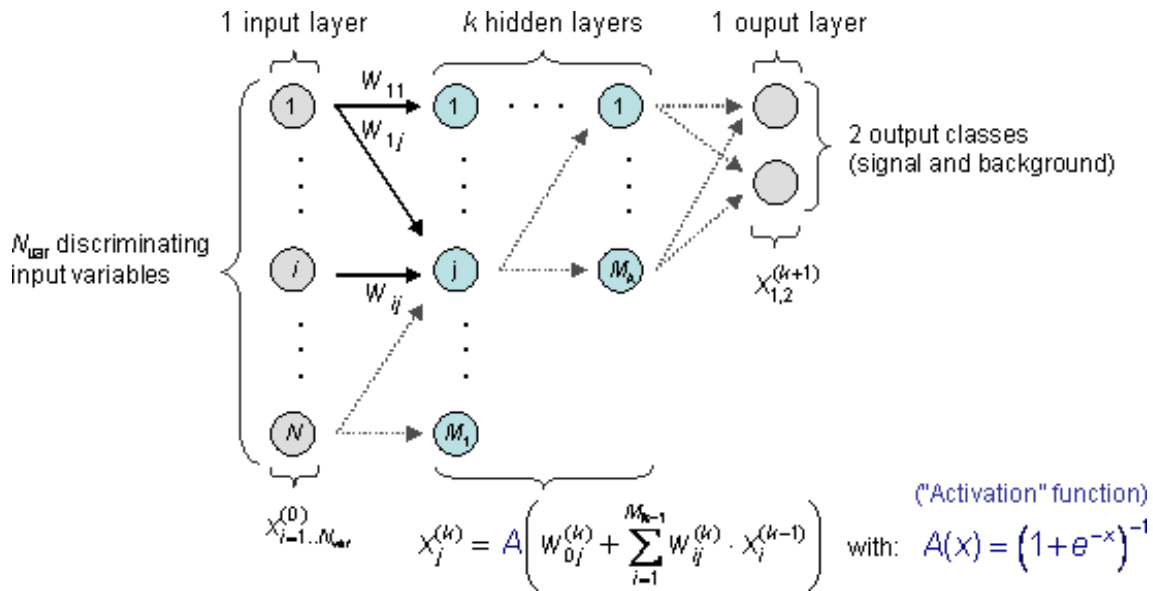


Figure 5.9: Feed Forward Network, Diagram from <http://tmva.sourceforge.net>

Level 3 strategy

Consideration was given whether to use the simulated atmospheric muons as a training sample or data taken during when the Sun is above the horizon as training sample. It was decided to use data, for in contrasts with the CORSIKA generated atmospheric muons at Level 3, the data taken when the Sun was above the horizon is much more abundant, and therefore 10,000 events were used from each year during this time against 5000 events from WIMPs sample. The comparison study yielded a similar result, meaning at this level the difference in shape distribution between the atmospheric muons and the data is not noticeable. However, using CORSIKA generated background for training the neural net would also lead to discarding the same sample. This would not be an optimal use of the simulated background. The training events were taken from the runs 3389 to 3397.

The higher level processing actually consists of two steps.

In the first step, some precuts on topological variables are performed prior to performing the neural net training, to ensure that unphysical events were removed. In the second step, a multivariate analysis is performed to identify WIMP induced neutrino events and to reject atmospheric muon background.

Precut Variables

The following variables were selected for precuts in order to remove tails in the distribution. These precuts remove mainly pathological events while keeping the vast majority of signal events. At this stage an angular cut on the reconstructed zenith angle was made removing events above the horizon.

- No.OMs > 50

Here the No.OMs refer to the number of OM's with a projected distance from the track between 5 and 100m. The OMs can be either hit or not hit in this cylinder. This cut removes tracks which do not pass properly through the detector.

- $Rhosq.dir.av < 2000m^2$

$Rhosq.dir.av$ is the mean of the projected distance squared of all OMs with direct hits within 5 to 100 m to the track. Direct hits, defined to be hits within the time window of -25 ns and 75 ns, usually occur close to the track. If they are far away on average this indicates a misreconstruction.

- $||COG_z|| < 250m$

COG_z refers to ⁷ the z-coordinate of the centre of gravity of all hits. The well-instrumented region of AMANDA extends over 500m in z-coordinates, so it removes the events which have most hits outside this region.

- $4m < COG_sigz < 50m$

COG_sigz refers to the standard deviation of $||COG_z||$

- $32Jams.Theta > 90^\circ$

$32Jams.Theta$ is the zenith angle reconstructed by 32 iteration LLH fit seeded by JAMS. This analysis is for upgoing events only.

The distributions for the each WIMP mass in 2001 at L2 are shown in figure 5.12,5.13,5.14. The blue line indicates where the precuts are made. The other years are shown in the appendix section A.1. The values chosen for the cuts are kept constant over the three masses.

In the choice of variables, some possibilities were explored in different combinations, of adding variables to an existing combination and seeing the effect on the final background rejection - see Figure 5.10, 5.11, and Table 5.8. For example, figure 5.11 shows the passing rate of the background on a sample against the passing rate of the signal. From figure 5.10, combination G(which corresponds to the combination of using the above six neural net variables plus an angular cut was chosen.

The investigation into the choice of variables revealed that this is not always intuitive. There are several factors to be considered - in terms of the separating power of the variables, the correlation of the variables to each other and also the network architecture. The relation between these factors are not so clear-cut or well understood in a multivariate method such as this one.

The figures 5.12, 5.13, 5.14 show that the tails of each distribution can be cut out with a linear cut, in order to prepare it for the neural net training.

⁷For the distribution of the value of COG_z both positive and negative see A.2.

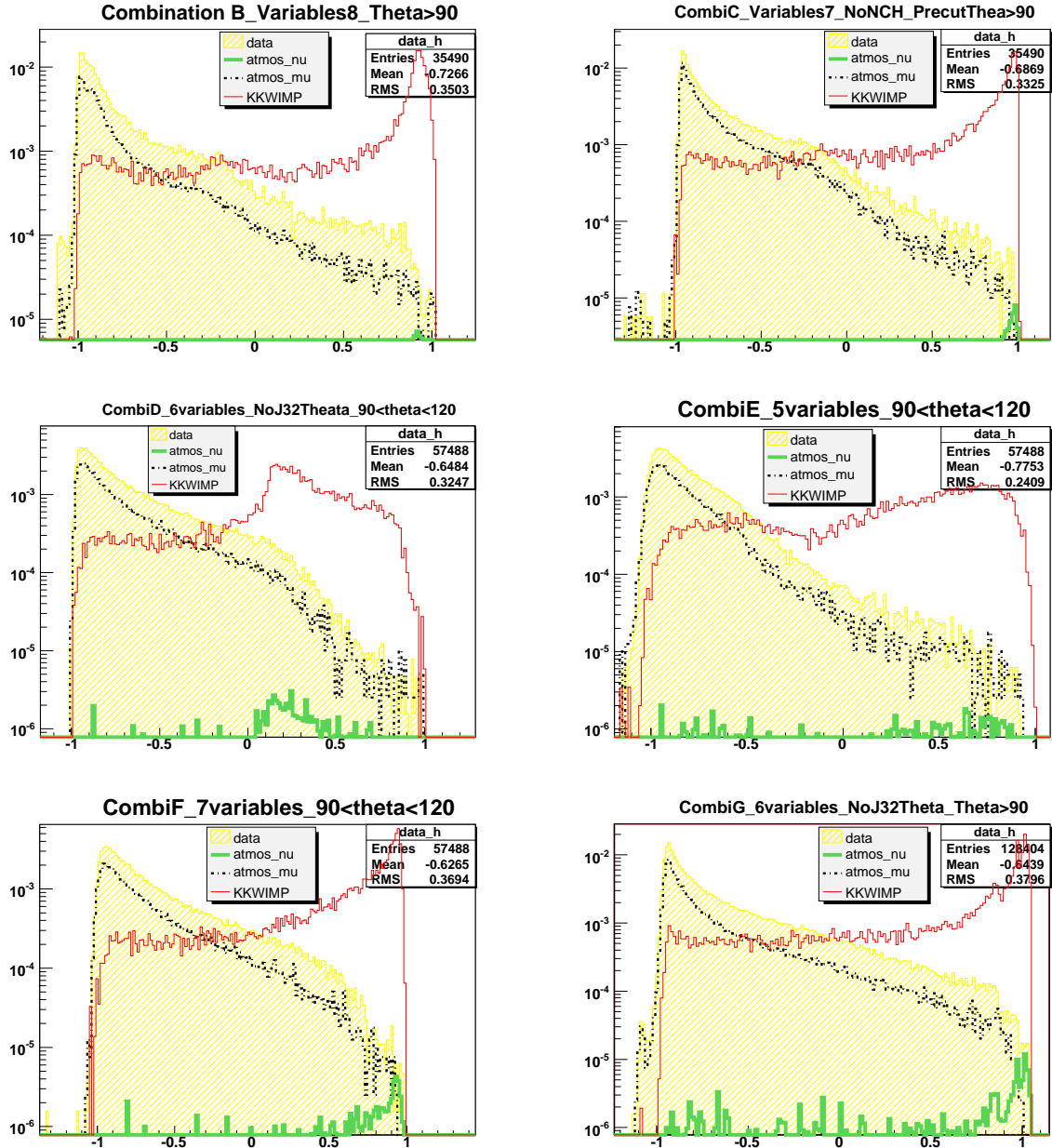


Figure 5.10: Multivariate parameter comparison of the variable combinations from B to G (left to right, top to bottom)

Table 5.8: Variable Comparison for L3 Neural Net

Variable Combination	Number of Variables	Angular Precut Applied
A	7	$\theta > 90$
B	8	$\theta > 90$
C	7	$\theta > 90$
D	6	$90 < \theta < 120$
E	5	$90 < \theta < 120$
F	7	$90 < \theta < 120$
G	6	$\theta > 90$

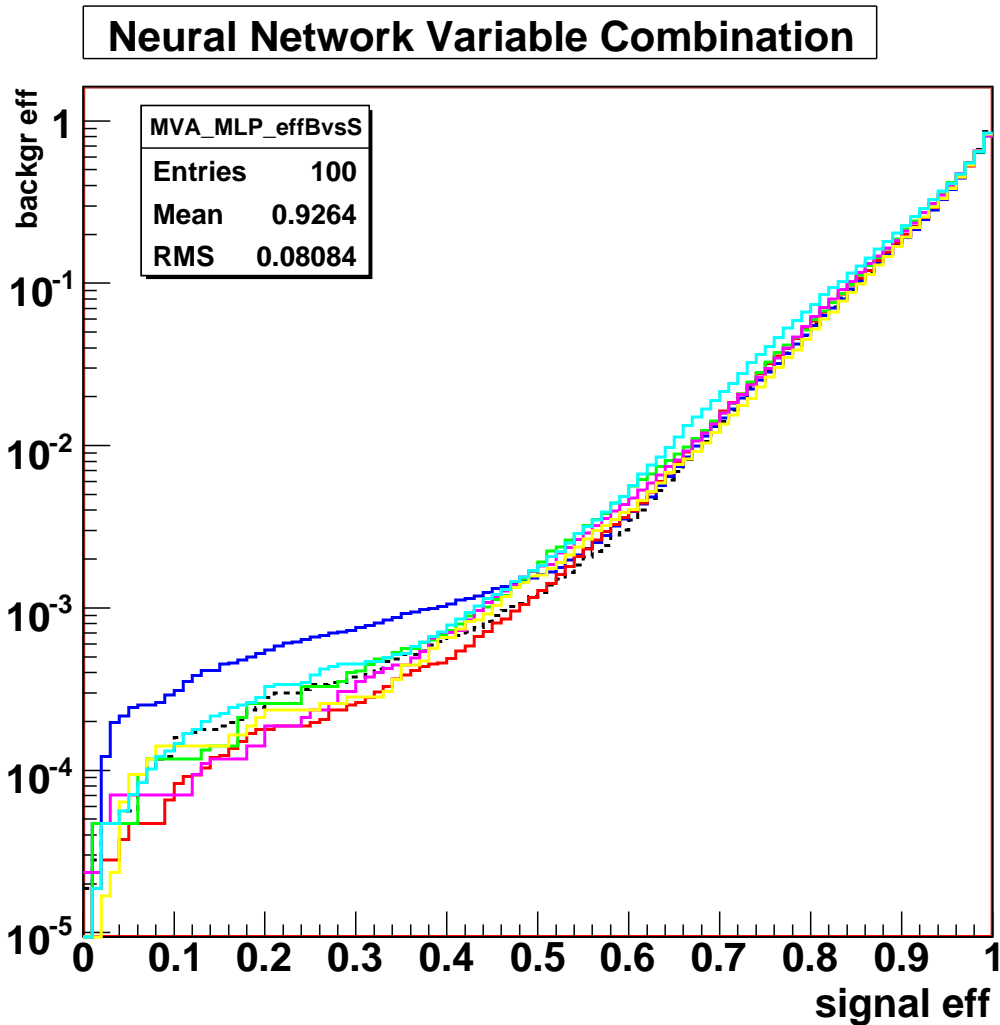


Figure 5.11: Various Combinations of neural network variables - Black A, Blue B, Red C, Green D, Purple E, Yellow F, Cyan G see 5.8 for more information.

Higher Level Variables

The following six variables were chosen for their robustness after testing their performance as neural net variables. These were chosen using the WIMP mass 750GeV signal, as they performed best among the several combination neural net variables performed with the chosen precut. The distribution is shown for the year 2001 in figures 5.15, 5.16, 5.17. For the year 2002 and 2003, the distributions are in appendix A.3.

Initially, a separate NN was trained for the WIMP masses of 500GeV and 1000GeV⁸. In this case, three different configurations would have been unblinded. Following a suggestion by the WIMP group within the IceCube collaboration⁹, it was decided to unblind only the configuration optimized for the 750GeV and derive the limits for all WIMP masses.

⁸The old method is described in detail in A.4 along with the old results obtained using this method.

⁹See the minutes of call on 9th December 2009 [122] that using one optimization would also benefit from the absence of the so called penalty factor

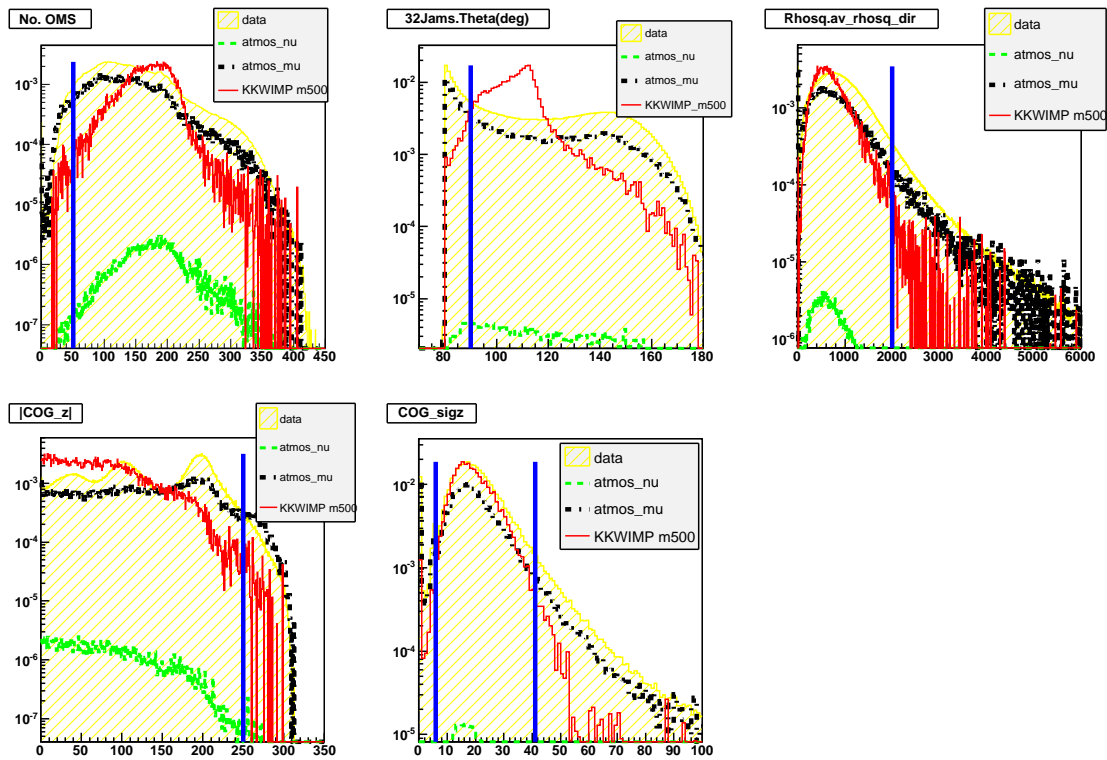


Figure 5.12: Precut L3 Variables year 2001 mass 500GeV. Blue (solid vertical) lines denotes where the linear precut is applied prior to the level 3 neural net training.

The neural net training cycle size was fixed at 600 cycles. Of the WIMP signal events, half of the signal produced was used as sample for training the neural net. The sample size used for training was 5000 signal against 5000 data events for the signal for WIMP mass 750 GeV. The signal events used for training were discarded and the MVA classifier was attached as a weight to the remaining signal events as well as to the data and to the simulated background.

Variables for the NN Training The following variables were used in the neural net classification:

- 32JAMS.LLH-32Bayes.LLH
The difference between log likelihood of 32 iterations seeded by JAMS and Bayesian reconstruction
- NDirStrC
The number of strings with direct hits of type C. Type C hits are hits recorded between the time -15ns and 75ns
- NDirB
Number of direct hits type B. Type B hits are hits recorded between the time -15ns and 25ns
- 32JAMS.Theta - JAMS.Theta
The difference in zenith angle from the JAMS seeded Log Likelihood fit and JAMS seeded 32

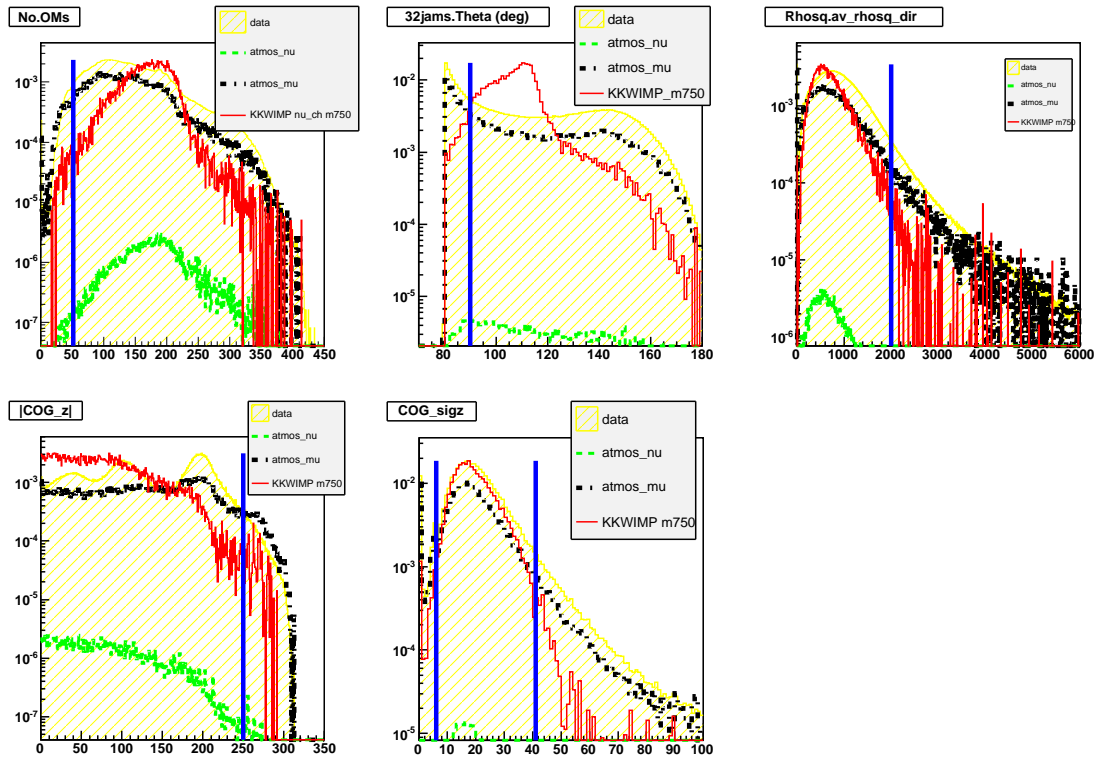


Figure 5.13: Precut L3 Variables -year 2001 mass 750GeV. Blue (solid vertical) line denotes where the linear precut is applied prior to the level 3 neural net training.

iterated Log Likelihood method.

- 32JAMS.rLLH

JAMS seeded reduced 32 iterated log likelihood fit.

- 32JAMS.LDirB

The projected length along the track of direct hits of type B.

Figure 5.18 shows the MVA classifier value for the signal and the data and the simulated background. As can be seen in figure 5.18, the atmospheric neutrino background becomes comparable to the atmospheric muon background for the MVA classifier value close to 0.95, whilst reducing data considerably and keeping a large fraction of the signal. This motivated making a cut at this value.

An additional cut at zenith angle less than 120 degrees is performed along with a MVA cut at this level for all three WIMPS.

The cut at MVA value of 0.96 results in the 2651 (scaled to three years livetime, 8(2001), 9(2001), and 6(2003)) atmospheric neutrino background events and 632 (scaled to three years livetime) atmospheric muon background events against 4509 events of data events (three years). The simulated background is simply used as a guide for the cuts to be made when the background becomes dominated by the atmospheric neutrino background, and the final level optimization is done on the remaining scrambled data.

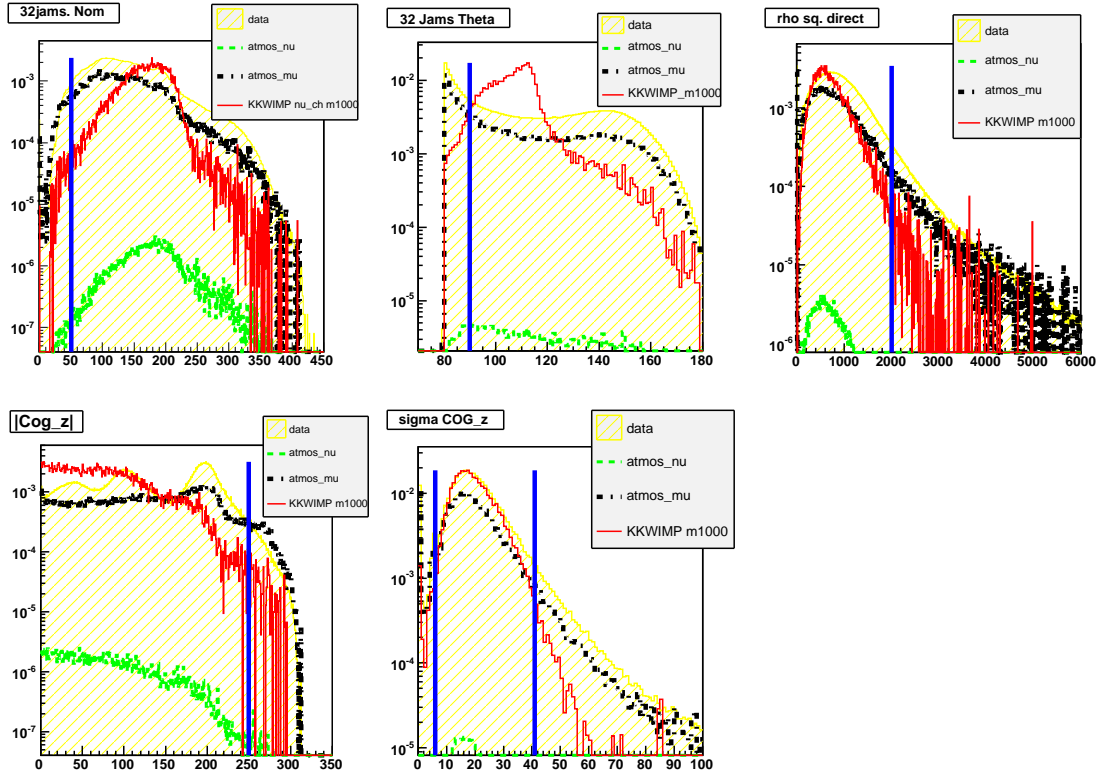


Figure 5.14: Precut L3 Variables - year 2001 mass 1000GeV. Blue (solid vertical) line denotes where the linear precut is applied prior to the level 3 neural net training.

5.6 Cut Optimization and Sensitivity

As this is a blind analysis the directional information of the Sun was kept blind during optimization of the cuts for the filtering. The Feldman-Cousins statistics [123] allows us to draw a classical upper limit from a two sided confidence intervals, from which the 90% limit result will be drawn. However, with the blindness requirement no data was available with its measured directional information until the unblinding. This meant we had to make use of the concept of sensitivity, or the average upper limit in order to optimize for our final level. It is defined as:

$$\langle \mu^{CL}(N_{bkg}) \rangle = \sum_{N_{obs}=0}^{\infty} \mu^{CL}(N_{obs}, N_{bkg}) \cdot P(N_{obs}, N_{bkg}) \quad (5.11)$$

where N_{bkg} is the expected background of events and N_{obs} is the number of observed events and finally, P is the Poissonian probability. The value derived this way replaces the Feldman Cousins upper limit prior to unblinding and is used to gauge the performance of the analysis.

In the final sensitivity optimization we used the data with randomized direction as background. We counted the number of randomized background events in the direction of the Sun as the background events remaining against a zero observation events to draw the upper average limit.

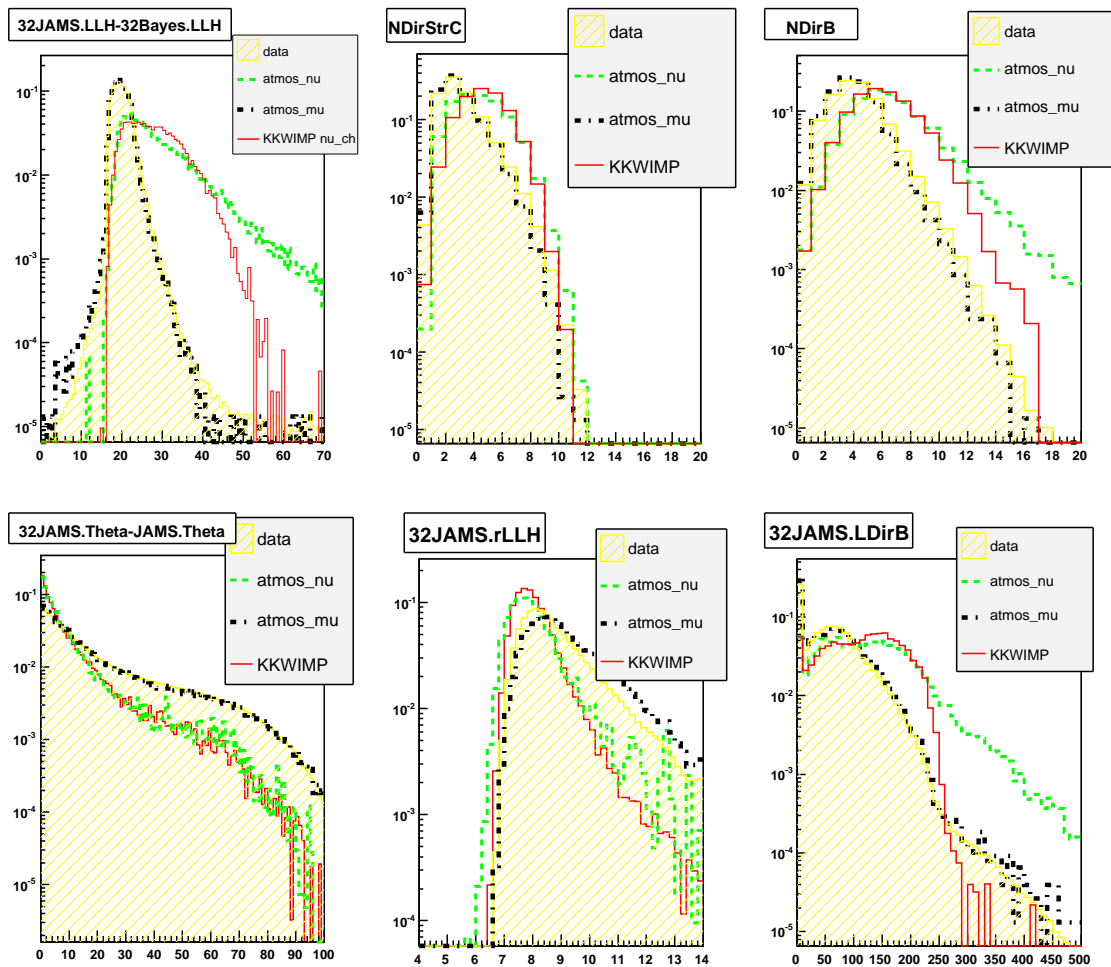


Figure 5.15: Distribution of L3 Neural Net Variables-year 2001 mass 500GeV, from top to bottom left to right, 32JAMS.LLH-32Bayes.LLH, NDirStrC, NDirB 32JAMS.Theta - JAMS.Theta, JAMS32.rLLH, JAMS32.LDirB

The final level optimization was done by using pseudo-experiments on scrambled data to determine the background. The sensitivity was determined then by translating the average event upper limit into a flux using signal MC. In more detail, the following steps were followed:

1. Iterate the following procedure for each cut of the MVA value, and each angular cone window (over a certain range):
2. Scramble the direction of the data.
 Scrambling refers to the randomization of the angular information of the data. This procedure ensures that the data is background-like.
3. Get the mean value of the background
 Count the total number of background events in a certain angle window in a large number of

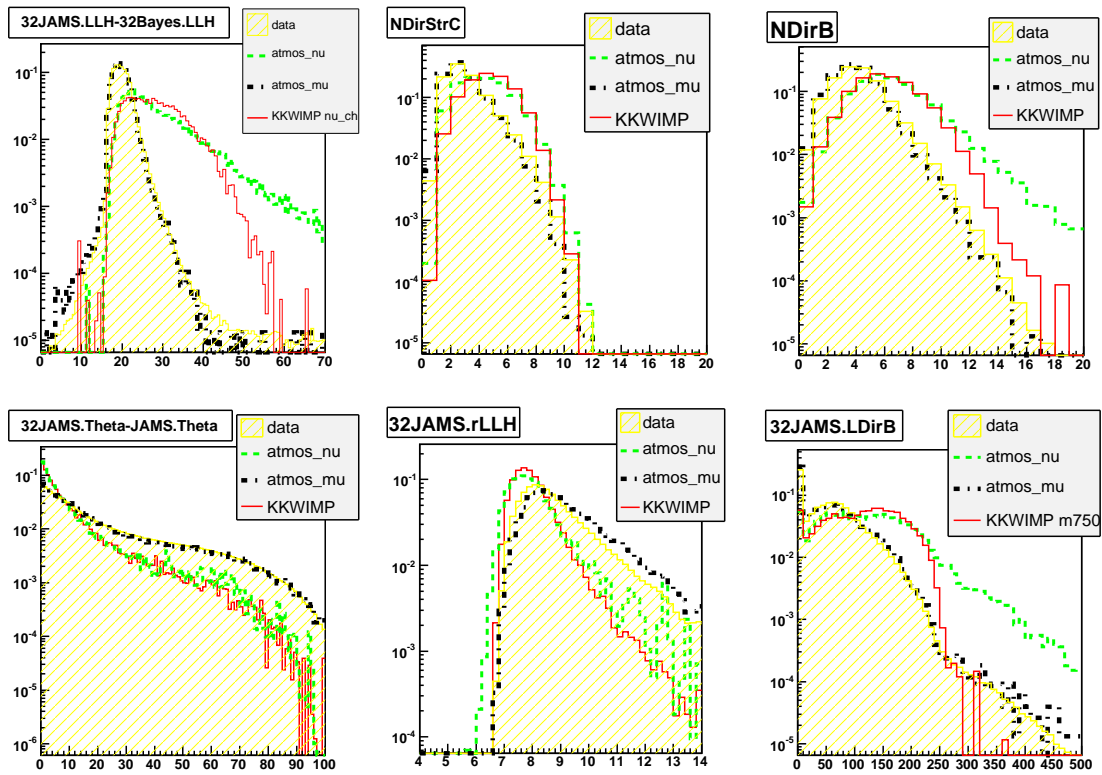


Figure 5.16: Distribution of L3 Variables year 2001 mass 750GeV, from top to bottom left to right, 32JAMS.LLH-32Bayes.LLH, NDirStrC, NDirB 32JAMS.Theta - JAMS.Theta, JAMS32.rLLH, JAMS32.LDirB

pseudo-experiments e.g. 10,000, and get the mean value.

4. Calculate the average event upper limit(90% C.L.) according to the Feldman Cousins from the value above.
5. Calculate the percentage of the signal contained in the same corresponding angular window for WIMPs.
6. Calculate the muon to neutrino rate from the above along with information on livetime and final effective volume.
7. Choose the combination of MVA value and angular cone which gives the minimum muon to neutrino rate.

The cut efficiency relative to the trigger level for each filtering level is summarized in the following plot in figure 5.20. After the multivariate filtering, the atmospheric muon background is at a comparative level to the atmospheric neutrino background which allowed us to go and perform the final sensitivity cut, looking in a angular bin in the direction of the Sun.

Figure 5.21 shows the sensitivity cuts. The plot on the left show the bins with the angular size

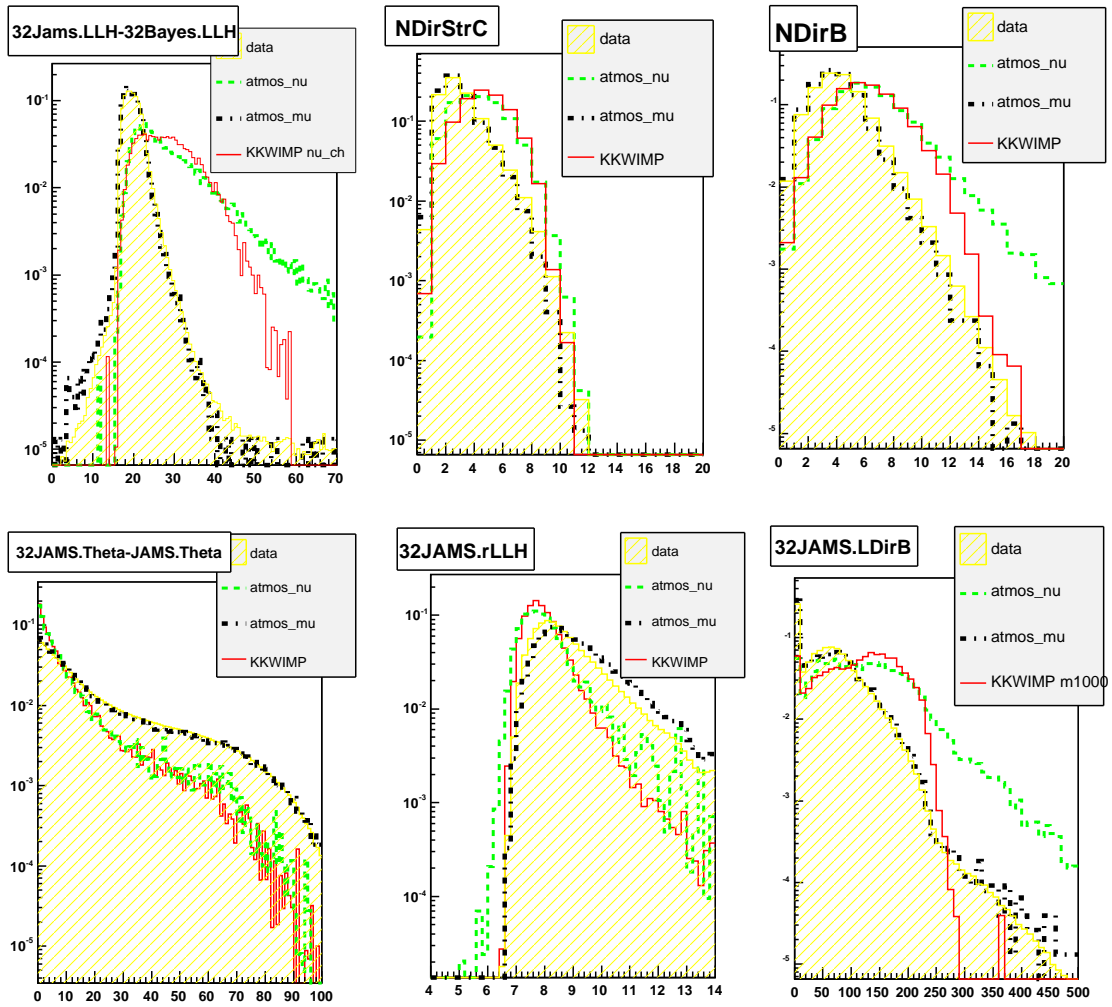


Figure 5.17: Distribution of L3 Variables year 2001 mass 1000GeV, from top to bottom left to right, 32JAMS.LLH-32Bayes.LLH, NDirStrC, NDirB 32JAMS.Theta - JAMS.Theta, JAMS32.rLLH, JAMS32.LDirB

(x-axis) and the MVA value (y-axis) and the values inside the bin show the sensitivity in terms of the neutrino to muon conversion rate. The colour scheme helps to show the contour where the minimum occurs, at which we place our final cut. The clear minimum is only shown with enough number of pseudo-experiments, as not enough statistics will not show this result. Using the result from this plot, the cut is placed at the MVA value greater than 0.96, and the angular size less than 4.5 degrees - see 5.9. The plot on the right show the corresponding number of background events counted from the randomized data. The trend of the number of background events shown in colour also supports the case and shows at a glance that we have generated enough statistics.

As stated, the concept of average upper limit, or Feldman Cousins sensitivity from equation 5.11 in which the mean of the upper limit derived from the background number only, is utilized. It is used to obtain the neutrino to muon rate below:

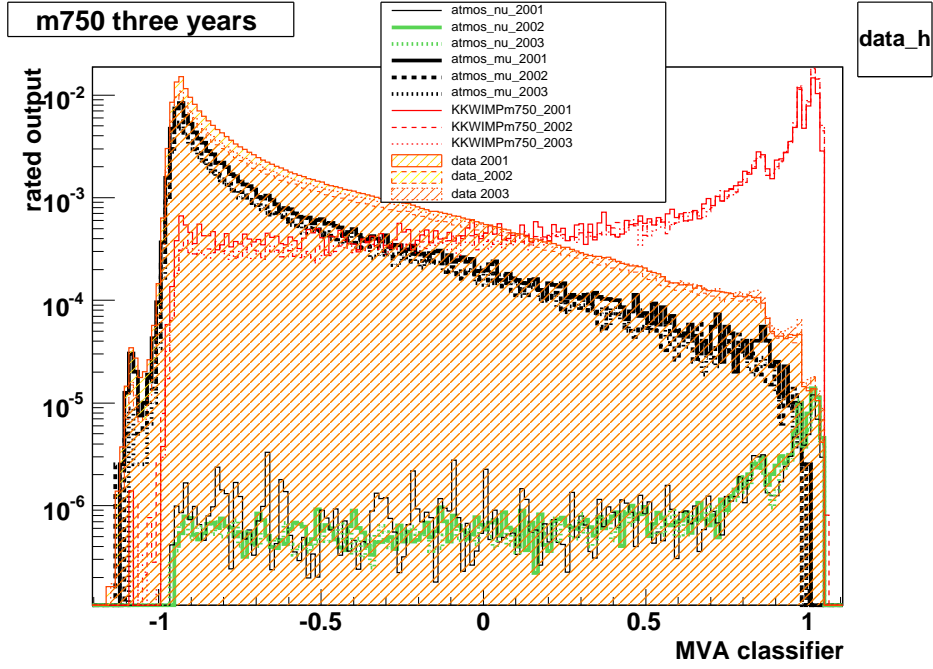


Figure 5.18: MVA Classifier output mass 750GeV, yellow(shaded) data, red(solid) WIMPs, green(dash) atm. neutrinos and black(dashdot) atm. muon on test sample

$$\Gamma_{\nu \rightarrow \mu}^{90\%} \leq \frac{\langle \mu^{90\%}(\Psi) \rangle}{V_{eff} \cdot \epsilon \Psi \cdot t} \quad (5.12)$$

where V_{eff} is the effective volume at the final level and $\epsilon \Psi$ is the fraction of signal events reconstructed within a selected source bin Ψ , and t is the detector livetime in years.

The annihilation rate of the WIMPs in the Sun is given by :

$$\Gamma_A^{90\%} = c_i^{-1} \cdot \Gamma_{\nu \rightarrow \mu}^{90\%} \quad (5.13)$$

where c_i^{-1} are conversion coefficients calculated by a script written by Edsjö [124]. We can use the calculated average upper limit on the neutrinos to muons conversion rates to calculate a corresponding upper limit on the KK dark matter annihilation in the Sun.

Finally the muon flux rate limit at the detector was derived from the following:

$$\Pi_{\mu}^{90\%} = \frac{\Gamma_A^{90\%}}{4\pi r_{\odot}^2} \cdot \int_{E_{\mu}^{thr}}^{\infty} dE_{\mu} \frac{dN}{dE_{\mu}}, \quad (5.14)$$

where r_{\odot} is the distance to the Sun, and $\frac{dN}{dE_{\mu}}$ is the differential term which represents the number of muons produced by the WIMP annihilations in the Sun.

The left figure in figure 5.21 shows where the minimum value of the muon to neutrino rate lie. The sensitivity from the average upper limit is shown in the table 5.9 calculated from the lepton/neutrino/hardronic

MLP Evolution of Error

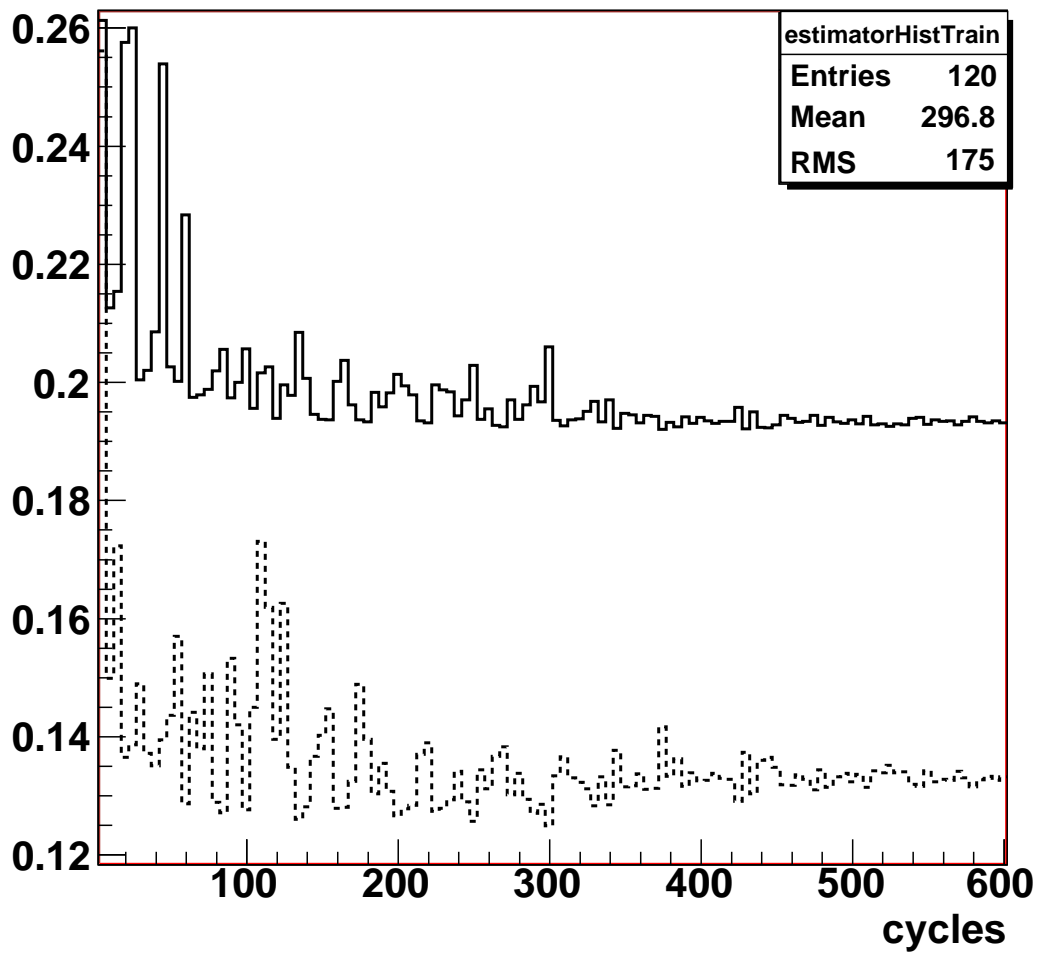


Figure 5.19: Evolution of Neural Network Errors, 600 cycles - year 2001 mass 750GeV. The dotted line is the training sample, the solid line is the test sample

shower flux conversion website [125].

Also shown are the plots of the decomposition of the effective volume at the final level in figure 5.22.

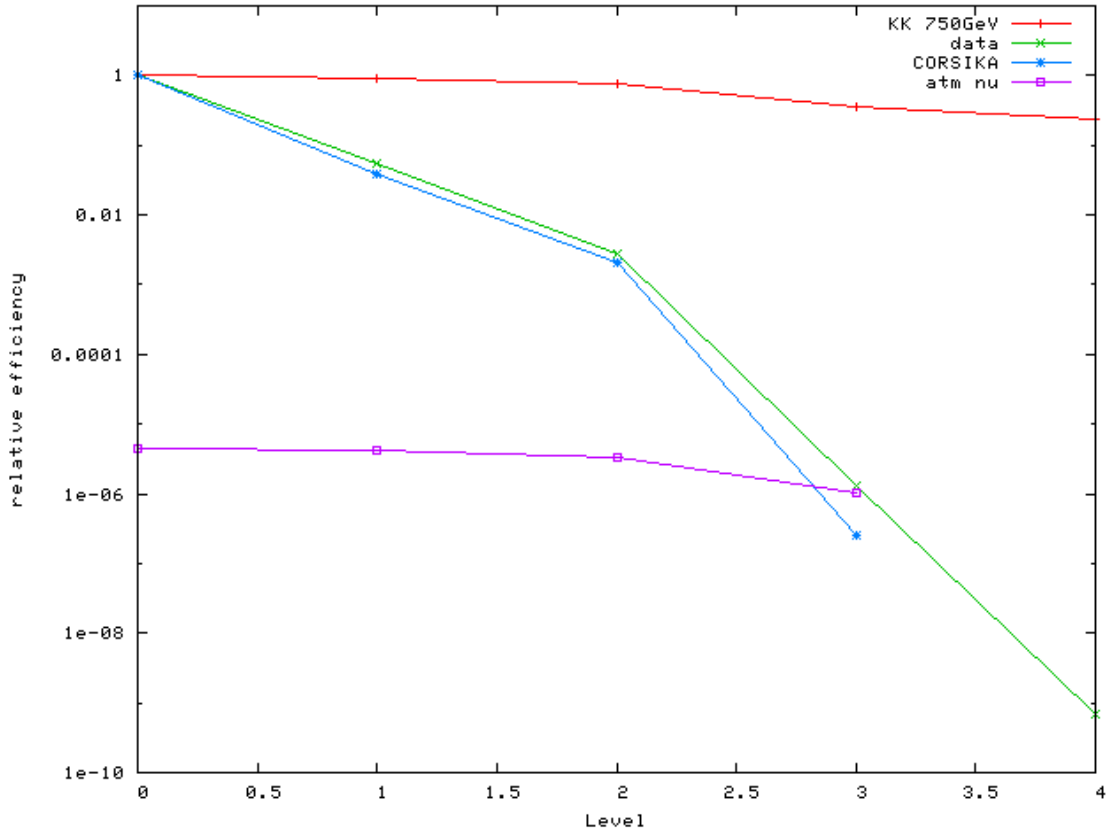


Figure 5.20: The relative cut efficiency is shown in this plot. The signal, data and atmospheric muon background are set to 1 at trigger level, and the ratio of the atmospheric neutrino background to the atmospheric muon background is plotted for the atmospheric neutrino background efficiency.

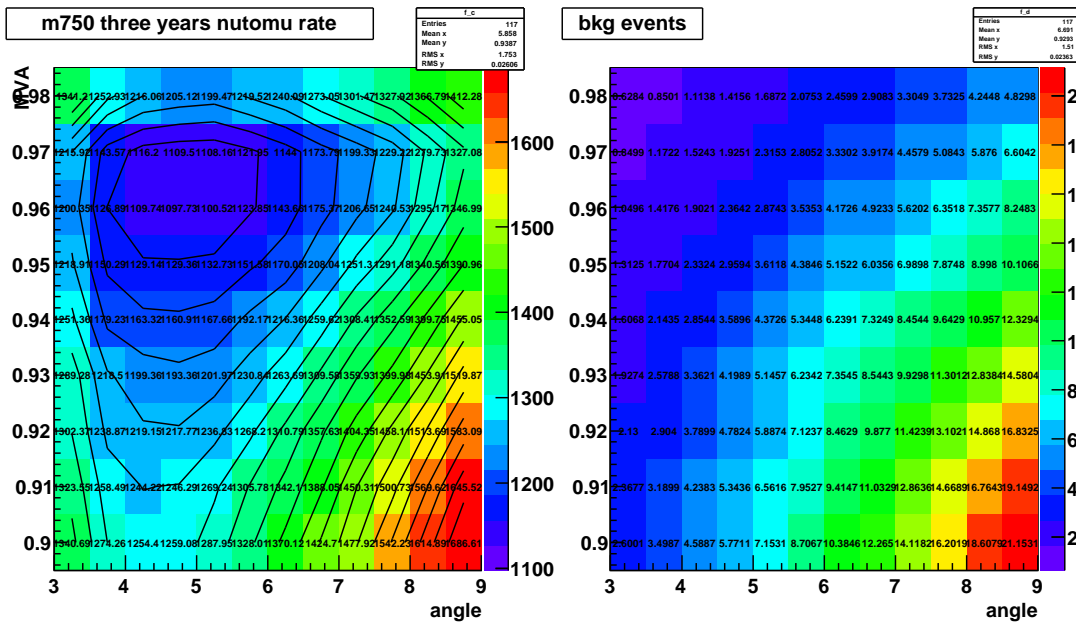


Figure 5.21: Sensitivity Optimization at the final level for the 750GeV mass LKP

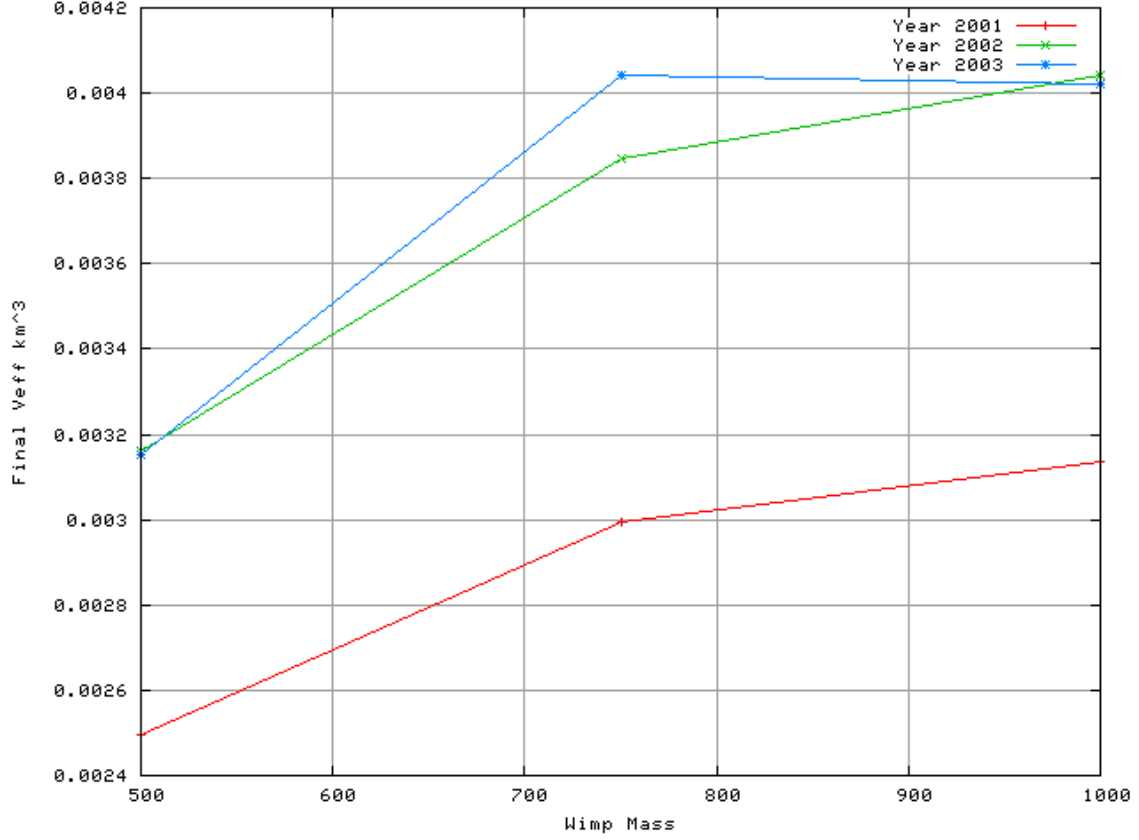


Figure 5.22: Final Effective Volume shown by year

Table 5.9: Final Cut Value and Sensitivity

Value	$m500$	$m750$	$m1000$
w_{gen}	$1.02128e - 24$	$1.0890e - 24$	$1.0956e - 24$
V_{eff} at final[km^3]	0.00294	0.00356	0.00405
MVA greater	0.96	0.96	0.96
angle less	4.5deg	4.5deg	4.5deg
bkg events	2.364	2.364	2.364
FCoverage	4.104	4.104	4.104
nutomu	$1329.3\text{km}^{-3}\text{yr}^{-1}$	$1097.7\text{km}^{-3}\text{yr}^{-1}$	$965\text{km}^{-3}\text{yr}^{-1}$
ann.rate	$2.554e21\text{s}^{-1}$	$2.049e21\text{s}^{-1}$	$1.83e21\text{s}^{-1}$
av. muon flux limit	$522.59\text{km}^{-2}\text{yr}^{-1}$	$506.64\text{km}^{-2}\text{yr}^{-1}$	$483.47\text{km}^{-2}\text{yr}^{-1}$

Chapter 6

Limits

When the unblinded data shows no statistically significant excess of neutrinos from the direction of the Sun, an upper limit is able to be placed on the flux of the muon from annihilation of WIMPs in the Sun. The limit on the spin dependent and spin-independent cross section of WIMP on proton scattering can be obtained as well. While the former provides a way of comparison with other indirect detection experiments, the latter is able to compare the limit with the direct detection experiments.

The unblinding was performed with one set of cuts for all three masses of WIMPs. This simplifies the unblinding process, as we only need to look once in the direction of the Sun with the corresponding cut values. No significant excess was observed above background. The obtained limits are presented in this chapter.

6.1 Muon Flux Limit

It is usual to express the limits obtained from an indirect solar dark matter search, with a neutrino detector, in terms of the maximum allowed resultant muon flux. As mentioned in a previous section, the model dependency of the WIMPs come into play during this stage when limits are derived.

The steps involved in obtaining the muon flux limit from the muon to neutrino conversion rate was sketched out in the previous chapter in 5.6 where the detector sensitivity was presented. The main idea is that the neutrino to muon rate obtained from the experimental result is used to convert to a WIMP-model dependent annihilation rate in the Sun, which means that Eq.5.12 is written as:

$$\Gamma_{\nu \rightarrow \mu}^{90\%} \leq \frac{\mu_s^{90\%}(\Psi)}{V_{eff} \cdot \epsilon \Psi \cdot t} \quad (6.1)$$

This result is shown in table 6.1.

Table 6.1: Muon Flux Limits

WIMP mass [GeV]	m500	m750	m1000
$\mu_{90\%}(2.364, 3)$	5.065	5.065	5.065
V_{eff} at final [km ³]	0.00294	0.00356	0.00405
$\Gamma_{\nu \rightarrow \mu}$ [km ⁻³ yr ⁻¹]	1639	1354	1189.9
Γ_A [s ⁻¹]	3.149e21	2.528e21	2.257e21
$\Phi^{90\%}$ [km ⁻² yr ⁻¹]	644	624	596
σ_{SI} [cm ²]	5.344e - 43	8.53e - 43	1.27e - 42
σ_{SD} [cm ²]	5.79e - 40	1.039e - 39	1.643e - 39

For comparison in figure 6.1 the muon flux limit is shown against the limit on neutralino WIMPs AMANDA II (hard channel) for the same years(2001 to 2003) from [15] and from a Kaluza Klein WIMP analysis from IceCube detector with 22 string configuration from [126]. In the case of the IceCube22 analysis which was done with the same configuration as a previous neutralino analysis on data during 104.3 days of livetime in 2007, a comparable limit is reached despite its larger effective volume due to a combination of factors including the longer livetime, and a higher final efficiency. This also illustrates well the point that despite the larger scale of IceCube, in terms of triggering events, the smaller spacing of the AMANDA II strings performed well for WIMP events at a relatively low energy(<TeV), and puts forth a strong case for the Deep Core project within the IceCube detector, which has just completed its deployment at the South Pole at the end of year 2009.

6.2 Cross Section Limit

The WIMP direct detection experiments search for WIMP-on-nucleon interactions. They can therefore put limits on the cross section of such interactions expressed by the WIMP mass and cross section. Amongst the direct WIMP detection efforts previously mentioned in section 3.4.1 the CDMS detector in Soudan very recently presented their final 5 year limit [127], which generated much interest. For a WIMP indirect search to compare its result with direct search it is necessary to refer to the model and obtain the corresponding spin dependent and independent cross section. This has been done in the manner described according to [128] using an approximation that either all WIMPs interact via spin-dependent scattering or via independent scattering, and that WIMP velocity follows a Maxwellian distribution:

$$\frac{f(u)}{u} = \sqrt{\frac{3}{2\pi}} \frac{n_\chi}{v_d \cdot v_\odot} \left(\exp\left(-\frac{3(u - v_\odot)^2}{2v_d^2}\right) - \exp\left(-\frac{3(u + v_\odot)^2}{2v_d^2}\right) \right), \quad (6.2)$$

where $v_\odot = 220$ km/s is the velocity of the Sun relative to the halo, $v_d = 270$ km/s is the WIMP velocity dispersion, u is the velocity of the WIMP (outside the potential well of the Sun), and n_χ is the WIMP number density. We assume that the local WIMP density is 0.3 GeV/cm³.

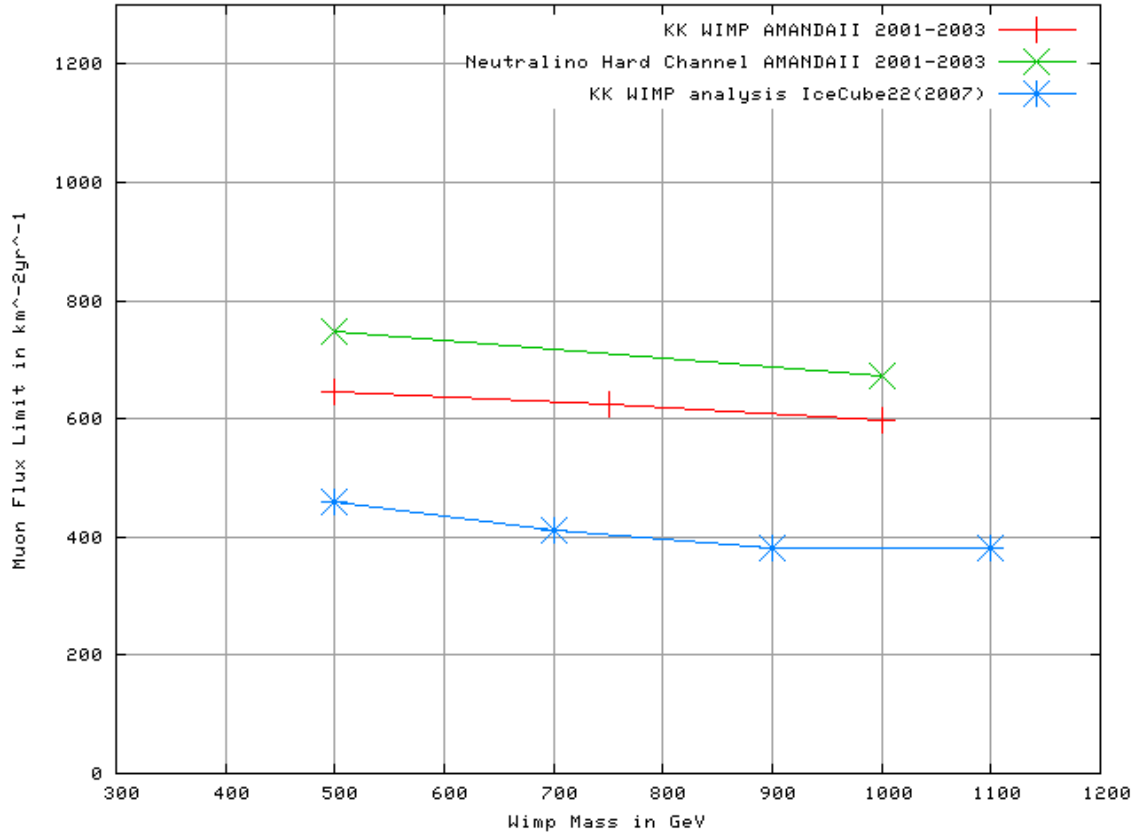


Figure 6.1: Muon Flux Limits

Muon flux limits at the detector for the KK WIMP analysis with the AMANDAI detector (2001-2003) in RED shown against two other previous analyses for comparison - Daan Hubert's Neutralino WIMP analysis [15] in GREEN, and IceCube22 analysis in 2007 from [126] in RED

WIMP capture in the Sun is dominated by the spin dependent cross section as mentioned in Section 3.3.1 therefore indirect searches such as this one are especially competitive in setting limits on the σ_{SD} . This is shown in 6.3 along with the IceCube22 limits and a selection of direct search experiments.

6.3 Uncertainties and Systematics

Uncertainties in the physics processes or approximations used in the simulation of the hardware can result in systematic errors. The AMANDA analysis of Daan Hubert [15] had a close setting for simulation at a similar energy range, so the systematics are also expected to be very similar. For a detailed description the reader is advised to refer to section 8.1.2 of [15].

In an AMANDA WIMP analysis the main systematics are due to the following:

- Neutrino-Nucleon cross-section

The quark distribution function of the nucleon $q(x, Q^2)$, is required to work out the cross-section of the neutrino-nucleon interaction. This is subject to some uncertainty. Measurement of q was

carried out by [130], and neutrino-nucleon cross-section is subject to about 5% error.

- Muon propagation

The MMC program [114] was used in propagating the muons as mentioned in section 5.2.3. Since ionization is the dominant energy loss process for the sub-TeV range muons, the effect should not contribute more than 1% to the uncertainty

- Ice Properties

The detector is in a medium of natural ice. In section 5.2.3 it was mentioned that the MAM ice model was used via *PTD*. It is extremely difficult to model natural ice realistically, and although the *PTD* linked tables are capable of a decent performance, the discrepancy becomes especially apparent when it comes to discretizing the depth-varying properties of the ice as seen in A.2. This was much improved by the Photonics package based on the work of [131]. Photonics consists of photon tracking Monte Carlo that calculates photon flux in a medium surrounding the light source and auxiliary programs used to manipulate resulting data tables. The light medium geometry and properties, and light source configuration are highly customizable. The simulation of photon from the EM cascades was investigated prior to this work by the author in [132], and the angular distribution of the photons was incorporated into the package. However, the incorporation of Photonics itself into an AMASIM analysis chain came too late for this analysis as the level 1 and level 2 filters had already been processed before the change was implemented.

The comparison/improvement with photonics was investigated carefully by [15]. The two main errors investigated consist of the implementation of the ice layers, and the underlying optical properties of the ice. The corresponding uncertainty value for the neutralino hard channel at WIMP mass 1000GeV is taken at +4% and -19%.

- OMs sensitivity

Along with the ice properties, the OM sensitivity is another major contribution to the overall uncertainty. The specific properties of the OMs such as quantum efficiency, transmissivity of the glass spheres, absolute sensitivity are measured in laboratory. However aging, as well as extreme temperature conditions in ice all contribute to modification of these values. The manufacture specification gives an expected uncertainty on total OM sensitivity of 25%, and a corresponding uncertainty was calculated to be around 10%.

The effect of the OM sensitivity is investigated separately by dividing it into a global shift [15] and individual shifts [133]. Although the global shift in OM efficiency on the effective volume is found to be around 15-20 % for the higher energy models, the effect of a 20% spread in efficiency caused by individual shifts average out to be less than 5%.

- Hardware Simulation

A discrepancy between the experimental data and the muon background trigger rate was noted during the analysis. Detector electronics simulation can partly explain this discrepancy, and an investigation of the detector thresholds simulation was performed in [134], and with retriggering, this effect can be estimated to be around 6%.

- Detector Time and Geometry Calibration

The uncertainty in the horizontal position of the OMs (estimated to be less than 0.5m) gives rise to an uncertainty of about 2.5 ns in time calibration. The effect on the analysis results have been studied in [135] by repetitive calibration of experimental and simulated data, and is found that both random and systematic errors in time and geometry calibration of the detector is less than 5%.

The limits on SD cross section including the systematic uncertainty are shown in Figure 6.4. It should be noted, however, that a substantial uncertainty from astrophysics contribute to the conversion from the neutrino-induced muon flux to the SD cross section, including the elemental abundance in the Sun, the local density of dark matter, the density distribution profile.

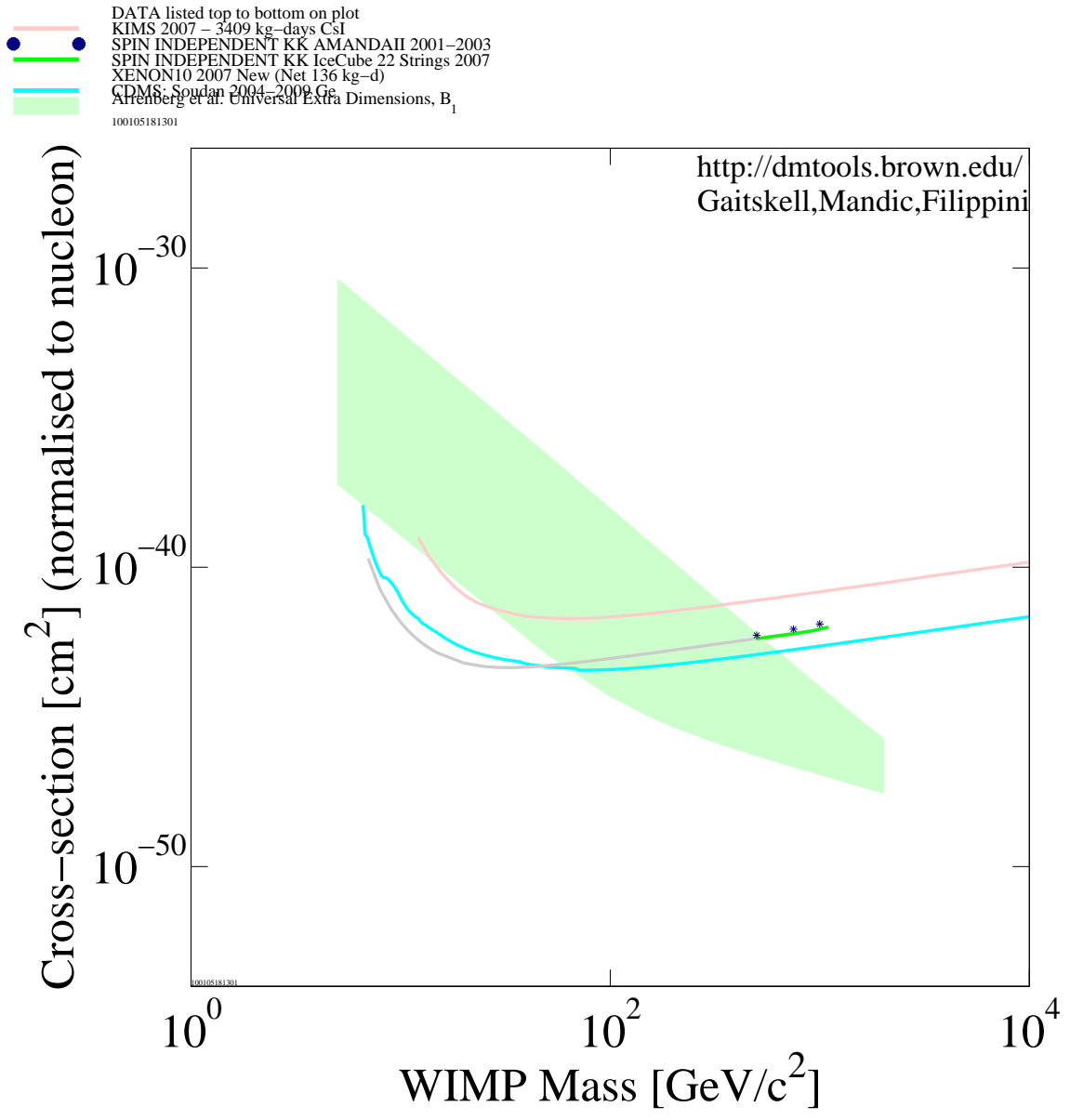


Figure 6.2: Spin Independent Cross Section Limit

SI cross section limits for the KK WIMP analysis with the AMANDAI I detector (2001-2003) in dark blue stars shown against IceCube22 analysis in 2007 in solid green from [126] against theoretically possible region (Arrenberg et. al) shaded light green. Limits a selection of direct detection searches are also given -KIMS 2007 (solid pink), XENON10 2007 (solid grey), CDMS Soudan 2004-2009 (solid cyan)

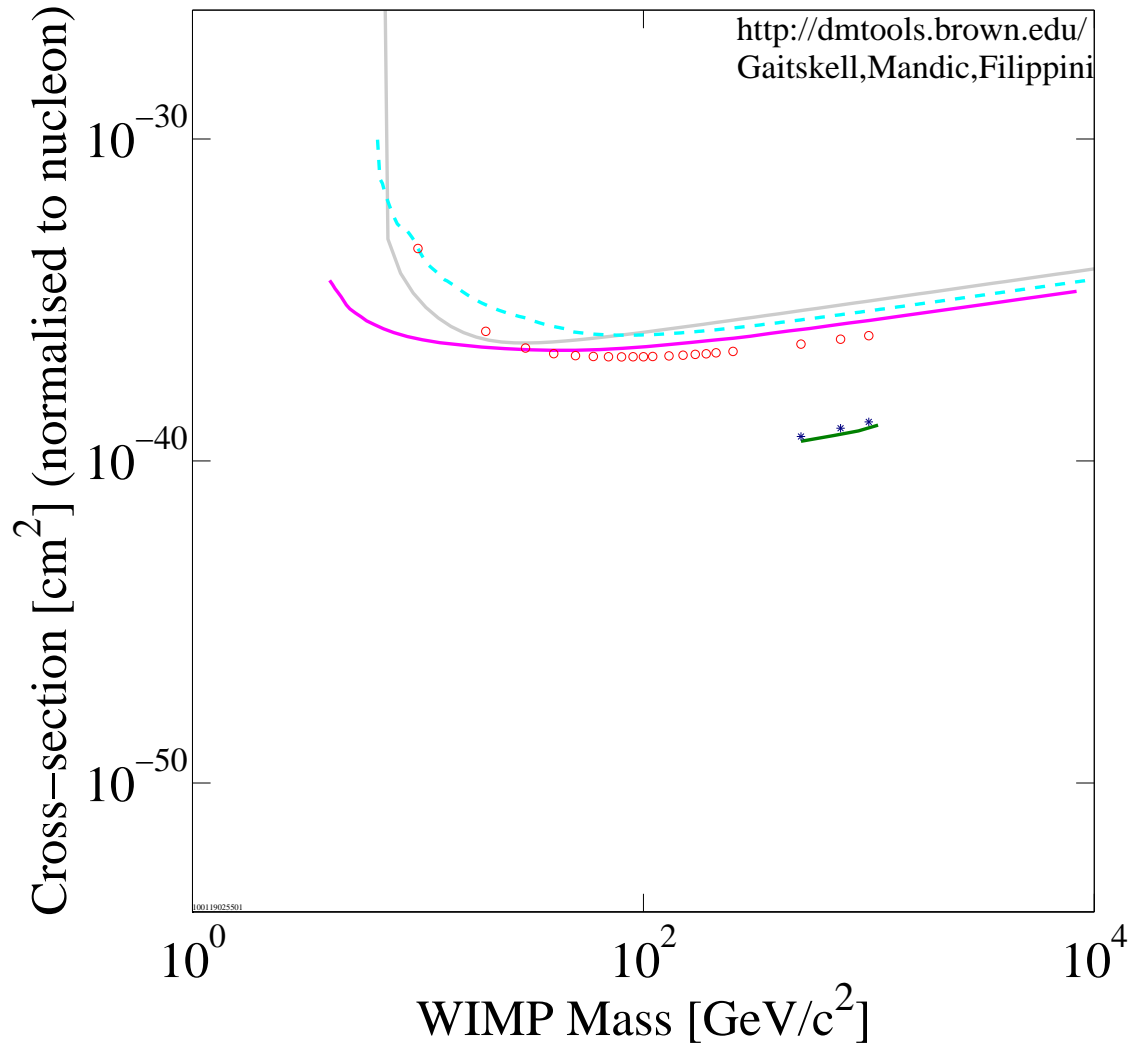


Figure 6.3: Spin Dependent Cross Section Limit

SD cross section limits for the KK WIMP analysis with the AMANDAII detector (2001-2003) in dark blue stars shown against IceCube22 analysis in 2007 in solid green from [126]. Other direct detector limits - CDMS 2004-2009(in dashed cyan), XENON10 (in solid grey), COUPP 2008 (in solid pink)are taken from the publicly available data on dmtools website [129], and KIMS 2007 limit(in red circles) is from a private correspondence

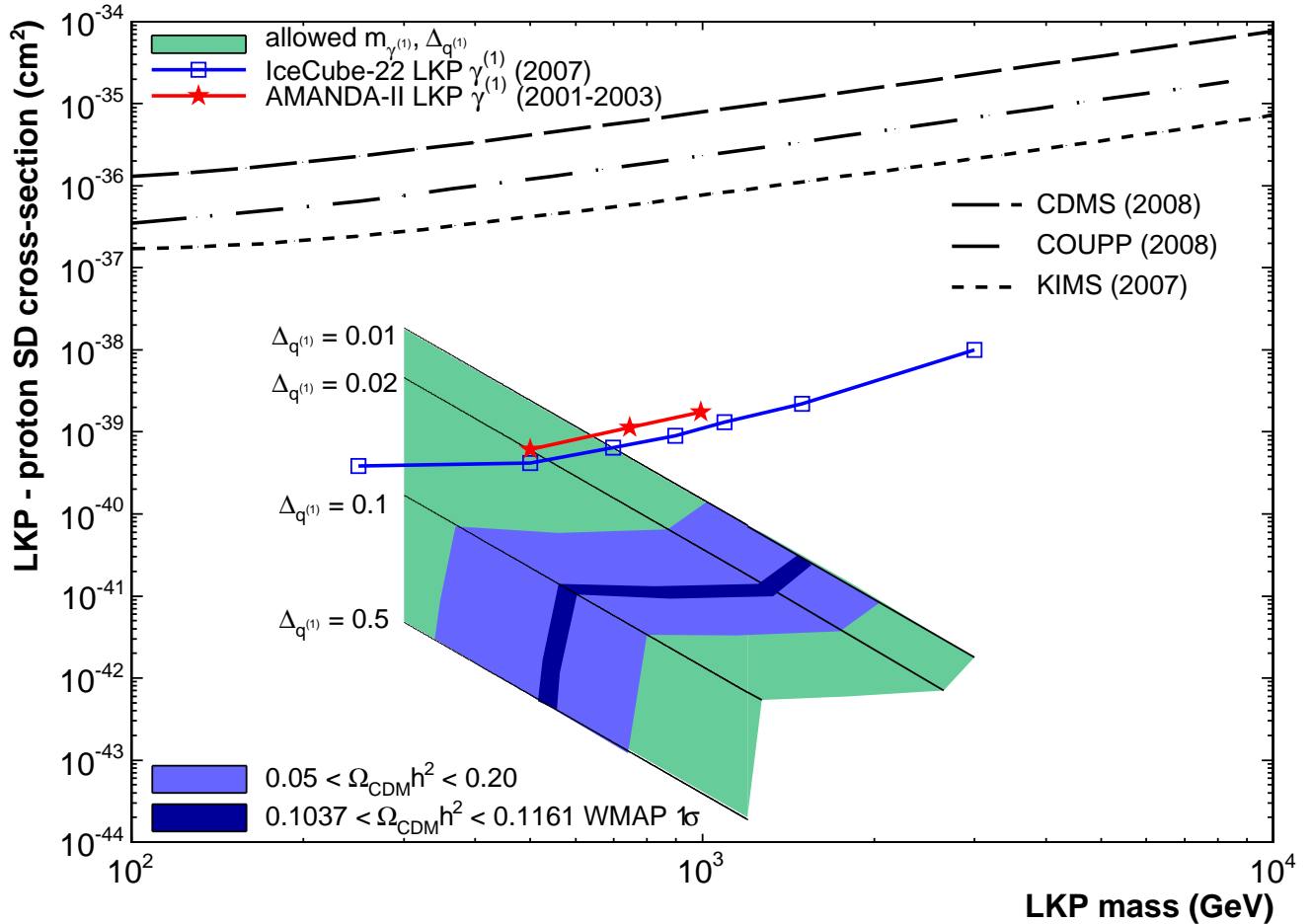


Figure 6.4: Spin Dependent Cross Section Limit with systematics

SD cross section limits (systematics included) for the KK WIMP analysis with the AMANDAII detector (2001-2003) in solid red stars shown against IceCube22 analysis in 2007 in hollow blue squares. The theoretical prediction of cross section is shown in green, and the black solid lines correspond to the mass splitting value - see section 3.3.1. The blue regions correspond to the allowed region considering $0.05 < \Omega_{CDM} h^2 < 0.20$ (light blue) and $0.1037 < \Omega_{CDM} h^2 < 0.1161$ (dark blue) from [136]. The upper bound corresponds to the overclosure limit and the lower bound at $m=300\text{GeV}$ from the collider experiment is shown from [137]

Chapter 7

Conclusion and Outlook

In this work, the AMANDA-II 2001-2003 limit on the Kaluza Klein WIMPs from the Sun was presented. This is the first completed analysis within the collaboration which was specifically optimised for a Kaluza Klein WIMP signal. Previous studies focusing on this particular model of WIMPs exist, including [138], in which only the effective volume at final level was obtained from an analysis consisting of a series of linear cuts on the 2001 AMANDA-II data, and a completed neutralino WIMPs analysis [133] on the IceCube data which was then used for obtaining the limit on the KK WIMP [126]. The result from the three years of AMANDA-II data shows a comparable limit to the IceCube with 22 strings analysis not separately optimized for the Kaluza Klein WIMPs signal. Sensitivity comparison shows a slightly better performance by the AMANDA-II KK analysis. The following conclusions can be drawn from this.

- The AMANDA-II with string trigger was well-optimized for WIMPs analysis for its detector volume. About six independent recent WIMP analyses in total have been performed. These include the five Solar WIMPs analyses [13, 15, 139–141]¹ and one Earth WIMPs analysis [14]. It is good to verify the performance of the AMANDA-II over the years in the on-going effort of the WIMPs detection before its final switch-off.
- On the other hand, the conclusion provides us with a glimpse of the feasibility of WIMP detection with the IceCube detector. At the time of writing, at the end of the 2009-2010 deployment season IceCube has 79 strings including 6 Deep core strings (see Appendix A.5. At IceCube's completion in 2011, 86 strings will be operational. This opens the door to exciting prospects of providing one of the lowest limits possible on the WIMP detection which could compliment the direct detection efforts and the collider searches. A preliminary study on the sensitivity with the 86 configuration on neutralino is shown in figure 7.1

Recently, due to various exciting results from other indirect experiments, the model building community has been very active in coming up with more variations to the models. Previously the emphasis

¹There is one more in preparation [142]

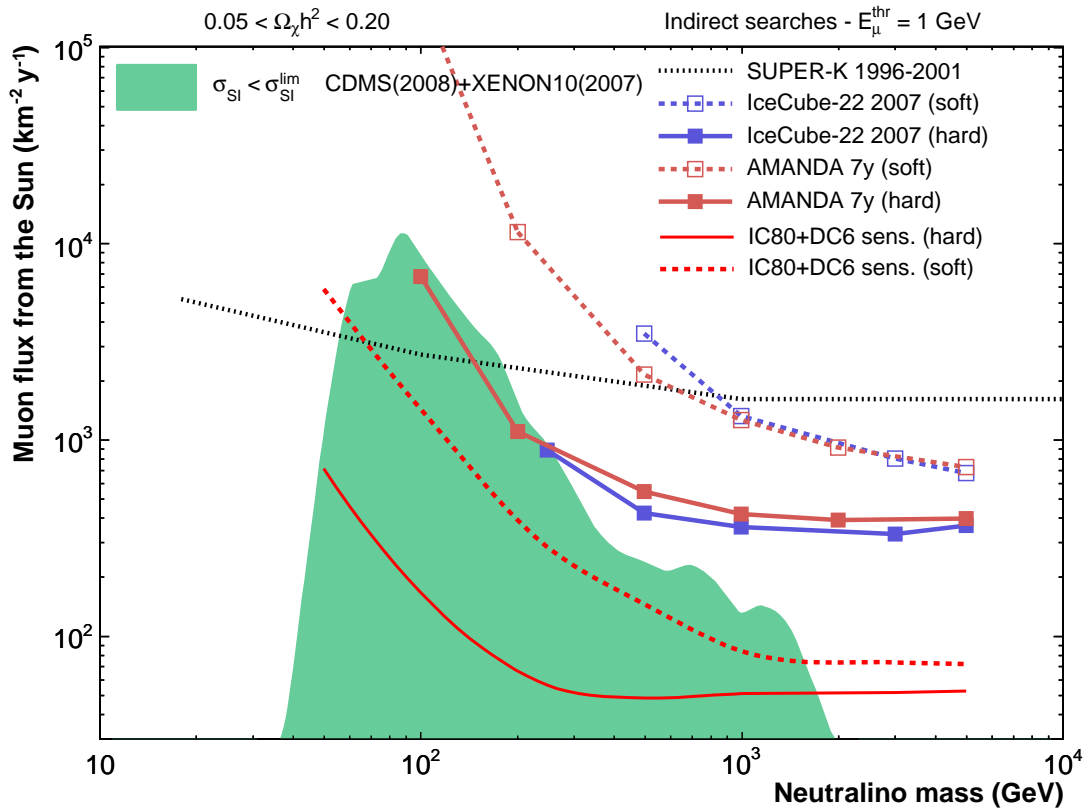


Figure 7.1: Sensitivity of IceCube with 86 Strings Solar Neutralino

The extent to which IceCube at full capacity can lower the solar neutralino sensitivity is shown primarily against other previous IceCube Neutralino Analyses limits : IceCube-22 refers to the result from [133], and AMANDA 7y refers to the result from [13]. Figure provided by IceCube repository

has been on neutralino WIMPs as the main dark matter candidate. However now there is a new effort by the theorists not only to come up with other models, or *tuned* models, but also look at scenarios with varying parameters within the model. Some aspects of the models with extra dimensions have been sketched out in chapter 2, but a lot of the more recent developments and predictions with respect to collider technology were not discussed. As WIMP signal generation program such as WIMPSIM [101] have become more developed and are capable of customizing to various parameter changes (such as the annihilation branching ratios to each of the SM particles) it is feasible to expand the analysis to try out the many different scenarios. This can include both variation within the UED model (i.e.with different mass splitting fraction) and as tried in this work, to other similar models (e.g. sUED and Warped GUT).

It is also worth mentioning that there have been preliminary investigations into looking for WIMPs from the galactic halo as well [143]. Depending on the halo models applied, this method looks for the WIMPs annihilating in the galactic halo to place limits on the annihilation cross section, and is different from the Solar or the Earth WIMPs analysis in that it is not looking for an excess of events from a source but is looking for anisotropy in the signal. It is based on an interesting idea of looking for WIMPs from the *least visible annihilation product* suggested by [144], and is expected to be capable of putting a

very stringent bound on a relatively model-independent annihilation cross section bound on the WIMPs, especially with the Deep Core part of the IceCube.

In terms of the models with extra dimensions, several works have looked at the feasibility of looking for various signatures beyond the DM search with the AMANDA/IceCube detector.

In [145], the neutrino-nucleon cross-section increase with energy surpasses the increase predicted by the Standard Model. For three different extra-dimension cases this is shown in 7.2. This would result in the increase in the flux of neutrinos to be more pronounced in the down-going direction, which could in turn be investigated by looking at the zenith angle dependency of the flux. A preliminary investigation was performed using the IceCube 2007 data in [99] to look at a model-independent limit. It was found that any model which increases the neutrino-nucleon cross-section by more than two orders of magnitude is unlikely at the center-of-mass energy of the cosmic neutrino collision above 40TeV. These collisions are due to cosmic neutrinos with typical energy above 1EeV.

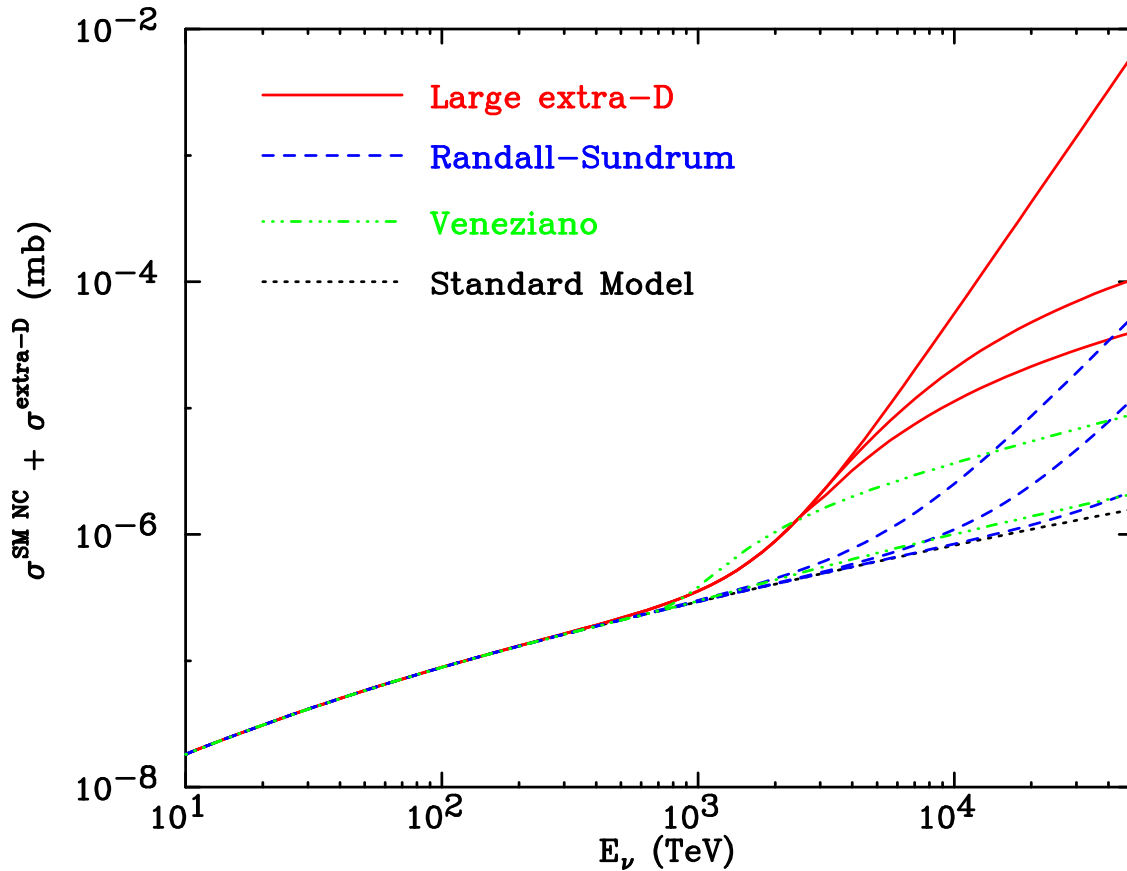


Figure 7.2: Neutrino-nucleon cross sections in a variety of extra dimension models compared to the Standard Model neutral current prediction. ADD (large extra dimension) models are for all, 5 and 1 partial waves, up to unitarity saturation (top to bottom). RS models are shown for $\Lambda=1$ TeV, $m_g=500$ GeV; $\Lambda=1$ TeV, $m_g=1$ TeV; $\Lambda=3$ TeV, $m_g=500$ GeV (top to bottom). Models using Veneziano amplitudes are for $a = b = 5$ and $a = b = 0$ (top to bottom). $M_s=1$ TeV for all models. Figure from [145]

Another manifestation of such models would be the production of micro-black holes from UHE cosmic rays which then could decay into standard model particles. Such black holes would then evaporate and the resulting hadronic showers, muons and taus could be detected by neutrino detectors such as IceCube. The feasibility has been calculated by [146], and there are future plans for IceCube analysis [99].

All in all, the future is looking exciting for probing theories with extra dimensions with IceCube, whose path was well paved by AMANDA, RIP.

Appendix A

APPENDIX

Appendix A: Precut Variable Distribution for years 2002 and 2003

In this appendix the the precut variable distributions are shown for 2002 and 2003. The precut variables are described in the Precut Variables section in Section 5.5.2.

Year 2002

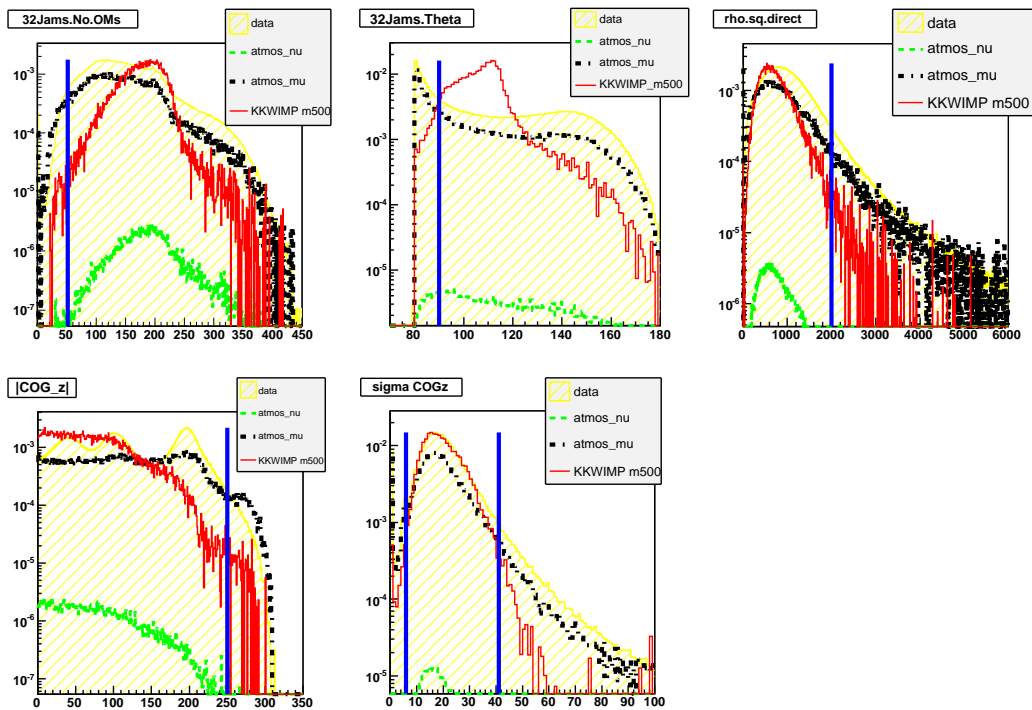


Figure A.1: The precut L3 variable distributions for the 2002 data with a 500 GeV WIMP mass as the signal. Blue (solid vertical) lines denotes where the linear precut is applied prior to the level 3 neural net training.

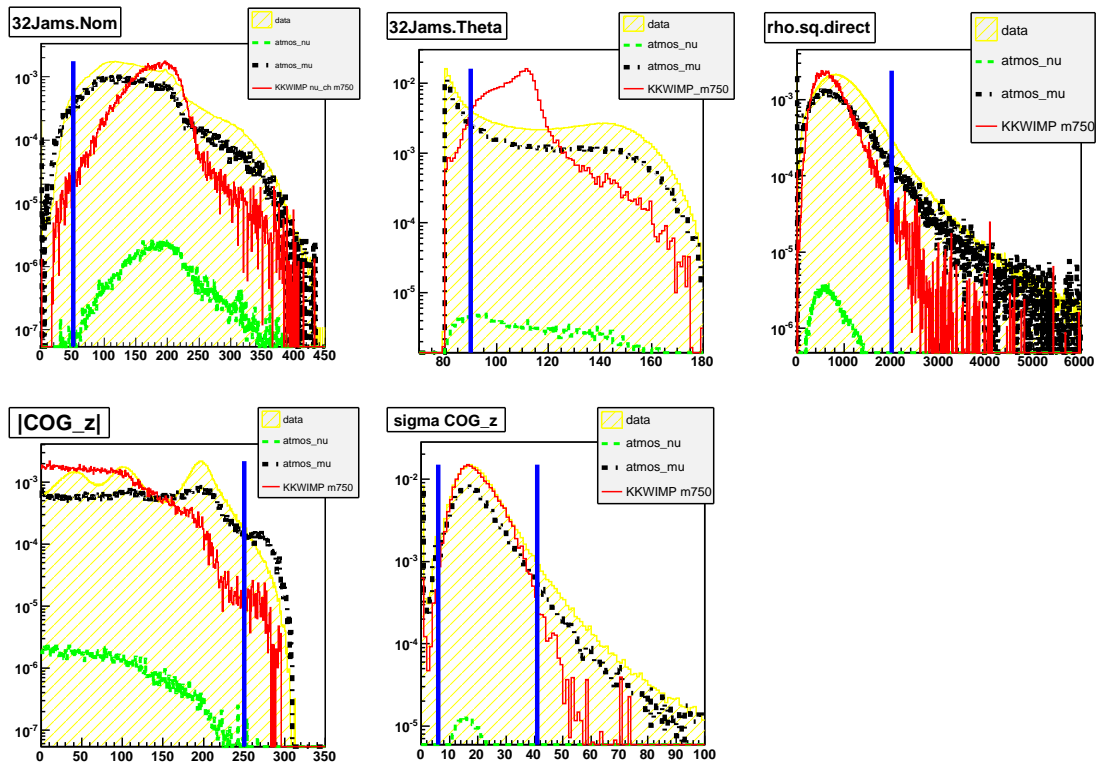


Figure A.2: The precut L3 variable distributions for the 2002 data with a 750 GeV WIMP mass as the signal. Blue (solid vertical) lines denotes where the linear precut is applied prior to the level 3 neural net training.

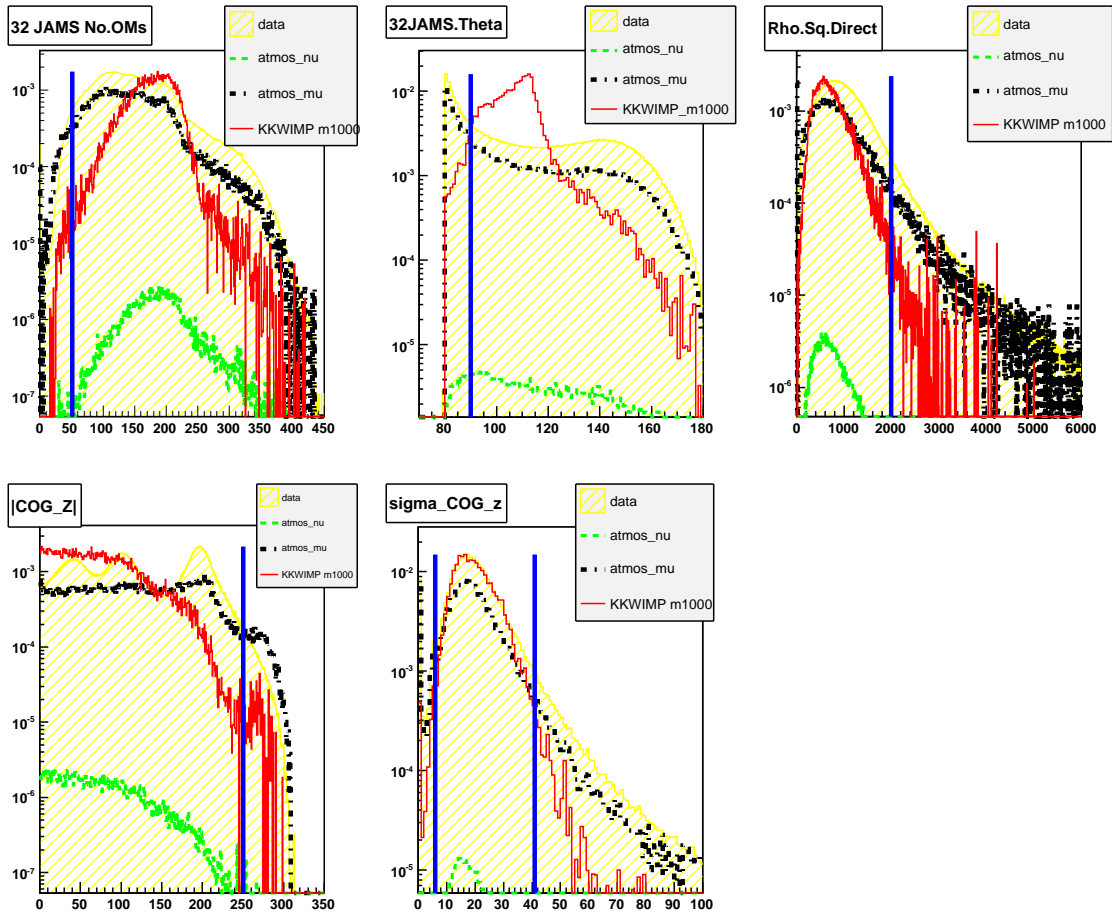


Figure A.3: The precut L3 variable distributions for the 2002 data with a 1000 GeV WIMP mass as the signal. Blue (solid vertical) lines denote where the linear precut is applied prior to the level 3 neural net training.

Year 2003

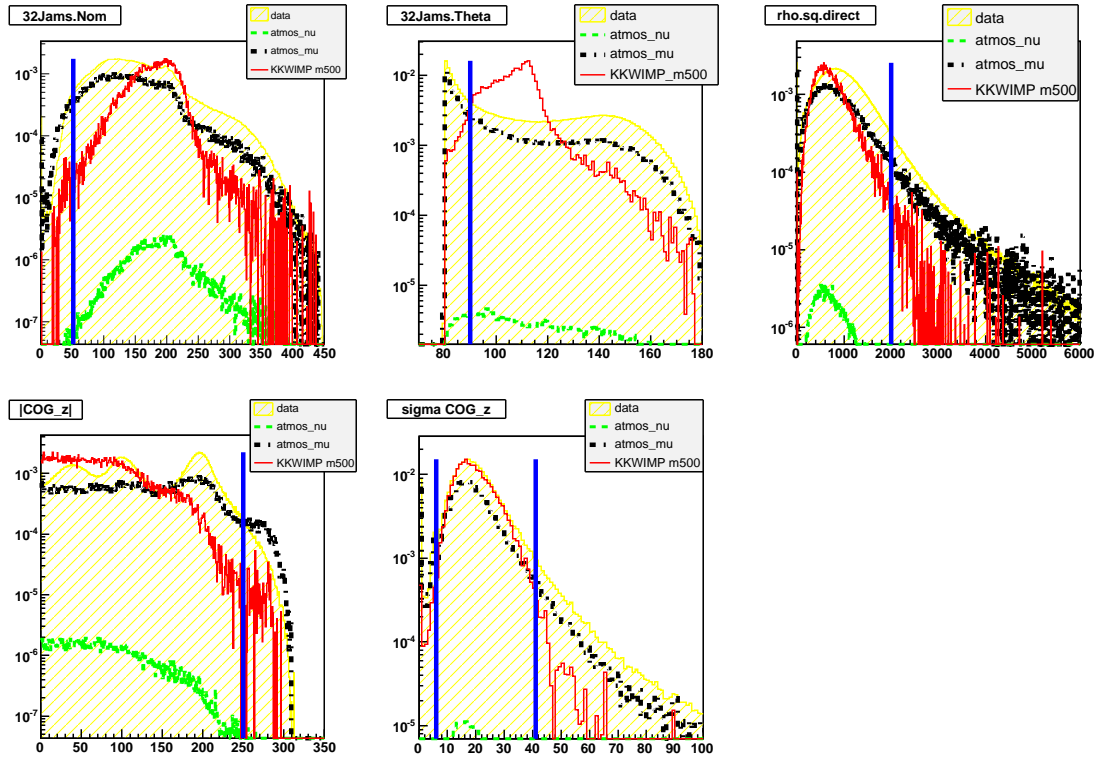


Figure A.4: The precut L3 variable distributions for the 2003 data with a 500 GeV WIMP mass as the signal. Blue (solid vertical) lines denotes where the linear precut is applied prior to the level 3 neural net training.

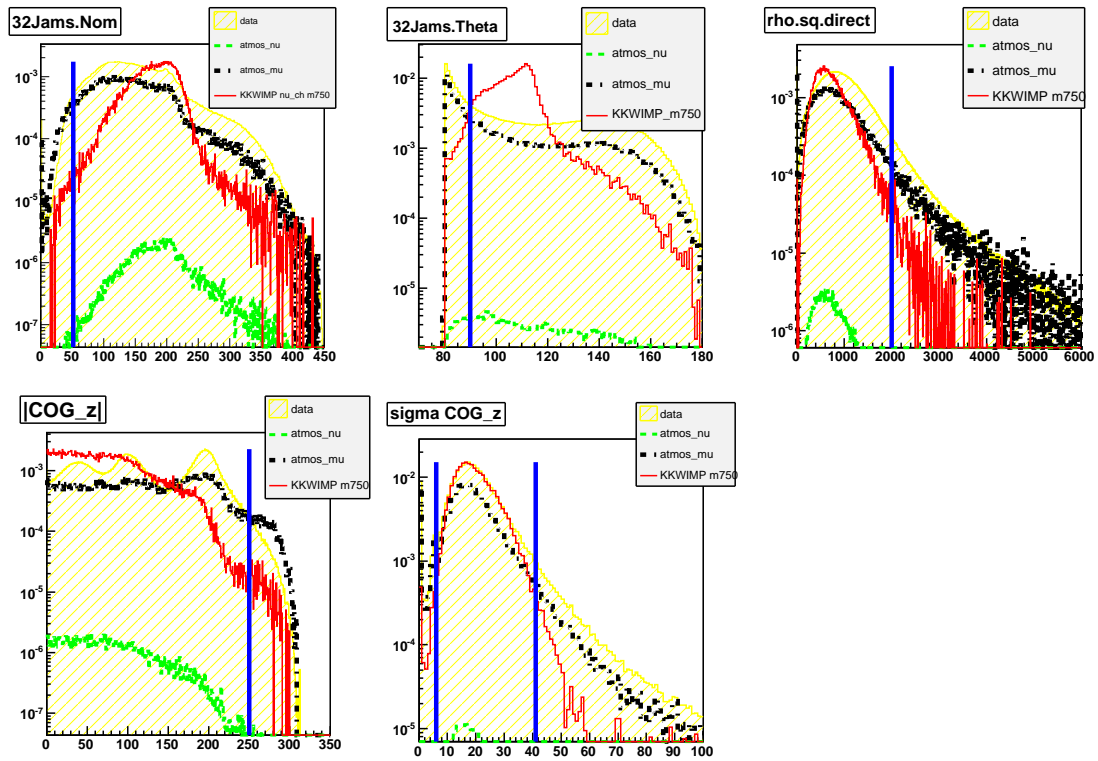


Figure A.5: The precut L3 variable distributions for the 2003 data with a 750 GeV WIMP mass as the signal. Blue (solid vertical) lines denotes where the linear precut is applied prior to the level 3 neural net training.

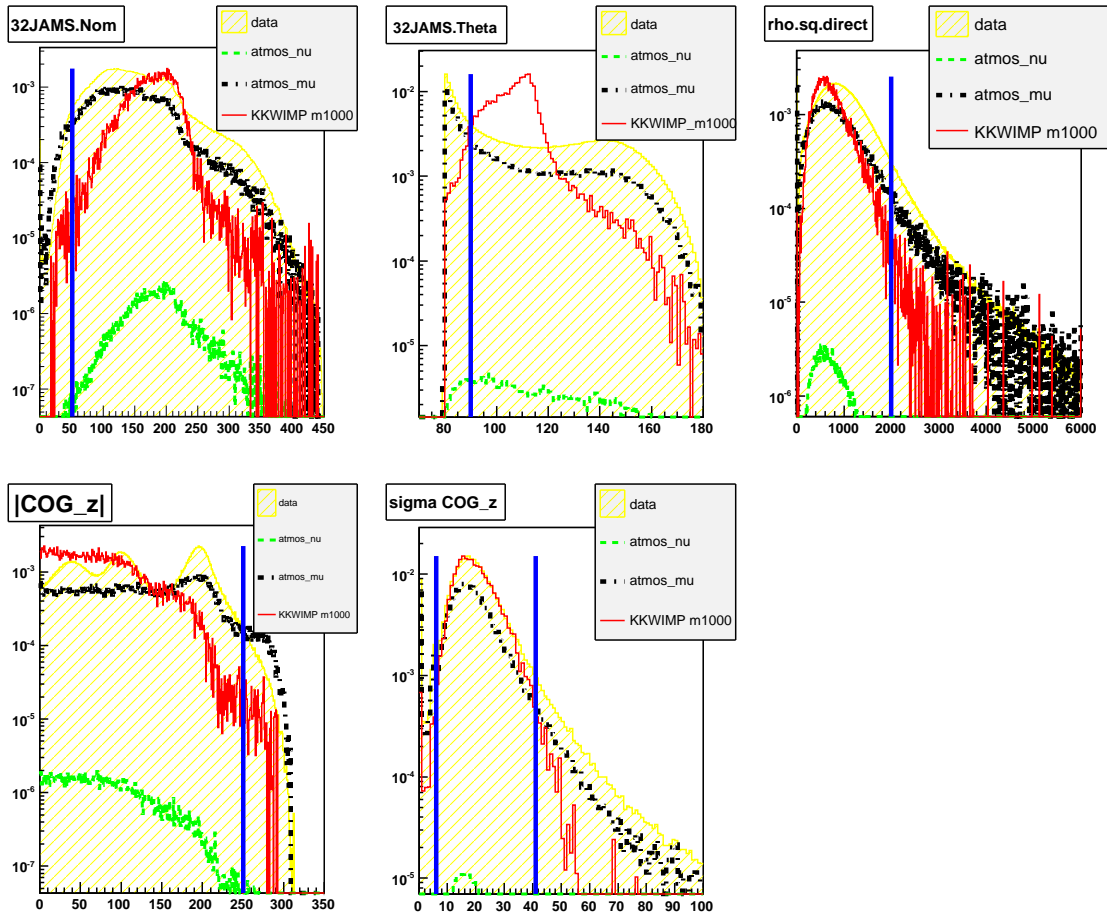


Figure A.6: The precut L3 variable distributions for the 2003 data with a 1000 GeV WIMP mass as the signal. Blue (solid vertical) lines denote where the linear precut is applied prior to the level 3 neural net training.

Appendix B: COGz Variable Distribution

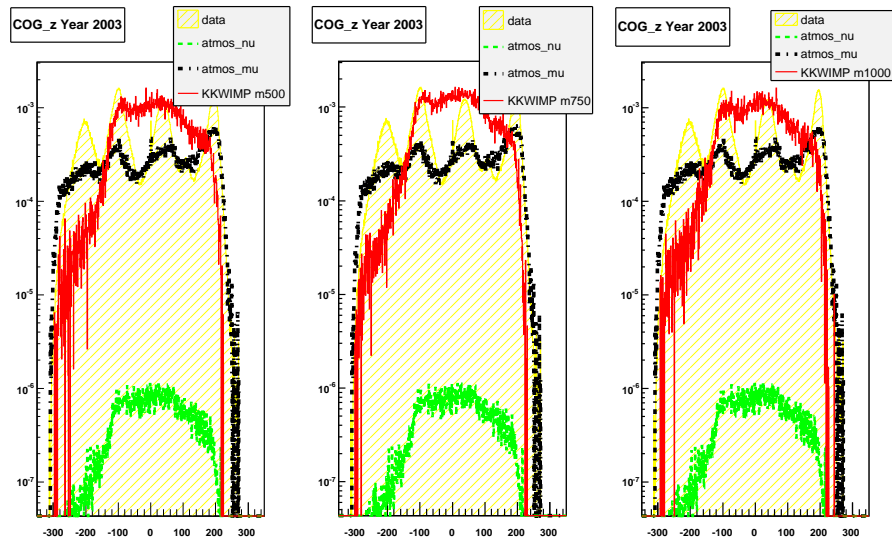


Figure A.7: The COGz distribution of year 2003 against 3 different WIMP masses

Appendix C: NN Variable Distribution for years 2002 and 2003

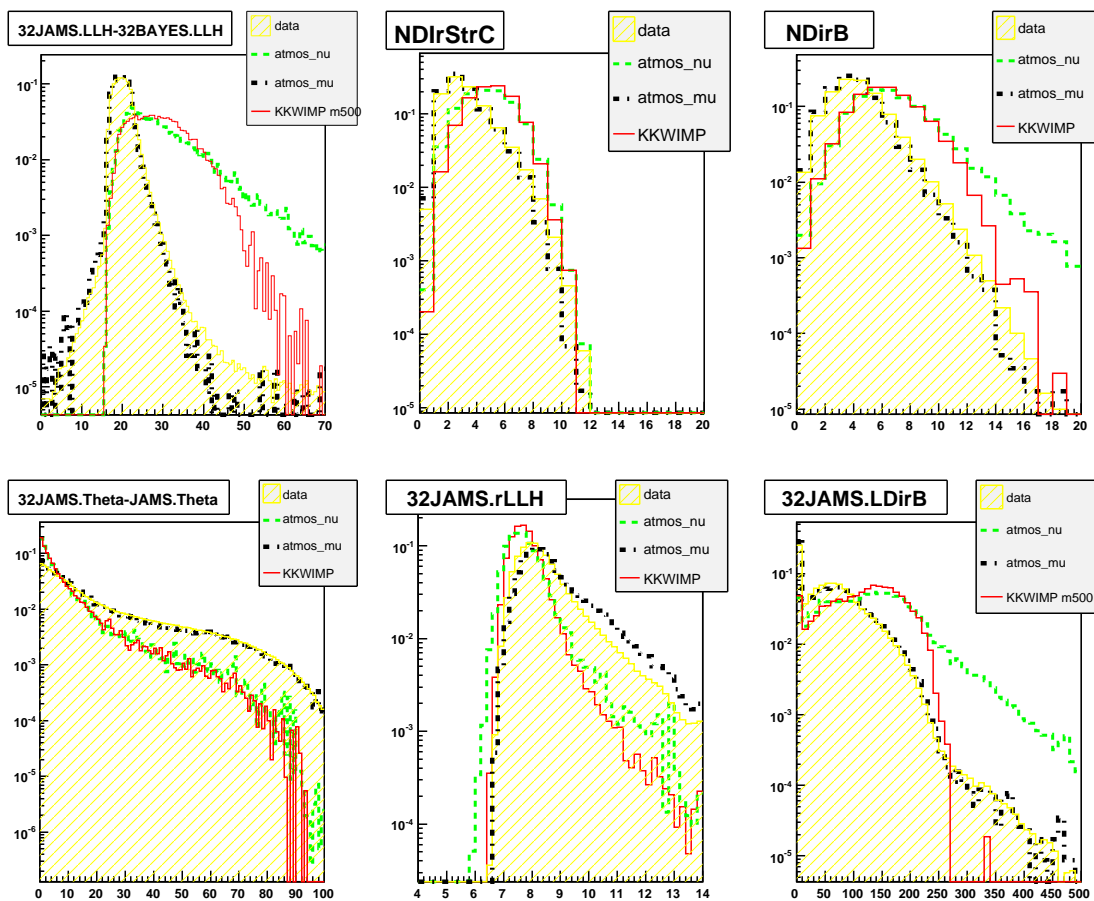


Figure A.8: Distribution of L3 Neural Net Variables year 2002 mass 500GeV, from top to bottom left to right, 32JAMS.LLH-32Bayes.LLH, NDirStrC, NDirB 32JAMS.Theta - JAMS.Theta, JAMS32.rLLH, JAMS32.LDirB

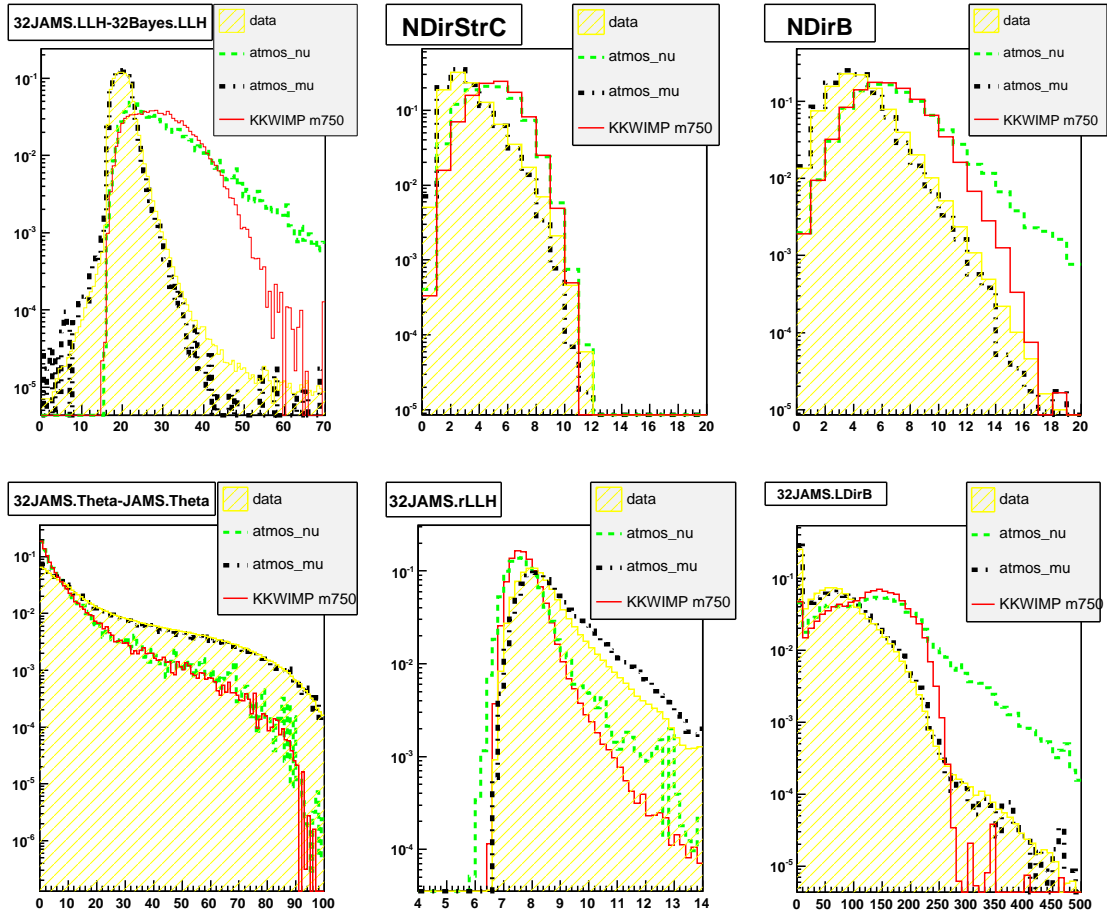


Figure A.9: Distribution of L3 Neural Net Variables year 2002 mass 1000GeV, from top to bottom left to right, 32JAMS.LLH-32Bayes.LLH, NDirStrC, NDirB 32JAMS.Theta - JAMS.Theta, JAMS32.rLLH, JAMS32.LDirB

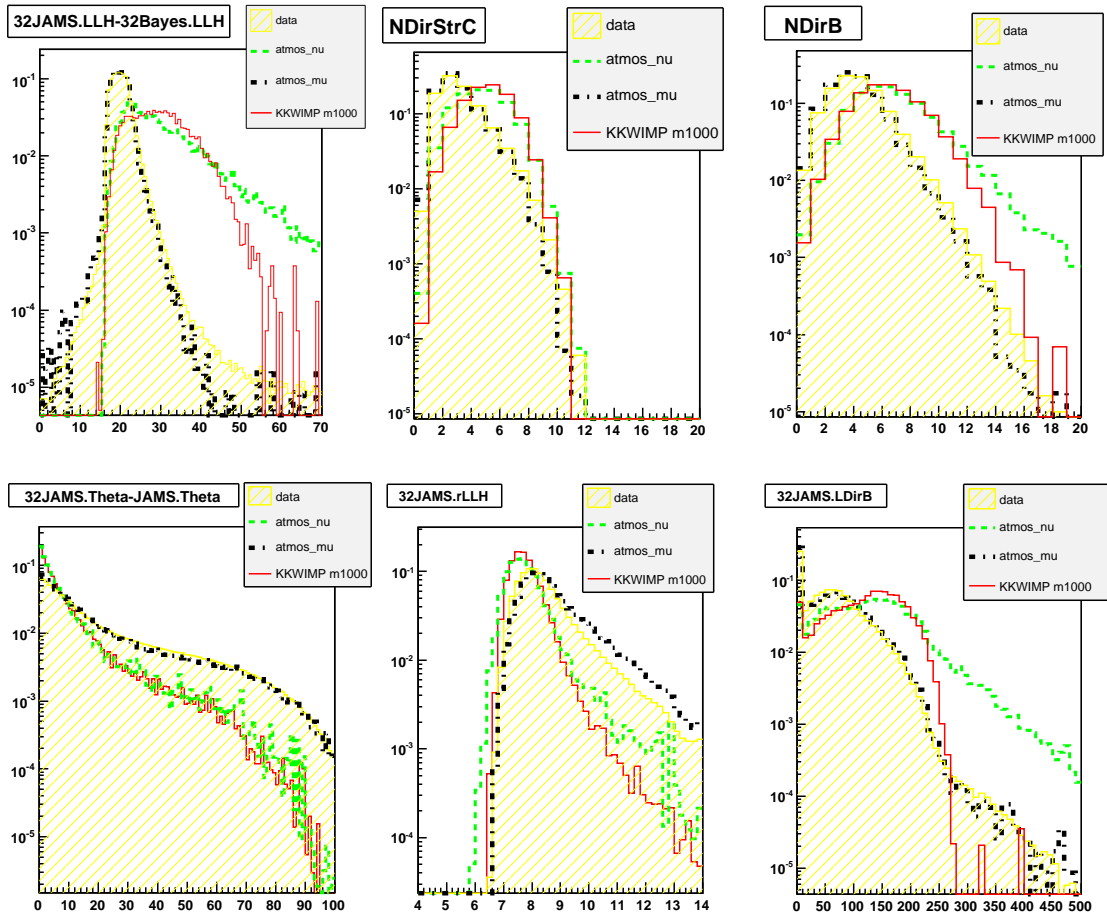


Figure A.10: Distribution of L3 Neural Net Variables year 2002 mass 1000GeV, from top to bottom left to right, 32JAMS.LLH-32Bayes.LLH, NDirStrC, NDirB 32JAMS.Theta - JAMS.Theta, JAMS32.rLLH, JAMS32.LDirB

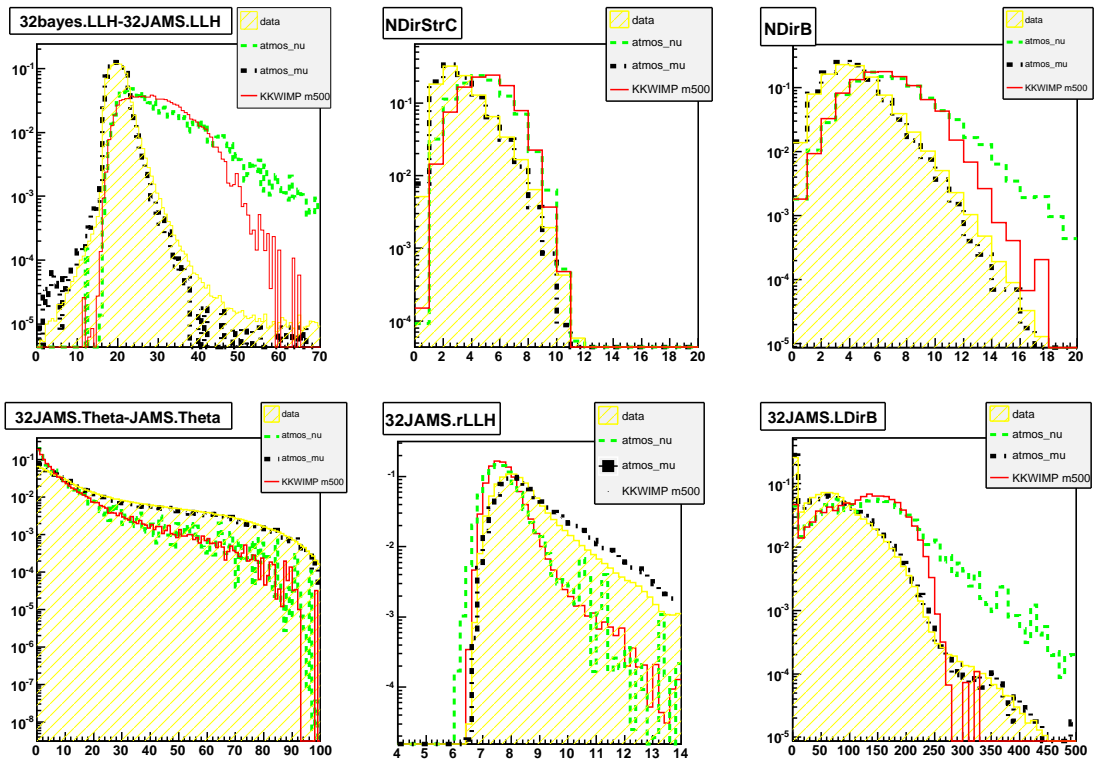


Figure A.11: Distribution of L3 Neural Net Variables year 2003 mass 500GeV, from top to bottom left to right, 32JAMS.LLH-32Bays.LLH, NDirStrC, NDirB 32JAMS.Theta - JAMS.Theta, JAMS32.rLLH, JAMS32.LDirB

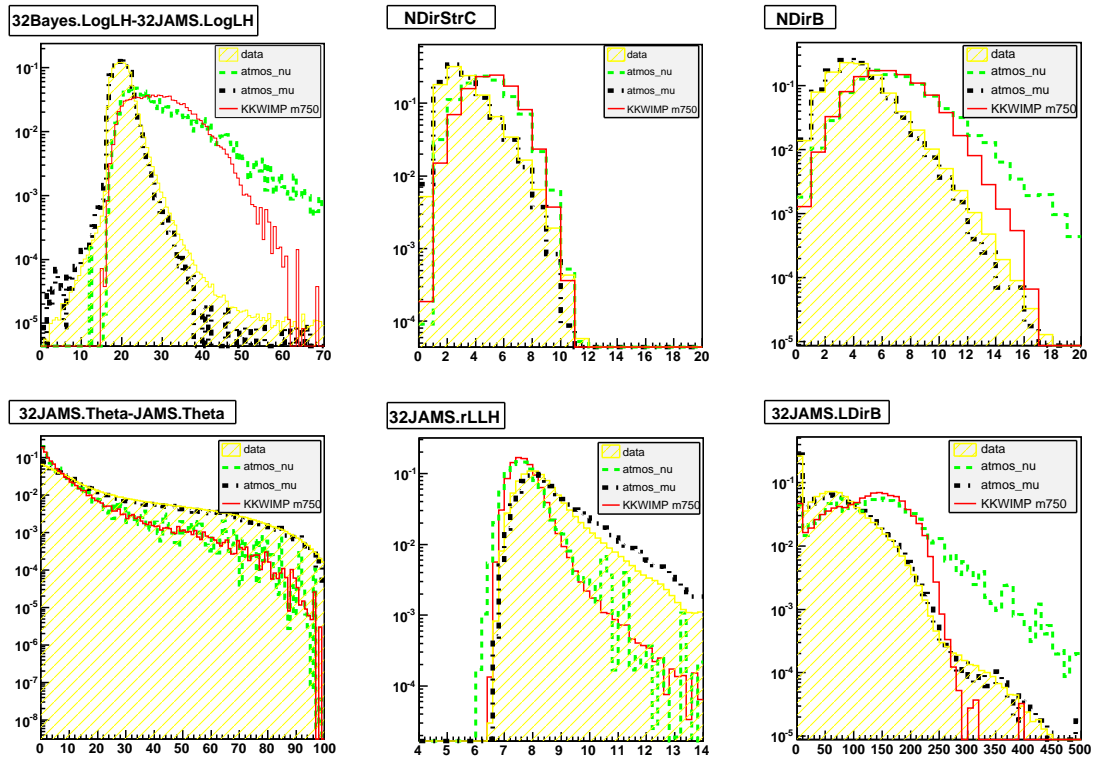


Figure A.12: Distribution of L3 Neural Net Variables year 2003 mass 750GeV, from top to bottom left to right, 32JAMS.LLH-32Bayes.LLH, NDirStrC, NDirB 32JAMS.Theta - JAMS.Theta, JAMS32.rLLH, JAMS32.LDirB

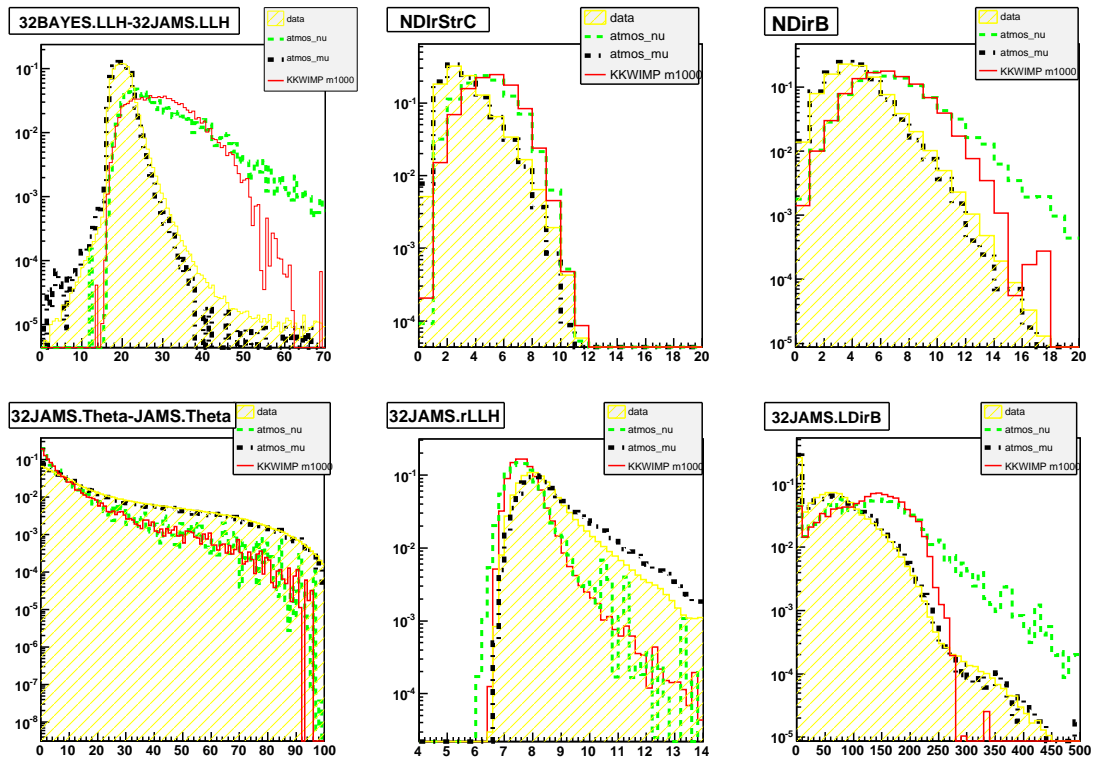


Figure A.13: Distribution of L3 Neural Net Variables year 2003 mass 1000GeV, from top to bottom left to right, 32JAMS.LLH-32Bayes.LLH, NDirStrC, NDirB 32JAMS.Theta - JAMS.Theta, JAMS32.rLLH, JAMS32.LDirB

Appendix D: MVA trained separately for m500 and m1000

For reference, the method and the result for using m500 and m1000 WIMP signal to train to obtain MVA weights are presented.

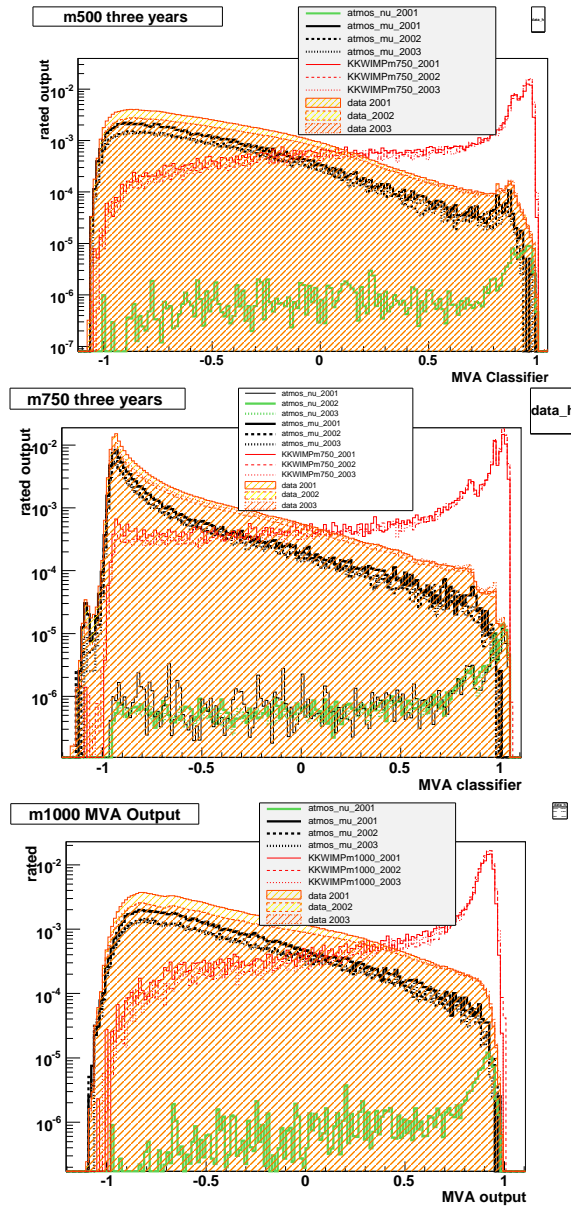


Figure A.14: MVA Classifier output for each mass

The Old sensitivity values for m500 and m1000 when trained against m500 and m1000 Signal

The same choice of NN variables was used to train 5000 WIMP signal events against 10000 data events for m500 and m750 WIMPs and 10000 signal events against 10000 data events for the 1000GeV KK WIMP. A cut was made at 0.85 for WIMP mass 500GeV and 1000GeV and a harder cut made at 0.9 for 750 GeV before going onto the optimization on the sensitivity.

For the case of WIMP 1000GeV, as the plot A.15 shows that there is further discriminating power after the neural net cut, one additional cut for the length of direct hit less than 100m was performed prior to the sensitivity calculation.

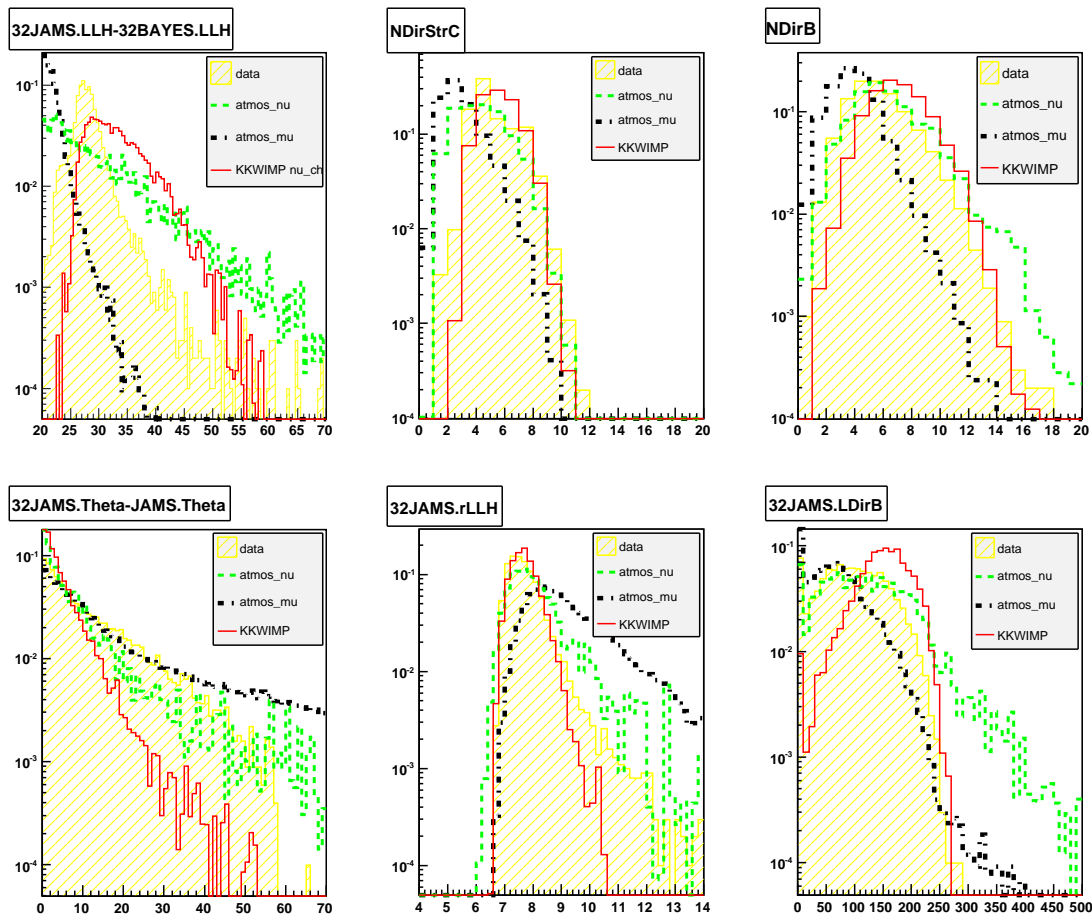
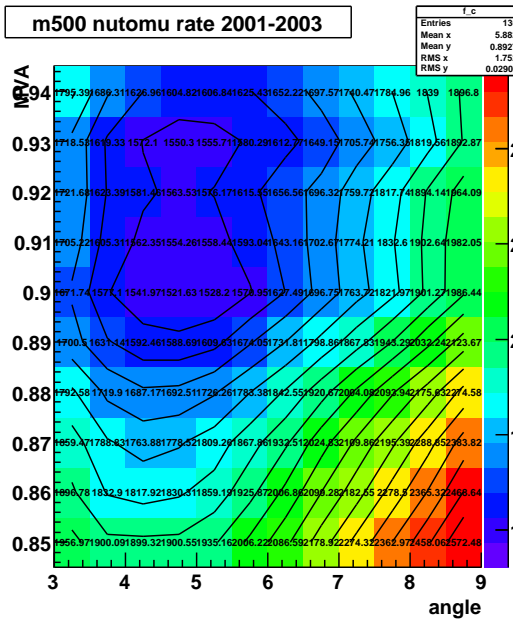


Figure A.15: Distribution of L3 Variables, after the NN cut year 2001 mass 1000GeV, from top to bottom left to right, 32JAMS.LLH-32Bays.LLH, NDirStrC, NDirB 32JAMS.Theta - JAMS.Theta, JAMS32.rLLH, JAMS32.LDirB

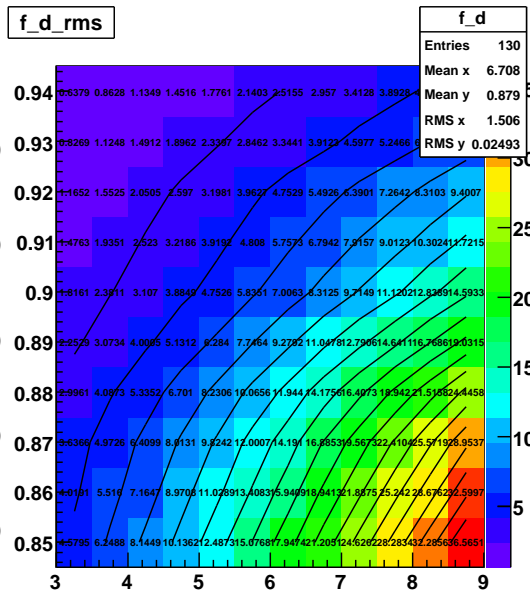
Table A.1: Final Cut Value and Sensitivity

Value	$m500$	$m750$	$m1000$
w_{gen}	$1.02128e - 24$	$1.0890e - 24$	$1.0956e - 24$
V_{eff} at final[km ³]	0.00298	0.00356	0.00394
MVA greater	0.9	0.96	0.87
angle less	4.5deg	4.5deg	4.0deg
bkg events	3.8849	2.364	3.38
FCaverage	4.77	4.104	4.57
nutomu	$1521.63km^{-3}yr^{-1}$	$1097.73km^{-3}yr^{-1}$	1103.75
ann.rate	$2.92327e21s^{-1}$	$2.049e21s^{-1}$	$2.09e21s^{-1}$
muon flux limit	$598.21km^{-2}yr^{-1}$	$506.64km^{-2}yr^{-1}$	$552.98km^{-2}yr^{-1}$

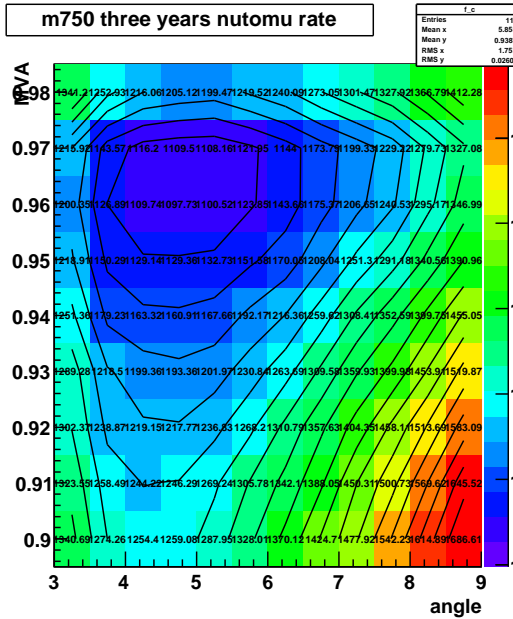
m500 nutomu rate 2001-2003



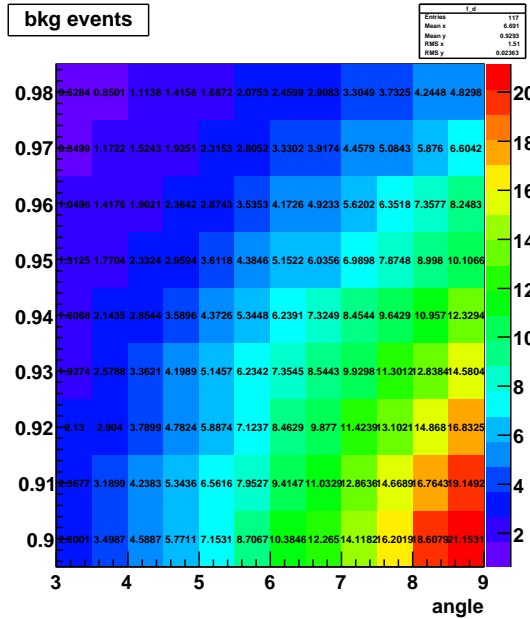
f_d_rms



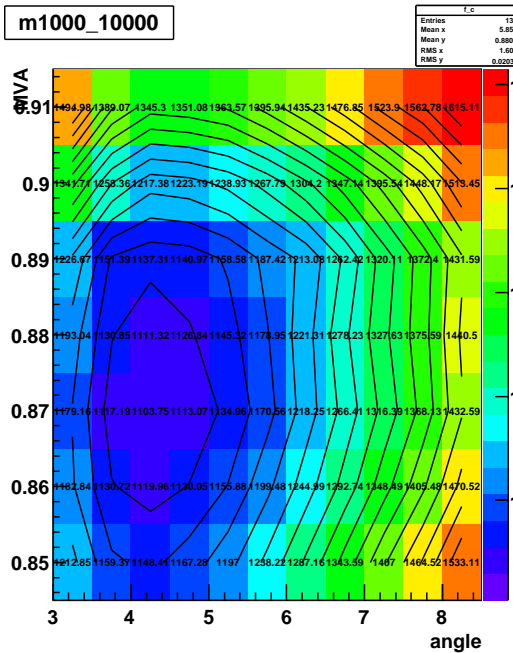
m750 three years nutomu rate



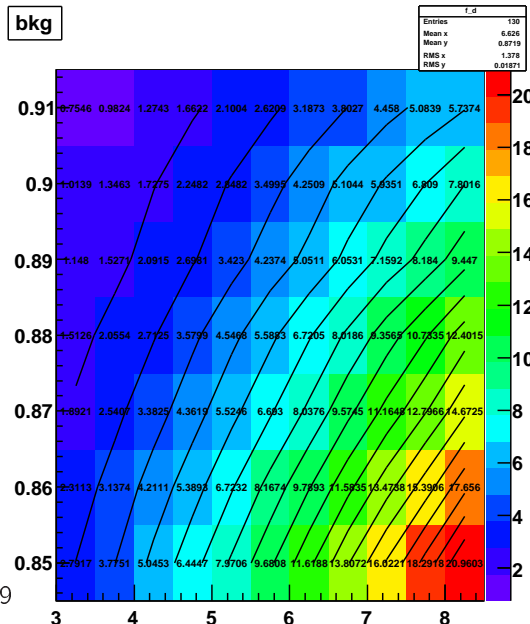
bkg events



m1000_10000



bkg



Appendix E: IceCube Project Timeline

- May 2004 1. IceCube Construction Project Baseline and U.S. National Science Board Construction Funding Approval
- June 2004
 1. UW Milestone - Validate Digital Optical Module Requirements for First Year Deployment
- July 2004
 1. UW Milestone - Conduct DOM Production Readiness Review for Initial Strings and Tanks
- August 2004
 1. Complete EHWD System Integration, Verification, and Testing
- September 2004
 1. UW Milestone - First Digital Optical Module Accepted and Ready for Shipment
- December 2004
 1. UW Milestone - Complete Shipment of EHWD Equipment to the South Pole
 2. Deploy initial IceTop Tanks
- January 2005
 1. Construction Status - 1 String and 8 Tanks Deployed
 2. Assemble and Operate the Enhanced Hot Water Drill at the South Pole
 3. Deploy Initial In-Ice Strings
 4. UW Milestone - Complete Assembly EHWD at the South Pole
- February 2005
 1. UW Milestone - Begin End-to-End System Tests of Initial Strings and Tanks
- April 2005
 1. UW Milestone - Collect and Process Data with Initial Strings and Tanks
- May 2005
 1. Complete End-to-End System Tests of Initial Strings and IceTop Array
- January 2006
 1. Construction Status - 9 Strings and 32 Tanks Deployed
- February 2006
 1. Determine Annual String Deployment Rates for Future Years
 2. UW Milestone - Perform Initial In-Ice and IceTop Data System Integration

- March 2006
 1. UW Milestone - Validate Digital Optical Module Requirements
- June 2006
 1. Establish Full Production Rate of Digital Optical Modules
- September 2006
 1. UW Milestone - Approve full production contracts for DOM and DAQ Components
- November 2006
 1. Validate In-Ice and IceTop Design
- December 2006
 1. UW Milestone - Beneficial Occupancy of the IceCube Laboratory
- January 2007
 1. Construction Status - 22 Strings and 52 Tanks Deployed
 2. Full Occupancy of the IceCube Laboratory
- March 2007
 1. Initial Operational and Data Analysis Capability
 2. UW Milestone - Complete AMANDA/IceCube Integration
 3. UW Milestone - Complete Detector Verification and Physics Benchmarking for Initial Operations
- August 2007
 1. Data System Software Complete
- January 2008
 1. Construction Status - 40 Strings and 80 Tanks Deployed
- June 2008
 1. Complete Integration of In-Ice and IceTop Data Systems
- January 2009
 1. Construction Status - 59 Strings and 120 Tanks Deployed
- January 2010
 1. Construction Status - 77 Strings (6 Deep Core) and 148 Tanks Deployed
- January 2011
 1. Construction Status - 86 Strings and 160 Tanks Deployed

References

- [1] H.R Crane. The energy and momentum relations in beta-decay, and the search for the neutrino. *Review of Modern Physics*, 20:278–295, 1948.
- [2] Fardon, Nelson, and Weiner. Dark energy from mass varying neutrinos. *JCAP 0410:005,2004*
<http://arxiv.org/pdf/astro-ph/0309800>.
- [3] J.Silk G.Bertone, D.Hooper. Particle dark matter : Evidence, candidates and constraints. *Physics Reports*, 405(5-6):279–390, January 2005.
- [4] Cheng, Matchev, and Schmaltz. Bosonic supersymmetry? getting fooled at the lhc.
www.arxiv.org/hep-ph/0205314.
- [5] Servant and Tait. Elastic scattering and direct detection of kaluza-klein dark matter.
www.arxiv.org/hep-ph/0209262.
- [6] Hooper/Kribs. Probing kaluza-klein dark matter with neutrino telescopes. www.arxiv.org/hep-ph/0208261.
- [7] Joakim Edsjo. *Aspects of Neutrino Detection of Neutralino Dark Matter*. PhD thesis, Uppsala University, 1997.
- [8] A E Chudakov. Search for heavy magnetic monopoles in an experiment at the baksan underground scintillation telescope. *1985 Sov. Phys. Usp. 28 1054-1055*, 1985.
- [9] Antares Collaboration. Search for cosmic neutrino point sources with the 5-line antares telescope.
<http://arxiv.org/abs/0909.1262>, 2009.
- [10] The Super-Kamiokande Collaboration. Search for astrophysical neutrino point sources at super-kamiokande. *Astrophys. J. 704 (2009) 503-512*, [arXiv:0907.1594](http://arxiv.org/abs/0907.1594), 2009.
- [11] C.de los Heros D.Hubert, A.Davour. Search for neutralino dark matter with amanda ii. In *29th International Cosmic Ray Conference, Pune*, 2005.
- [12] M.Danninger K.Han. Search for the kaluza-klein dark matter with the amanda/icecube detectors. In *31st International Cosmic Ray Conference, Lodz*, 2009.

- [13] Daan Hubert for the IceCube Collaboration Jim Braun. Searches for wimp dark matter from the sun with amanda. *Contribution to the 31st ICRC.Poland, arXiv:0906.1615*, 2009.
- [14] Anna Davour. *Search for Low Mass WIMPs with the AMANDA Neutrino Telescope*. PhD thesis, Uppsala Univerity, 2007.
- [15] Daan Hubert. *Search with the AMANDA detector for neutralino dark matter in the Sun*. PhD thesis, Vrije Universiteit Brussel, 2009.
- [16] Gunnar Nordström. Über die möglichkeit, das elektromagnetische feld und das gravitationsfeld zu vereinigen. *Physikalische Zeitschrift*, pages 504–506, 1914.
- [17] F.Ravndal. Scalar gravitation and extra dimensions. *The Gunnar Nordström Symposium on Thoretical Physics, Helsinki*, 2003.
- [18] T. Kaluza. On the problem of unity in physics. *Sitzungsber. Preuss. Akad. Wiss. Berlin (Math. Phys.)*, page 966, 1921.
- [19] O. Klein. Quantum theory and five-dimensional theory of relativity. *Z. Phys*, 37:895, 1926.
- [20] J.Overduin and P.Wesson. Kaluza klein gravity. *Phys.Rept.283:303-380,1997*, 1997.
- [21] David Wiltshire. Effective models of gravity in higher dimensions. *University of Cambridge PhD Thesis*, 1987.
- [22] L. Randall and R. Sundrum. A large mass hierarchy from a small extra dimension. *Phys.Rev.Lett*, 83:3370, 1999.
- [23] S. L. Parameswaran Y. Aghababaie, C. P. Burgess and F. Quevedo. Towards a naturally small cosmological constant from branes in 6d supergravity. *Nucl.Phys.B*, 680:389, 2004.
- [24] P. J. Steinhardt J. Khoury, B. A. Ovrut and N. Turok. The ekpyrotic universe: Colliding branes and the origin of the hot big bang. *Phys Rev D*, 64, 2001.
- [25] G. D. Kribs. Tasi 2004 lectures on the phenomenology of extra dimensions. *A writeup of a 2004 TASI Lectures, arXiv:hep-ph/0605325*.
- [26] S. Dimopoulos N. Arkani-Hamed and G. R. Dvali. The hierarchy problem and new dimensions at a millimeter. *Phys.Lett.B429:263-272*, pages 263–272, 1998.
- [27] M.Perelstein S.Cullen. Sn1987a constraints on large compact dimensions. *Phys.Rev.Lett.83,268*, 1999.
- [28] N.Kaloper J.March-Russell N.Arkani-Hamed, S.Dimopoulos. Rapid asymmetric inflation and early cosmology in theories with sub-millimeter dimensions. *Nucl.Phys.B 567,189*, 2000.

- [29] L. Randall and R. Sundrum. An alternative to compactification. *Phys.Rev.Lett*, 83:4690, 1999.
- [30] G.Servant K.Agashe. Warped unification,proton stability and dark matter. *Phys.Rev.Lett.* 93 (2004) 231805.
- [31] G.Servant K.Agashe. Baryon number in warped guts : Model building and dark matter related phenomenology. *JCAP 0502 (2005) 002*.
- [32] G.Servant D.Hooper. Indirect detection of dirac right-handed neutrino dark matter. *Astropart.Phys.* 24 (2005) 231-246.
- [33] H. C. Cheng T. Appelquist and B. A. Dobrescu. Bounds on universal extra dimensions. *Phys Rev D*, 64:025002, 2001.
- [34] E.Poppitz B.Dobrescu. Number of fermion generations derived from anomaly cancellation. *Phys.Rev.Lett.* 87 (2001) 031801.
- [35] E.Ponton Ho-Ung Lee T.Applequist, A.Dobrescu. Proton stability in six dimensions. *Phys.Rev.Lett.* 87 (2001) 181802.
- [36] B.Dobrescu T.Applequist, H.Cheng. Bounds on universal extra dimensions. *Phys.Rev. D64 (2001) 035002*, 2001.
- [37] S.Park J.Shu. Split universal extra dimension and dark matter. *Phys.Rev.D79.091702(R) 2009*.
- [38] J.Chang et al. An excess of cosmic ray electrons at energies of 300gev to 800gev. *Nature* 456, 362-365 (20 November 2008).
- [39] S.Torii. High-energy electron observations by ppb-bets flight in antarctica. <http://arxiv.org/abs/0809.0760>, 2008.
- [40] O.Adrinani et al. Observation of an anomalous positron abundance in the cosmic radiation. <http://arxiv.org/abs/0810.1527>, 2009.
- [41] Pasquale Dario Serpico Dan Hooper, Pasquale Blasi. Pulsars as the sources of high energy cosmic ray positrons. <http://arxiv.org/abs/0810.4995>, 2009.
- [42] Fermi/LAT collaboration. Measurement of the cosmic ray e+ plus e- spectrum from 20gev to 1 tev with the fermi large area telescope. <http://arxiv.org/abs/0905.0025>, 2009.
- [43] S.Park Jing Shu C.Chen, M.Nojiri. Kaluza klein dark matter after fermi. *IPMU09-0101*.
- [44] J. H. Oort. The force exerted by the stellar system in the direction perpendicular to the galactic plane and some related problems. *Bulletin of the Astronomical Institutes of the Netherlands*, 6:249, 1932.

- [45] F. Zwicky. Spectral displacement of extra galactic nebulae. *Helv. Phys. Acta*, 6:110, 1933.
- [46] Milgrom. A modification of the newtonian dynamics as a possible alternative to the hidden mass hypothesis. *Astrophysics*, 270:365, 1983.
- [47] Sanders Begeman, Broeils. *Monthly Notices of Royal Astronomical Society* 249,523, 1991.
- [48] M.Milgrom. A modification of the newtonian dynamics - implications for galaxies. *Astrophys.J.*270: 371-389, 1983.
- [49] Robert H.Sanders Jacob D.Beckenstein. A primer to relativistic mond theory. *Mass Profiles and Shapes of Cosmological Structures, EAS Publications Series, Vol.1*, 2005.
- [50] R. H. Sanders. Resolving the virial discrepancy in clusters of galaxies with modified newtonian dynamics. <http://arXiv:astro-ph/9807023>.
- [51] G.W.Angus, H.Y.Shan, H.S.Zhao, and B.Famaey. On the proof of dark matter, the law of gravity, and the mass of neutrinos. *Astrophys. J.* 654: L13-L16, 2007.
- [52] D. Clowe et al. A direct empirical proof of the existence of dark matter. <http://arXiv.org/astro-ph/0608407>.
- [53] P. Tisserand et al. Limits on the macho content of the galactic halo from the eros-2 survey of the magellanic clouds. <http://arXiv:astro-ph/0607207>.
- [54] The Planck Collaboration. The scientific programme of planck. *ESA-SCI(2005)1*, 2006.
- [55] M.Kowalski et al. Improved cosmological constraints from new, old and combined supernova datasets. *Astrophys.J.*686:749-778, 2008.
- [56] H. Bethe R. A. Alpher and G. Gamow. The origin of chemical elements. *Phys Rev*, 73:803, 1948.
- [57] M. Trodden and S. M. Carroll. Tasi lectures: Introduction to cosmology. <http://arXiv:astro-ph/0401547>.
- [58] O.Gerhard and J.Silk. Baryonic dark halos: A model with machos and cold gas globules. *astro-ph/9511036*, 1995.
- [59] J.Silk. The dark side of the universe. *2001: A Spacetime Odyssey (World Scientific, Singapore)*, 2008.
- [60] E.Turner R.Kolb. *The Early Universe*. Addison–Wesley, 1990.
- [61] Gerard Jungman, Marc Kamionkowski, and Kim Griest. Supersymmetric dark matter. *Physics Reports*, 267(5-6):195 – 373, 1996.

- [62] Pierre Salati. Quintessence and the relic density of neutralinos. *Physics Letters B*, 571(3-4):121 – 131, 2003.
- [63] Kim Griest and David Seckel. Three exceptions in the calculation of relic abundances. *Phys. Rev. D*, 43(10):3191–3203, May 1991.
- [64] Joakim Edsjö and Paolo Gondolo. Neutralino relic density including coannihilations. *Phys. Rev. D*, 56(4):1879–1894, Aug 1997.
- [65] Joakim Edsjo, Mia Schelke, Piero Ullio, and Paolo Gondolo. Accurate relic densities with neutralino, chargino and sfermion coannihilations in msugra. *Journal of Cosmology and Astroparticle Physics*, 2003(04):001, 2003.
- [66] M.Schmaltz H.Cheng, K.Matchev. Bosonic supersymmetry? getting fooled at the lhc. *Phys. Rev. D* 66, 056006 (2002).
- [67] G.Servant.T.Tait. Is the lightest kaluza-klein particle a viable dark matter candidate. *Nucl.Phys.B650:391-419,2003*.
- [68] S.Profumo D.Hooper. Dark matter and collider phenomenology of universal extra dimensions. *Phys.Rept.453:29-115,2007*.
- [69] Marc Kamionkowski Andriy Kurylov. Generalized analysis of weakly-interacting massive particle searches. *Phys.Rev.D69:063503,2004*, 2003.
- [70] G.Hinshaw et al WMAP Collaboration. Five-year wilkinson microwave anisotropy probe (wmap) observations: Data processing, sky maps, and basic results. *Astrophys.J.Suppl.180,225(2009)*.
- [71] P.Gondolo Y.Ramachers L.Roszkowski D.R.Tovey, R.J.Gaitskell. A new model-independent method for extracting spin-dependent cross section limits from dark matter searches. *Physics Letters B 488(2000) 17-26*, 2000.
- [72] CDMS Collaboration. A search for wimps with the first five-tower data from cdms. <http://arxiv.org/abs/0802.3530>, 2008.
- [73] COUPP. The chicagoland observatory for underground particle physics. <http://www-coupp.fnal.gov/>.
- [74] B.Majorovits et al. The cress dark matter search. *Proceedings of the 5th International Workshop on the IDM 2004*, 2004.
- [75] V.N.Lebedenko et al. Limits on the spin-dependent wimp-nucleon cross sections from the first science run of the zeplin-iii experiment. *Phys. Rev. Lett. 103, 151302 (2009)*, 2009.

- [76] E.Armengaud et al. First results of the edelweiss-ii wimp search using ge cryogenic detectors with interleaved electrodes. *arXiv:0912.0805v1*, 2009.
- [77] H.S.Lee et al. Limits on wimp-nucleon interactions with csi(tl) crystal detectors. <http://arxiv.org/abs/0704.0423>, 2007.
- [78] R.Bernabei et al. Dama results. <http://arxiv.org/abs/astro-ph/0305542>, 2003.
- [79] David Tucker-Smith Neal Weiner Spencer Chang, Graham D. Kribs. Inelastic dark matter in light of dama/libra. <http://arxiv.org/abs/0807.2250>, 2008.
- [80] Garczarczyk et al. for the Magic Collaboration. Grb observations with the magic telescopes. *Contribution to the 31st ICRC, Lodz, Poland, July 2009*, 2009.
- [81] R.Kiuchi et al. Cangaroo-iii search for tev gamma rays from two clusters of galaxies. *Astrophys. J.*, 704, 240-246 (2009), 2009.
- [82] F.Aharonian et al H.E.S.S. Collaboration. The energy spectrum of cosmic ray electrons at tev energies. <http://arxiv.org/abs/0811.3894>, 2008.
- [83] H.Mayer-Haesselwander et al. High-energy gamma-ray emission from the galactic center. <http://www.iop.org/EJ/ref/-prog=article/-target=inspec/0004-637X/596/2/1035/17>, 1998.
- [84] J.Edsjö L.Bergström C.Farnier Y.Akrami P.Scott, J.Conrad. Direct constraints on minimal supersymmetry from fermi-lat observations of the dwarf galaxy segue 1. <http://arxiv.org/abs/0909.3300>, 2009.
- [85] O.Reimer A.Strong, I.Moskalenko. Diffuse galactic continuum gamma rays. a model compatible with egret data and cosmic-ray measurements. <http://arxiv.org/abs/astro-ph/0406254>, 2004.
- [86] for the NEMO Collaboration C.Stefano. Status of nemo: results from the nemo phase-1 detector. <http://arxiv.org/abs/0901.1252>, 2008.
- [87] G. Aggouras et al. A measurement of the cosmic-ray muon flux with a module of the nestor neutrino telescope. <http://arxiv.org/abs/astro-ph/9906426>, 2005.
- [88] P.A.Rapidis for the KM3NET Consortium. Km3net:a large underwater neutrino telescope in the mediterranean sea. <http://arxiv.org/abs/0803.2478>, 2008.
- [89] M.Reno R.Gandhi, C.Quigg. Ultrahigh-energy neutrino interactions. *Astropart.Phys.*5:81-110,1996.
- [90] M.Reno I.Sarcevic R.Gandhi, C.Quigg. Neutrino interactions at ultrahigh energies. *Phys.Rev.D*58:093009,1998.

- [91] C.Wiebusch. *The Detection of faint light in deep underwater neutrino telescopes, PhD Thesis, 1995.* PhD thesis, Aachen, 1995.
- [92] Karl Mannheim John Learned. High energy neutrino astrophysics. *Annual Review of Nuclear and Particle Science Vol. 50: 679-749, 2000.*
- [93] K.Woschnagg for the AMANDA Collaboration. Optical properties of south pole ice at depths from 140 to 2300 meters. *Proceedings of the 26th International Cosmic Ray Conference. August 17-25, 1999, 1999.*
- [94] M.Ackermann et al AMANDA Collaboration. Optical properties of deep glacial ice at the south pole. *J. Geophys. Res., 111, D13203, 2006.*
- [95] K.Woschnagg et al. A deep high resolution optical log of dust, ash and stratigraphy in south pole glacial ice. *Geophysical Research Letters 32 (November 2005), 2005.*
- [96] B.Price and L.Bergström. Optical properties of deep ice at the south pole:scattering. *Appl.Opt.,36,4181-4194, 1997.*
- [97] IceCube collaboration. The preliminary design document. *October 11, 2001 Revision:1.24.*
- [98] L.Gladstone. Moon shadow observation by icecube. *31st International Cosmic Ray Conference, Lodz, 2009.*
- [99] S.Yoshida. Constraints on neutrino interactions at energies beyond 100pev with neutrino telescopes. In *31st International Cosmic Ray Conference, Lodz, 2009.*
- [100] G. L. Fogli, E. Lisi, A. Mirizzi, D. Montanino, and P. D. Serpico. Oscillations of solar atmosphere neutrinos. *Phys. Rev. D, 74(9):093004, Nov 2006.*
- [101] J. Edsjo. Wimpsim neutrino monte carlo. <http://www.physto.se/edsjo/wimpsim/>.
- [102] Torbjörn Sjöstrand et al. Pythia event generator. <http://home.thep.lu.se/torbjorn/Pythia.html>.
- [103] J.Edsjö. Nusigma 1.15.
- [104] M.T/'ortola J.Valle M.Maltoni, T.Schewetz. Status of global fits to neutrino oscillations. *New J. Phys. 6, 122 (2004).*
- [105] Stockholm University T.Burgess. Wimpeventf2k.
- [106] J.Capdevielle G.Schatz T.Thouw D.Heck, J.Knapp. Corsika:a monte carlo code to simulate extensive air showers. *Tech. Rep. FZKA-6019.*
- [107] D.Chirkin. Cosmic ray energy spectrum measurement with the antarctic muon and neutrino detector array. *PhD Thesis, UC Berkeley, 2003.*

- [108] D.Chirkin. dcorsika update report.
- [109] H.Meyer B.Wiebel-Sooth, P.Biermann. Cosmic rays vii. individual element spectra:prediction and data. *Astron.Astrophys.330(1998)389-398*.
- [110] S.Ostapchenko N.Kalmykov. The nucleus-nucleus interaction, nuclear fragmentation,and fluctuation of extensive air showers. *Phys.Atom.Nucl.56(1993)346-353*.
- [111] A.Pavlov N.Kalmykov, S.Ostapcheko. Quark-gluon string model and eas simulation problems at ultra-high energies. *Nucl.Phys.Proc.Suppl.52B(1997)17-28*.
- [112] P.Lipari. Lepton spectra in the earth's atmosphere. *Astropart.Phys.1(1993)195-277*.
- [113] M.Kowalski A.Gazazov. Anis: High energy neutrino generator for neutrino telescopes. *Comput.Phys.Commun.172(2005)203-213*.
- [114] D. Chirkin and W Rhode. Muon monte carlo: A high-precision tool for muon propagation through matter. 2004.
- [115] S Hundertmark. Amasim neutrino detector simulation program. In *Simulation and Analysis methods for large neutrino detectors in Ice*, edited by C.Spiering, 1999.
- [116] A. Karle. Monte carlo simulation of photon transport and detection in deep ice: muons and cascades, in simulation and analysis methods for large neutrino telescopes. In *Simulation and Analysis methods for large neutrino detectors in Ice*, edited by C.Spiering, 1999.
- [117] Paolo Desiati Kurt Woschnagg Gary Hill, Albrecht Karle. Evidence for insufficient absorption in the amanda monte carlo. <http://icecube.wisc.edu/~ghill/absorption/absorption.html>, 2009.
- [118] Carlos de los Heros Anna Davour. Optimizing direct walk ii for short tracks. *Amanda Internal Reports 20031102*.
- [119] Peter Steffen. Amanda pattern recognition. *AMANDA/IceCube Meeting in Stockholm 2002, Presentation*.
- [120] Arvid Pohl. Flare events in amanda. http://www5.hik.se/personal/tpoar/Flare_proposal.html.
- [121] Andreas Hoecker et al. Toolkit for multivariate analysis with root. <http://tmva.sourceforge.net>.
- [122] WIMP group. Minutes of dedicated call meeting for kk amanda analysis unblinding 8th december. http://wiki.icecube.wisc.edu/index.php/WIMP_phone_call_December – 08_2009, 2009.
- [123] Gary J. Feldman and Robert D. Cousins. Unified approach to the classical statistical analysis of small signals. *Phys. Rev. D*, 57(7):3873–3889, Apr 1998.

- [124] J.Edsjo. Lepton/neutrino/hadronic shower flux conversion script. <http://copsosx03.physto.se/cgi-bin/edsjo/wimpsim/flxconv.cgi>, 2009.
- [125] T.Ohlsson M.Blennow, J.Edsjo. Neutrinos from wimp annihilations obtained using a full three-flavor monte carlo approach. *JCAP 0801:021,2008*, 2008.
- [126] IceCube Collaboration. Limits on muon flux from kaluza-klein dark matter annihilations in the sun from the icecube 22-string detector. *arxiv:astro-ph:0910.4480*, 2009.
- [127] CDMS Collaboration. Results from the final exposure of the cdms ii experiment. *arXiv: 0912.3592*, 2009.
- [128] G.Wikström and J.Edsjo. Limits on the wimp-nucleon scattering cross-section from neutrino telescope. *JCAP 04(2009) 009 arXiv: 0903.2986*, 2009.
- [129] Jeff Filippini Rick Gaitskell. Dm tools website. <http://dmtools.brown.edu/>, 2000.
- [130] The Zeus Collaboration. Measurement of $d\pm$ production in deep inelastic $e\pm p$ scattering at desy heras. *Phys. Rev. D 69, 012004 (2004)*, 2004.
- [131] Predrag Miocinovic. Muon energy reconstruction in the amanda. *PhD Thesis, UC Berkley*, 2001.
- [132] Kahae Han. Simulation of cascade using geant4 for icecube. *IceCube Internal Report*, 2005.
- [133] Gustav Wikström. A search for solar dark matter with the icecube neutrino telescope. *PhD Thesis, Stockholm University*, 2009.
- [134] Ty DeYoung. Observations of atmospheric muon neutrinos with amanda. *PhD Thesis, University of Wisconsin*, 2001.
- [135] A.Biron. Reconstruction uncertainties due to time calibration errors. *AMANDA Internal Reports 20001101*, 2000.
- [136] J.Dunkley et al WMAP Collaboration. Five-year wilkinson microwave anisotropy probe (wmap) observations: Likelihoods and parameters from the wmap data. *Astrophys.J.Suppl.180:306-329,2009*.
- [137] J. F. Oliver, J. Papavassiliou, and A. Santamaria. Bounds on models with one latticized extra dimension. *Phys. Rev. D, 68(9):096003*, Nov 2003.
- [138] Olbren Depaepe. Onderzoek van de gevoeligheid van amanda voor kaluza klein donkere materie in de zon. *Licentiaat in de Wetenschappen, Vrije Universiteit Brussel, Belgium, 2007*, 2007.
- [139] Yulia Minaeva. Search for neutralino dark matter with the amanda-ii neutrino telescope. *PhD Thesis, University of Stockholm*, 2004.

- [140] Ralf Ehrlich. The search for neutralino dark matter with the amanda neutrino telescope. *PhD Thesis, University of Maryland*, 2008.
- [141] Thomas Burgess. A search for solar neutralino dark matter with the amanda-ii neutrino telescope. *PhD thesis, Stockholm University*, 2008.
- [142] Alfio Rizzo. Amanda 2001-2006 solar wimps analysis. *PhD thesis, in preparation, Vrije Universiteit Brussel, Belgium*, expected 2010.
- [143] Carsten Rott. Searches for dark matter from the galactic halo with icecube. *CCAPP Symposium Talk, Ohio State University*, 2009.
- [144] Gregory D. Mack John F. Beacom, Nicole F. Bell. Upper bound on the dark matter total annihilation cross section. *Phys.Rev.Lett.*99:231301,2007, 2007.
- [145] T. Han D. Hooper J. Alvarez-Muniz, F. Halzen. Phenomenology of high energy neutrinos in low-scale quantum gravity models. *Phys.Rev.Lett.* 88 (2002) 021301, 2001.
- [146] Francis Halzen Tao Han Dan Hooper Jaime Alvarez-Muniz, Jonathan L. Feng. Detecting microscopic black holes with neutrino telescopes. *Phys.Rev.* D65 124015, 2002.